A Model for Sample Stacking in Microcapillary DNA Electrophoresis

by

Alok Srivastava

Submitted to the Department of Mechanical Engineering
in partial fulfillment of the requirements for the degree of

Doctor of Philosophy

at the

Massachusetts Institute of Technology

June 2002

Signature of
Author:..................... ....
Department of Mechanical Engineering
May 10, 2002

Certified
by:........... ....
Daniel J. Ehrlich
Principal Research Scientist
Thesis Supervisor

Accepted
by:...
Ain A. Sonin
Professor of Mechanical Engineering
Chairman, Department Committee on Graduate Students

A Model for Sample Stacking in Microcapillary DNA Electrophoresis

by

Alok Srivastava

Submitted to the Department of Mechanical Engineering
on May 10, 2002 in partial fulfillment of the
requirements for the degree of
Doctor of Philosophy

ABSTRACT

Sanger's method of chain termination is the method of choice in DNA sequencing, where electrophoresis is used to separate the different sized DNA. In the past decade, microfabricated capillary devices have been developed and are increasingly used to perform DNA electrophoresis. While tremendous progress has been made in the process, sample injection has not been well understood. In an earlier study, images of sample injection obtained using video microscopy showed sharp sample stacking peak at the trailing edge of the sample plug.

This thesis examines the underlying physics that explain the behavior of DNA in microcapillary electrophoresis. A developed model captures the dynamics of the major electrolytes in the system. The applied voltage and the conductivity profile determine the local electric field. The electric field drives the analyte transport. The analyte consists of DNA molecules of various fragment sizes. Since the DNA concentration is smaller than the electrolyte concentration by a few orders of magnitude, its concentration does not affect the conductivity. The major components of the sample are identified, and role during injection is investigated. Analytical studies of the electrolyte boundary dynamics and evolution and the transport of DNA are presented. The effect of the buffer, applied voltage during injection, and sample mobility on stacking are shown.

A numerical model is implemented to quantitatively predict the stacking of DNA in microcapillary electrophoresis. The numerical model has been developed for the 1-dimensional case. The model is verified using analytical results. Results of numerical models that predict the behavior of DNA under experimental conditions are presented. The numerical model is compared with real experimental data to evaluate its predictive power. Preliminary numerical simulations have also been done for 2-dimensional geometries. A procedure has been developed for design of injector lengths to obtain a given resolution of separation in a microcapillary channel of specified length. Strategies for optimization are presented for improving the performance of the devices.

Thesis Supervisor: Daniel J. Ehrlich
Title: Principal Research Scientist

Acknowledgements

I am grateful to Prof. Peter So, who helped me face challenging hurdles in the course of my thesis. I appreciate the encouragement and support of Prof. Paul Matsudaira. I would like to thank my advisor, Dr. Dan Ehrlich for the opportunity to work on this project. I would also like to thank Prof. Rowell and Prof. McKinley for their guidance.

I would like to thank the following persons for valuable discussions and insights in different aspects of this work: Dr. Herbert Zeiger (sample stacking), Prof. Markus Zahn (electrodynamics), Prof. Ain Sonin (electrochemistry and fluid mechanics), Dr. Rich Garner (plasma physics), Ramkumar Krishnan (electrochemistry), Prof. Paul Laibinis (electrochemistry), Dr. Suvranu De (finite element methods), Prof. Jaime Peraire (numerical methods), Prof. Alan Grodzinsky (problem formulation), Prof. John G. King, Dr. Chandra Narayanan (finite difference method), Dr. Rama Rao (numerical method), and Dr. George Georghiou (2-D FCT).

I thank Maribel Vazquez for making the experimental data available, Mark Novotny and Samantha Desmarais for providing detailed information on experiments and protocols, and James Evans for the helping with graphical data software.

I thank the Whitehead Institute for Biomedical Research and MIT for all the resources, and the MIT Libraries in particular for their services. I thank Prof. John Vander Sande and Cambridge-MIT Institute (CMI) for the support to work at University of Cambridge.

I am grateful to my wife Dr. Dawn Hastreiter for her love, encouragement, and having faith in my abilities. I am indebted to my parents Mrs. Shashi Bala Srivastava and Mr. Bijay Krishna Srivastava, and Badki Didi and Chotki Didi for their love, patience and sacrifices.

Table of Contents

List of Figures

List of Tables

Chapter 1. Introduction

1. Problem description

Electrophoresis is a separation process based on the difference in the electro-migration rates between constituents of the analyte. While electrophoresis is conventionally done in slab gels, micro-capillary electrophoresis has gained considerable importance in high volume sequencing. Deoxyribonucleic acid (DNA) sequencing is an important application of micro-capillary electrophoresis. The most widely used method of DNA sequencing is based on separating fragments of DNA prepared from Sanger [1] sequencing reactions. Upon separation, the appropriately tagged fragments are detected using laser-induced fluorescence. The optical signal is collected, processed, analyzed, and the sequence information of that DNA fragment is obtained. The sequence has four building blocks - adenine (A), thymidine (T), guanosine (G), and cytosine (C). Micro-capillary based DNA sequencing has become important for two reasons. This method requires smaller sample quantities and yields faster separation times. It is also amenable to high integration and high throughput. The need for sequencing various genomes is growing exponentially. Some other applications of micro-capillary electrophoretic DNA separation are DNA fingerprinting [2] and single nucleotide polymorphism (SNP) detection.

A sample is injected into a capillary device for the purpose of separation into its constituents. Prior to separation, the sample is collapsed into a smaller volume of higher density. This formation of a smaller and denser sample plug is called sample stacking, and it has been reviewed in [3] and [4]. Images of sample stacking of DNA were obtained using video microscopy [5]. It was speculated that DNA sample stacking in microfabricated capillary electrophoresis [6] was due to field-amplified stacking [7]. Field amplified stacking predicts concentration changes in the front of the sample plug. Since the observed stacking was at the rear part of the plug, the field-amplified stacking hypothesis could not explain the experimental results. The goal of this thesis is to bridge that gap by a physics-based mathematical and numerical model for the phenomena of sample stacking in microcapillary DNA electrophoresis.

2. Outline of thesis

This thesis consists of an introduction and three parts, which are described as follows.

Introduction

In this part, the method of DNA sequencing using microcapillaries is introduced. The different steps of the process are detailed. The experiments and protocols used in the BioMEMS Laboratory at the Whitehead Institute are outlined. The experiments from which data have been used in this thesis are described.

Part 1

The first part is model development and understanding the mechanism of stacking. The problem of stacking has been decoupled into (1) the dynamics of the electrolytes under the action of an applied electric field, which is nearly unaffected by the small amounts of DNA sample, and (2) the dynamics of the constituent DNA under the action of that electric field. The electric field, which has a characteristic distribution and dynamics, is responsible for the transport of DNA and results in the stacking observed. This stacking model complements the resolution analysis model shown by Luckey [8], and these together form a comprehensive model for DNA electrophoresis.

A previously reported model of the mechanism of stacking in DNA electrophoresis [5] makes unjustified assumptions and lacks accuracy, physical basis and predictive power. The original contribution in this part of the thesis is understanding the factors responsible for the phenomena and applying a physics-based model to explain the mechanism of sample stacking.

Part 2

The second part is numerical simulation. The literature for numerical implementation of one-dimensional (1-D) dynamical simulation of electrophoresis has been reviewed. A 1-D sample-stacking model has been implemented using a finite difference time domain based method. The method used a difference scheme that is forward in time and central in space (FTCS). It is well known that the FTCS scheme has a disadvantage of incorporating numerical diffusion. Although specialized schemes like the Lax-Wendroff [9] method and flux corrected transport (FCT) [10] were explored, FTCS was preferred because it was found to yield results which were sufficiently accurate for this model.

In order to extend the model to a two-dimensional (2-D) geometry the solution of the transport equation with advection and diffusion in a 2-D geometry has been applied. The advection computation in turn requires computation of an electric field in a 2-D geometry. A flux corrected transport-based numerical tool capable of solving 2-D transport and computing the electric field has been developed for applications in plasma physics at the University of Cambridge. This existing numerical tool has been applied to electrophoresis. The advantages of this numerical tool are its capability of handling sharp moving boundaries within the solution, the ability to solve problems in two-dimensional domains, and that it does not make *a priori* assumptions about charge neutrality. Using these numerical tools, phenomena of sample stacking in microfabricated devices has been studied.

The original contribution in this part of the thesis is the implementation of numerical models to demonstrate the principles of the mechanism of sample stacking in DNA electrophoresis.

Part 3

In the third part, comparison of numerical results with the experimental data has been performed. The available experimental data is a comprehensive set of images of sample injection in a microfabricated electrophoresis device obtained from video microscopy. From these images the following key experimental parameters have been extracted– (a) speed of sample wave, (b) stacking ratio of the sample peak, and (c) the evolution of the wave profiles. The effect of higher applied voltages and the effect of buffer on stacking is quantitatively predicted. The numerical model for sample stacking in DNA electrophoresis using micromachined devices has been validated. A design procedure has been developed to select injector length for a given resolution requirement of a certain fragment size, e.g. 800 base single stranded DNA (800b ssDNA).

The original contribution in this part of the thesis is the validation of the numerical model using existing experimental data of sample stacking. Another contribution is the study of the effect of varying different parameters, namely voltage, buffer mobility and injector length on the amount of sample stacking.

3 Structure of DNA

Deoxyribonucleic acid (DNA) is assembled from two linear polymers [11]. Each of the polymers consists of monomeric units called nucleotides. Each nucleotide consists of three components – deoxyribose sugar, 5-carbonic base, and phosphate. The bases that form a part of the nucleotides are of four different types – adenine, guanine (purines) and thymine and cytosine (pyrimidines). The sugars bond with one of the four bases and form one of the four nucleosides: adenosine, guanosine, cytidine, and thymidine. Each polymer is also called a strand and is characterized by its polarity (a 3'-end and a 5'-end.) Two strands associate to form DNA. The strands run parallel to each other but have opposite polarities. The bases are inside and connect with one another by weak hydrogen bonds. The bonds formed between the base pairs follow the rule of Chargaff which states that there are only two types of base-pairs in DNA: A-T pairs and G-C pairs.

The secondary structure of DNA reveals that the two polynucleotide chains are wound around a common axis to produce a double helix with a helix diameter of 20 Å. The adjacent bases are 3.4 Å apart along the axis and rotated 36° with respect to one another. There are 10 nucleotides per one full turn of the helix, which corresponds to a length of 34 Å. The bases are located inside the double helix and the phosphates and sugars outside the double helix.

4. DNA Sequencing

DNA sequencing is the extraction of the sequence information of the building blocks along a fragment of deoxyribonucleic acid (DNA), the fundamental carrier of genetic information. DNA sequencing consists of multiple steps, namely

(a) DNA extraction from tissue,
(b) sequencing reactions,
(c) separation of sequencing reaction products,
(d) detection of separation bands, and
(e) analysis.

Shotgun Sequencing and Assembly

In some instances, the DNA libraries are built from random sequences. In this method, also called shotgun sequencing, randomly located individual fragments are sequenced and then together using intensive computational methods by identifying the regions of overlap.

DNA Extraction

Chromosomal DNA is extracted from tissue which is lysed with buffer containing detergent and EDTA. EDTA chelates Mg^{2+} ions and prevents the magnesium ions from activating DNAase. DNAase is a protein that can digest DNA. The cell membrane is dissolved by the detergent, exposing the cellular material. The addition of proteinase K causes enzymatic reactions and digests proteins that complex with DNA. Phenol extraction is used to denature the proteins and lipids yielding a clear aqueous solution of DNA. Ethanol precipitation dehydrates and precipitates DNA.

In DNA sequencing, fragments of DNA need to be a few kilobases long. One way to obtain shorter DNA from chromosomal DNA is by randomly cleaving the DNA with DNAase. The individual components are fractionated and libraries of these fragments are built. Vectors are used to amplify the DNA fragments. The DNA fragment is inserted into a vector. Examples of vectors are plasmids and bacteriophages. Plasmids are small self-replicating DNA, and bacteriophages are similar to viruses. A commonly used vector is M13, a bacteriophage. A plasmid contains a large number of unique cleavage sites into which DNA fragments generated by an endonuclease restriction digestion can be inserted. The vectors are transfected into host cells, where they live in symbiotic relationship. Vectors multiply within the host, creating their copies which include the inserted fragment. The host cells also multiply. As a result, the inserted fragment of DNA is highly replicated. The amplified DNA is purified for further processing.

Sequencing Reaction

Sanger's method [1] is the most commonly used method of determining the sequence of nucleotides in DNA (Figure 1). DNA polymerase is used to transcribe specific regions of the DNA under controlled conditions. Inhibitors terminate the newly synthesized chains at specific residues. 2',3'-dideoxythymidine triphosphate (ddTTP) added on to the growing chain instead of thymidylic acid inhibits on DNA polymerase and prevents further extension of the chain. Thus termination occurs specifically at positions where dT should be incorporated. A primer and template are incubated with a DNA polymerase in the presence of a mixture of ddTTP and dTTP, as well as three of the other three deoxyribonucleoside triphosphates (dNTP), producing a mixture of fragments all having the same 5' and with ddT residues at the 3' ends. When this mixture is fractionated by electrophoresis on denaturing acrylamide gels, the pattern of bands shows the distribution of dTs in the newly synthesized DNA. By using analogous terminators for the other nucleotides in separate incubations and running the samples in parallel on the gel, a pattern of bands is obtained from which the sequence can be read off.

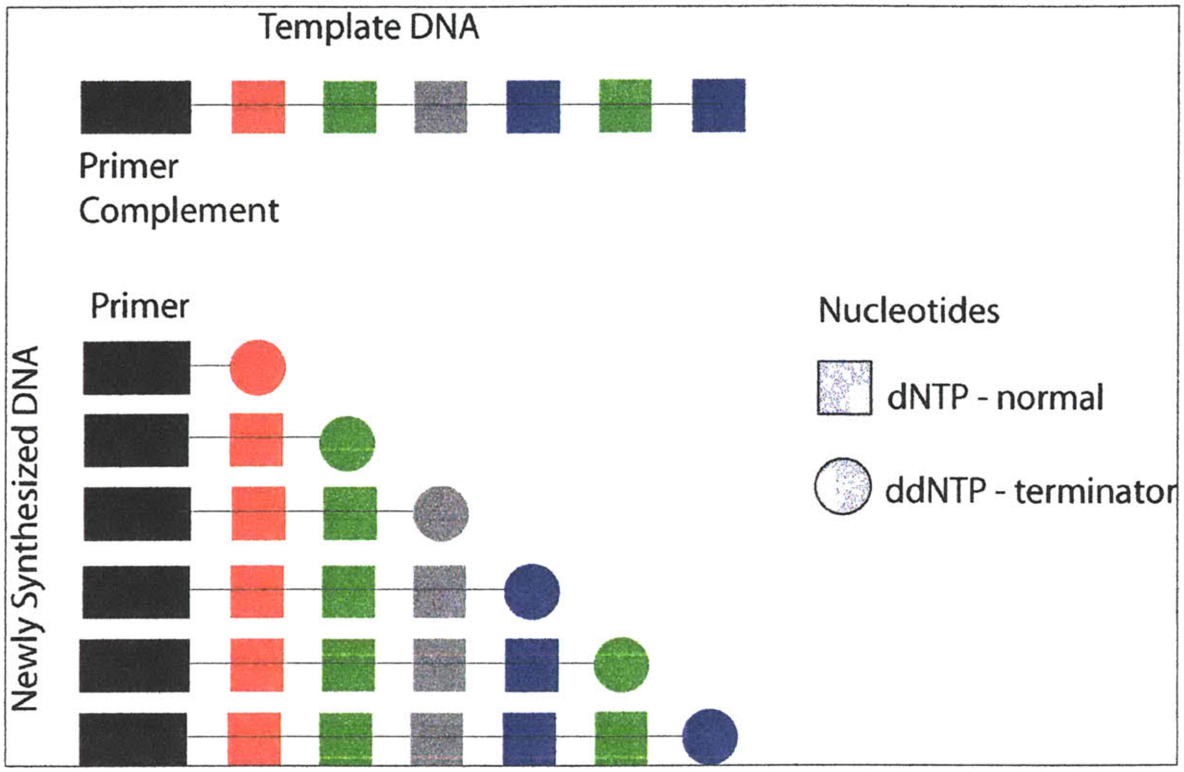

Figure 1. Sanger Sequencing Reaction Products.

Partial copies of the original sequence are made such that fragments differ from each other by one base pair. Addition of a terminator prevents synthesis of further bases to a fragment.

Sample Purification

Sequencing reactions yield DNA samples that are high in salt content, especially magnesium chloride. Two methods are used to purify the DNA sample, namely ethanol precipitation and spin column purification.

Ethanol precipitation [12] is a method of concentrating DNA by precipitation with ethanol. The precipitate of DNA, which is allowed to form at low temperature (-20°C or less) in the presence of moderate amounts of monovalent cations, is recovered by centrifugation and redissolved in an appropriate buffer at the desired concentration. The technique is rapid and quantitative even with nanogram quantities of DNA.

Spin column [12] purification is a useful method when several preparations of DNA are labeled simultaneously or when it is necessary to change the buffer in which the DNA is dissolved. The bottom of a disposable syringe is plugged with a small amount of sterile glass wool. A column of Sephadex G-50 is compacted by centrifuging. Sephadex is a gel-like substance that has a stronger affinity for smaller molecules. When the DNA sample is applied to the column and centrifuged, the impurities are absorbed by the sephadex, and the effluent from the syringe is collected. The unincorporated dNTPs remain in the syringe and the labeled DNA is collected from the decapped Eppendorf tube.

Experience at the BioMEMS laboratory indicates that of the two DNA sample purification protocols, spin column purification yields more consistent results compared with ethanol precipitation.

Microfabricated Device

Channel structures are fabricated on glass wafers with photolithography and chemical etching methods similar to the procedure described by Manz et al. [13]. The etched channels are on average 90 μm wide and 40 μm deep. A second wafer is thermally bonded to the etched wafer to enclose the channels. Each silica wafer is 1.1 mm thick, so the bonded device is 2.2 mm thick. Individual separation devices are 12 cm long and 2 cm wide. The separation channel has a volume of 0.5 μL. Access to the channel ends is provided by 200 μm diameter holes laser-drilled through the etched wafer with a CO_2 laser drilling system [6]. Reservoirs of 50 μL are formed around each hole by affixing 5 mm tall and 3 mm diameter glass rings with optical cement. These reservoirs hold the appropriate sample or buffer solutions into which the electrode is submerged.

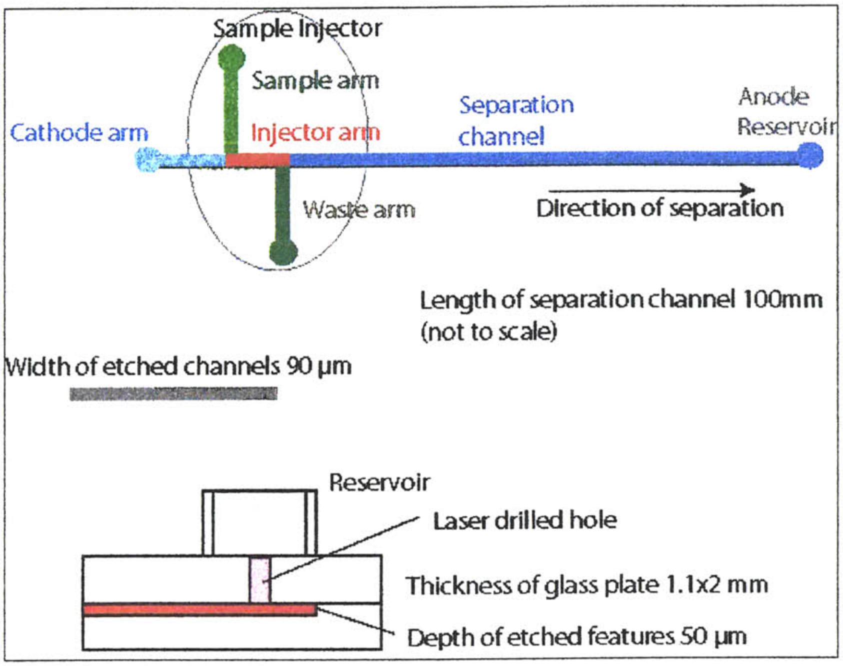

Figure 2. Geometry of Micro-Device

The sample is loaded from the sample well. It occupies the regions including the sample arm, injector arm and the waste arm. Along the direction of the separation channel, the sample is in the injector arm, sandwiched between the buffer in the cathode arm and the separation channel.

The separation device is primarily a 12 cm long channel. There are two electrodes, one at the start and one at the end, as shown in Figure 2. For a negatively charged sample species, as in the case of DNA, the electrode close to the start is negative and the electrode at the end of the separation chamber is positive. Before separation can be performed, the sample has to be introduced into the separation chamber from the sample reservoir by means of a sample injector. A double-T injector is used. The injector is near the start of the separation channel between two shorter channels or arms which are perpendicular to the main channel. The sample arm is the channel from the sample reservoir to the injector. Similarly, the waste arm is the channel from the waste reservoir to the injector. The combined length of the sample and waste channels is 5.5 mm. The injector offset is the distance between the centers of sample and waste injectors. Typical offsets used in the BioMEMS lab are 150 µm, 250 µm, 350µm or 500 µm, although some devices with no offset have also been occasionally tested. The length of the injector is the sum of the offset and the channel width. A 350 µm injector offset with a 90 µm channel width forms a 440 µm injector.

The sample is placed in the sample reservoir and introduced electrokinetically into the device by applying a high potential at the waste reservoir with respect to the sample reservoir. The sample moves electrokinetically from the sample reservoir to the sample arm, along the injector arm, through the waste arm and finally into the waste reservoir. The separation channel is the channel where the sample moves out of the injector and undergoes separation.

Sample injection into the separation chamber is carried out by application of a potential between the start and end reservoirs. The sample plug from the injector arm moves forward into the separation channel. No potential is applied at the sample and waste arms. After the sample has moved out of the injector, pullback voltages are applied at the sample and waste electrodes. This prevents leakage of the sample from those two arms into the injector.

To prevent electroosmotic flow [14], the inner walls of the microfabricated channels are coated with a solution of low molecular weight linear polyacrylamide (LPA) using a modified Hjerten procedure [15]. The sieving matrix loaded into the channel is another LPA solution of 3×10^9 Da synthesized in the laboratory. Separation matrix preparation protocols have been described by Carillo [16]. Solutions of 2% w/w LPA are prepared using 1xTTE (50 mM Tris, 50 mM TAPS, 2 mM EDTA) with 7 M urea. The 2% LPA solution is used for its superior separation properties. The TTE buffer is a standard electrophoresis running buffer. Urea maintains denaturing conditions so that DNA exists as single stranded.

Experimental Protocol

During pre-electrophoresis, the sample reservoir is filled with water and a a potential is applied between the sample and waste reservoirs. Pre-electrophoresis is performed at 300 V/cm for 3 minutes before each sample loading. The sequencing samples are electrophoresed for 2 minutes at 200 V/cm across the separation channel, and a 20 V/cm pullback is applied to both side channels to prevent leakage of excess sample into the separation channel. All separations are performed at 50 °C.

Detection Methods

The results of separation of the different sample components are determined by two methods of detection. In the first method, the sample is run on a slab gel and at the end of separation, and the bands of the different components are imaged. The way to image them depends on the type of tagging used. Some samples are imaged using radiolabeling, and some are tagged with visible dyes. A snapshot of all the separated components at the end is used to determine their nature. This may be called the one time all position (OTAP) detection approach.

In high-throughput automated approaches, a detector is placed at the end of the separation chamber and the passing bands are imaged over time. Unlike the previous case where all the bands were imaged at one time, the detection is done nearly continuously over the entire time of separation. The position of the detector is kept constant. Typically, this mode is used with fluorescence tagged DNA and a laser-induced detection system. This may be called an all time one position (ATOP) detection approach. A schematic of a typical detection system is shown in Figure 3.

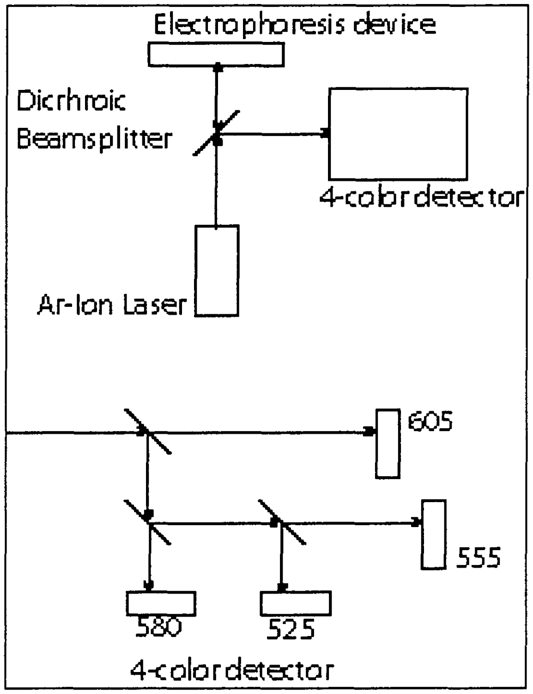

Figure 3. Detector Schematic.

Upper: laser source, beamsplitter, electrophoresis device and the detector. Lower: schematic of a four color detector. The all time one position approach is used.

In Sanger's original method [1], radiolabeling was used to visualize the bands. This method in conjunction with slab gel electrophoresis is commonly used in laboratory benches for scientific research. The use of fluorescent dyes in DNA sequencing is attributed to Lloyd Smith [17]. Another major development in the field was the introduction of energy transfer (ET) dyes developed by Mathies [18]. A recent innovation has been the development of Big Dye terminators which have better mobility characteristics [19].

The fluorophores are attached to the DNA molecules either at the primer or terminator. The use of tagged terminators involves a single reaction chamber which simplifies the process. When the DNA with the fluorophores pass the detection area, they are excited by the laser beam focused at that point. The fluorophores are excited to a higher energy level, and when they return to their ground state, they emit fluorescent light. The light is collected by an objective, and the excitation wavelengths are filtered out. This light is sent to the four-color detector. The four color detector may be implemented in different ways, and one realization is shown in Figure 3 b. The incoming light is filtered using long wavelength pass filters so that the beam is divided into the four components of interest. In the configuration used in the BioMEMS lab, an Ar-Ion laser source is used. This is a source of 488 nm and 514 nm wavelengths of light. The laser induced fluorescence is collected and filtered to remove the components of the excitation frequency, and the light is further filtered using dichroic filters to divide the beam into the constituents of the four dyes. The bands of wavelengths centered around 525 nm, 555 nm, 580 nm, and 605 nm are collected on photomultiplier tubes (PMTs). The PMTs serve as transducers that convert the light signal to electronic signals. These signals are amplified and appropriately filtered to remove noise, and the data is stored.

Data Analysis

The saved data of signals from the PMTs has the sequence information embedded within it. The extraction of the base sequence information is called base calling. Base calling consists of four steps. First, the signal is subjected to baseline correction to take into effect any drift in the signal. Due to the relative difference in mobility caused by the four different dyes, a mobility correction is applied. Furthermore, the four dyes have overlapping ranges of emitted frequencies.

This causes cross-talk between the four channels of data. Correct occurs is by transforming from color to base coordinates. A detailed treatment of this step is available in [20]. Once the transformation is performed, it is also advantageous to evaluate the quality of the sequence information. A further step which may be of importance in shotgun sequencing is the assembly of the different fragment sequences to yield the chromosome sequence. With the completion of the base calling step the sequence of the bases in the DNA fragment is obtained, and the fragment is said to be sequenced.

5. Other applications of DNA electrophoresis

DNA Typing

Specific markers in DNA can help to accurately identify a person [21]. These markers are short tandem repeat (STR) polymorphisms each of which may have a known maximum number of copies. These features being hereditary, DNA typing also has applications is determining parental identity, particularly paternity. There has been an increasing need for DNA typing of felons. Countries, including the United States and United Kingdom, are developing national DNA data bases. The US data-base [22] called the Combined DNA Index System (CODIS), has information on 13 specific loci, namely CSF1PO, FGA, TH01, TPOX, vWA, D3S1358, D5S818, D7S820, D8S1179, D13S317, D16S539, D18S51, and D21S11 and AMEL or the sex chromosome. All CODIS STRs are tetrameric repeat sequences, *i.e.* they can have within them up to four repeats of a known fragment within it.

SNP Detection

Single nucleotide polymorphisms are variations in the sequence of different individuals of a species. These variations may be markers for susceptibility to diseases. Due to their biological significance, their identification and comparative study are extremely important. DNA sequencing using microcapillaries can potentially play an important role in this effort.

6. Trends in Miniaturization and Automation

Capillary Electrophoresis

The conventional method for bench top electrophoresis is slab gel electrophoresis, where a gel is cast in a chamber and used as a separation medium for electrophoresis. The efficiency of separation is limited by thermal gradients across a chamber. The temperature profile across a channel from the periphery to the center is quadratic. The difference in temperature can cause internal convection and differences in sample mobility. In theory, electromigration mobility is independent of temperature while diffusion is proportional to temperature. However, the electrophoretic mobility of polymers which undergo molecular sieving in separation matrices can be a function of temperature.

The efficiency of separation is measured by the number of theoretical plates

$$N = \frac{\mu V}{2D} \tag{1.1}$$

where μ is the sample mobility, V is the applied voltage, and D is the diffusion coefficient of the sample in the separation channel. The theoretical plate number is a measure of the spreading of a sharp initial peak of sample as it reaches the end of the separation chamber. As applied voltage is increased, the separation efficiency increases. The migration time is $t = \frac{L^2}{\mu V}$, where L is the length of the channel. As the column length increases, the separation times increase and so does the effect of diffusion since the variance die to diffusion is $\sigma_D^2 = 2Dt$. Tiselius [23] had predicted that the efficiency of separation could be improved by reducing the channel width. The reduction in the channel diameter reduces the temperature variation across the channel. This temperature difference causes a difference in the effective mobility of DNA across the channel, increasing the effective diffusion of the sample in the channel. This was the motivation for reducing the scale of operation of electrophoresis from the slab gel format. The first notable success in capillary electrophoresis device was by Jorgenson and Lukacs [24]. Typical applied voltages were 30 kV across a 100 cm capillary of 150 μm diameter. Today, high throughput sequencing is routinely done on capillary based systems and further improvement of this technique is an area of current research [16].

Microdevice Development

Techniques developed for silicon micromachining for the computer chip industry were modified and applied to building a device for electrophoresis. The width of the microfabricated channels were 2-3 times less than the dimensions of capillaries, with implications for superior separation. Another advantage of using micromachined channels for electrophoresis was that it had potential for integrating with other subsystems to form a total analysis system (TAS). An embodiment of a TAS concept is a device that can perform sample collection, transport, reaction, separation and detection. As a first step in this context, Manz, *et al.* [13] announced the development of a microdevice for electrophoresis. Their analysis predicted fundamental process improvements with scaling down the process of electrophoresis. These advances were adapted by Mathies et al. [25] and Schmalzing et al. [6] to apply DNA electrophoresis on micro-devices. Typical devices developed at the BioMEMS laboratory have been described earlier.

Automation

Sequencers have been developed by several researchers [17, 26-29] for automated electrophoresis, raw data acquisition and base-calling. The automation is in the area of sample preparation [30], handling and delivery with robotics and suitable end-effectors, as well as process operation and control. Laser-induced fluorescence detection and base-calling software development have been instrumental in the development of automated systems for DNA diagnostics, the first of which was developed by Hood et al. [31]. These systems revolutionized the speed of sequencing and helped the Human Genome Sequencing project be completed ahead of schedule [32].

7. Investigation of DNA Sample Injection

Video microscopy of microcapillary electrophoresis was performed in an effort to understand the process of sample injection in DNA electrophoresis. The experiments of video microscopy of DNA motion in the injector region of microfabricated electrophoresis channels were previously performed BioMEMS lab [5]. The experiments are briefly described here and detailed experimental protocols are shown in Appendix 3.

Experimental Method

DNA sequencing reaction products are loaded into the cross injector by applying a negative potential of 165 V (corresponding to 300 V/cm) to the sample reservoir while keeping the waste reservoir at ground voltage. During sample loading, the voltage in the anode and cathode reservoirs were left floating. A pullback voltage of 20 V/cm is applied to limit leakage of sample from the sample and waste arms into the separation channel. In all experiments, a voltage of between 20 V/cm and 850 V/cm was applied for 5 seconds during electrophoretic injection and then changed to the standard 150 V/cm using a voltage relay switch for further electrophoresis.

The sequence of key steps is outlined. 1) Pre-electrophoresis is performed with water in the sample reservoir and buffer in the waste reservoir for 180 seconds. 2) The sample is introduced from the sample region into the injector for 180 seconds. 3) The sample was injected for 10 seconds. During this time, no pullback voltage is applied at the sample and waste electrodes. 4) The pullback voltage is applied at the sample and waste electrodes, and the sample from injector injected for 30 seconds. The last voltage condition is maintained until the end of separation. For the high voltage injection studies, the applied high voltage is applied for 5 seconds before reverting to the regular voltage. The pullback voltage is applied subsequently.

The sample, stained with propidium iodide dye, was imaged during electrophoretic injections using a 10X objective of an inverted, epi-fluorescence microscope (Nikon TE 3000). The microscope was equipped with filter cubes (Nikon 34-TA47) for image enhancement, a CCD camera (Orca-Hamamatsu 54327) for image capturing, and a mercury lamp for the illumination of samples. The CCD camera took images at 8 frames/second using a standard time lapse protocol. This data was converted into 8 bit digital images utilizing 256 gray scale. Details of the method can be found in [5], [33].

8. Current Models for DNA Electrophoresis

Although the theory of electrophoresis has developed considerably over the last two decades, there has been little work on developing a comprehensive model for DNA sequencing. Perhaps the most significant work so far in modeling DNA electrophoresis has been a study on the study of resolution of DNA separation [8]. The premise of that study was that electrophoresis of DNA is governed by two processes: (1) separation of distinct species due to difference in mobility, and (2) the diffusion of sample components over time. The resolution was determined by a net diffusion of the components in the sample plug. In other words, the model assumed that all sample components have a similar concentration profile, and it predicts how the sample moves down the separation channel with diffusive effects. This model worked well for the special case when the choice of a buffer minimized sample stacking, a condition satisfied in that study. The larger question of the effect of sample injection was not well understood. In a related study on DNA sequencing using microfabricated devices [6], it was shown that the sizes of estimated sample plug from a geometric reasoning standpoint, and those predicted by applying the Luckey [8] resolution analysis model were inconsistent.

It was noted [6] that "We observed a discrepancy between the measured injection length and the geometrically defined injector size to a highly efficient stacking process occurring in our device during injection. A plausible explanation is that, during the electrokinetic loading process, the ions of the sequencing are depleted at the injection (the DNA samples were dissolved in deionized water). As soon as the voltages are switched, most of the separation voltage is dropped over the short injector segment of high electrical resistance, leading to effective stacking." The existence of sample stacking in DNA electrophoresis was established. These findings opened up the question of the nature of sample stacking in electrophoresis. The field-amplified model for DNA stacking was proposed [6]. It was argued that the sample conductivity is lower than the buffer conductivity, and the process of pre-electrophoresis was depleting the injector region of charge carriers which made the sample effectively be loaded in a dilute buffer.

The effect of sample stacking of DNA is of greater importance in microfabricated devices which rely on electokinetic sample loading. In a following study [33], video microscopy based images were obtained to look at the profile of sample concentration (tagged with propidium iodide) during the process of sample loading and injection in a microfabricated channel. The results demonstrated that sample stacking was significant. Two types of samples were used in separate experiments: 500 b long DNA and sequencing reaction mixtures. These experiments revealed a surprising pattern of the sample concentration profiles as they developed. The peaks were at the rear of the sample plug, an emphatic rejection of field amplified stacking which was proposed as a model for DNA stacking. An attempt was made to understand this phenomenon [5]. However, the new model lacked physical reasoning and had serious predictive limitations.

The model presented in this thesis presents A model for the mode of stacking as observed in DNA electrophoresis has been developed in this thesis, which presents a viable alternative the previous theories. This thesis bridges the gap between experimental observations and a physical understanding of the phenomena. This model, although developed independently, is similar to stacking models reported by Gebauer et al. [34], [35]. The mode of sample stacking and the reasons for it have been explained in Chapter 2.

Chapter 2. Electrophoresis Modeling

1. Electrophoresis

In the original sequencing method developed by Sanger [1], slab gel electrophoresis was used for separation of different sized fragments of DNA. Tiselius [23] had demonstrated the usefulness of electrophoretic techniques for the analysis of protein mixtures with a moving boundary apparatus to resolve human serum proteins into albumin and four globulin fractions, α_1, α_2, β, and γ. The discovery gave rise to new instruments and techniques with ever increasing resolution.

Most materials in aqueous solution acquire an electrical charge due to ionization and therefore move in response to an electric field. The charged entities may be simple ions, complex macromolecules, colloids or living cells. The rate of migration depends on the amount of charge, the size and shape of the particle, and the properties of the solvent.

Mobility and Diffusion

Electrophoresis depends on two important parameters – mobility and diffusion. Mobility is proportional to the speed of the particle under the action of an electric field

$$v = \mu z E \tag{2.1}$$

where v is the velocity in m/s, μ is the mobility in m^2/sV, z is the valence, E is the electric field intensity in V/m.

The mobility of a particle is used to predict the steady state velocity of the particle. However, the transient speed of the particle is in general neglected. Why is this a reasonable assumption? It is justified by the fact that the time required for the molecule to move from rest to achieve steady state by the application of an electric field, is very small compared with the time of travel in common electrophoresis applications. Details of an analysis of response time are given in Appendix 10.

Diffusion is a process by which matter is transported due to the exchange of momentum from random molecular motion. Diffusion is modeled by Fick's law, which states that the net flux of a molecular species is proportional to the product of the diffusion coefficient and the concentration gradient. From a fundamental standpoint, diffusion scales as the product of the mean free path length and the mean speed between collisions

$$\Gamma = -D\frac{\partial c}{\partial x} \tag{2.2}$$

where Γ is the flux, D is the diffusion coefficient, c is the concentration, and x is the spatial distance.

The relationship between mobility and diffusion has been explained and encapsulated in the Einstein equation. This equation states that

$$D = \mu\frac{RT}{F} \tag{2.3}$$

where μ is the mobility, R is the universal gas constant, and F is the faraday number.

The ratio $\frac{D}{\mu} = \frac{RT}{F}$ is then a constant. For an ion in solution, for example the chloride ion, this ratio is $\frac{D}{\mu} = \frac{8.314\times 323}{98500} = \frac{1}{36.6}$. The ratio of diffusion coefficient to mobility of DNA for a 1000 base strand is

$$\frac{D}{\mu} \approx \frac{1\times 10^{-12}}{5\times 10^{-9}} = 2\times 10^{-4} = \frac{1}{5000}. \tag{2.4}$$

The ratio of diffusion to mobility is two orders of magnitude different for an ion like chloride and a DNA ion. The reason for this difference is that the mechanism of motion of DNA is fundamentally different from the motion of other ions. Diffusion in polymer transport undergoing sieving consists of interaction between the matrix and the polymer ion and result in molecules getting trapped in some positions, needing higher energy to restart motion. Since a molecule can undergo reptation, and if one end is trapped, another part can continue to move ahead. Presumably, this why the randomness associated with polymer ion transport is reduced. As a result, diffusion to mobility ratio for polymer ions is much lower than the similar ratio of regular ions, and the Einstein equation is not valid for polymer ions. The nature of molecular interactions between the DNA molecules and the gel matrix is a subject of active research, as shown in a review by Viovy [36].

For a DNA molecule, the charge to size ratio is nearly constant. The classical idea of mobility as a function of size is discussed in Appendix 10. MobilityIf the classical model for mobility had been applicable to DNA, DNA molecules would all have a similar value of mobility. Both Sanger [1] and Gilbert [37] , who invented methods for DNA sequencing in 1977, used electrophoresis to separate DNA based on size. Lerman and Frisch [38] explained the reason for the dependence of DNA size on mobility in 1982. Lumpkin and Zimm [39] also independently explained this dependence from first principles. The basis of the reasoning is that DNA is a worm-like polymer and its geometry is fundamentally different from a spherical particle. Lumpkin and Zimm's [39] analysis has been presented in Appendix 8. DNA Mobility as a Function of SizeDNA diffusion in microcapillary electrophoresis has been reported by Schmalzing [6]. DNA diffusion coefficients tend to be low due to the nature of the interaction between the polymer ion and the sieving matrix.

Description of Four Types of Electrophoresis

The process of electrophoresis can be classified into four general modes: zone electrophoresis (ZE), moving boundary electrophoresis (MBE), isotachophoresis (ITP), and isoelectric focusing (IEF). Prior to 1983, separate theories were used to explain each mode or technique, predicated on conditions too restrictive for generalization. These theories were unified by Bier et al. [40] who developed a single, general quantitative theory.

Zone Electrophoresis

This is the simplest and most commonly used method of electrophoresis. The electric field is nearly uniform in the separation domain, and particles move at a speed proportional to their mobility. The sample occupies a small portion of the column and complete separation of the sample constituents is possible. ZE is carried out in homogeneous buffer systems. As the sample moves along, it also undergoes spreading due to diffusion. Tools for resolution analysis of separation in ZE have been presented by Luckey et al. [8].

Moving Boundary Electrophoresis

In moving boundary electrophoresis (MBE), the sample forms stable moving boundaries which maintain their form. In capillary electrophoresis (CE) devices used for MBE, all analytes are co-ions and there is one common counter-ion. Across each moving boundary, one component is absent on one side. Complete separation of the components is not achieved in MBE. The fastest component forms the leading boundary and the slowest component forms the trailing boundary. MBE is carried out in homogeneous buffer systems. The migration rate of the moving boundaries formed by the components of different mobility values is the key parameter.

Isotachophoresis

Isotachophoresis is the term applied to particles moving under electrophoresis at equal speed. The analytes are all are co-ions, and there is one common counter-ion present in the separation column. Once transient separation takes place, the analyte separates into bands, and their concentration adjusts to new values. For the analytes to move at equal speed, the product of the mobility of each analyte with its local electric field must be equal. The electric field is adjusted by a change in its concentration and hence conductivity. The electric field and conductivity have sharp jumps at each analyte boundary. Discontinuous electrolyte systems must be used in ITP, the sample being inserted between the leading and a terminating electrolyte.

The formation of moving boundaries and steady state isotachophoresis are well understood. The transient phase of isotachophoresis has been explained by Brouwer and Postema [41]. The principal idea is that that every initial boundary with multiple components gives rise to moving boundaries, unless it is a pure concentration boundary. The separation of moving boundaries to form ITP boundaries is a result of interference of the moving boundaries causing separation of each component [41].

Isoelectric Focusing

This method is different from other classical modes of electrophoresis in that it depends on the formation of a stable pH gradient causing the sample constituents to migrate to their isoelectric points. One way to achieve this stable pH gradient or a stable electric field gradient is by depletion or controlled release of the electrolytes at the boundaries. The flux due to diffusion and that due to electromigration balance each other, thus maintaining a stable electric field or pH gradient.

2. *Types of Sample Stacking*

Stacking in zone electrophoresis is of the following general types – field-amplified stacking, isotachophoresis-assisted stacking, sample stacking with major and minor components, and micellar electrokinetic focusing.

In field-amplified stacking [7], the sample is electrokinetically introduced into a separation column with a buffer that is very dilute compared to the running buffer. The electric field due to the applied current or potential depends on the local conductivity of the buffer, which in turn depends on the buffer ion concentration and mobility. Across a buffer concentration boundary, the buffer ion concentrations are higher. A high electric field is set up in the region of lower buffer concentration and *vice versa*. Kohlrausch [42] has shown that a concentration boundary of the same species does not migrate with the application of an electric field. A sharp, initial boundary can only undergo diffusion. The sample concentration is small compared to the buffer concentration so the buffer concentration determines the electric field. The sample responds to the electric field, so sample in the high electric field region moves fast and slows down as it transitions into the low field region. During this transition, the density of the sample increases as predicted by mass conservation. The ratio of the density after transition to the original density is called the stacking ratio:

$$SR = \frac{c_{final}}{c_{initial}} \tag{2.5}$$

The stacking ratio for a species moving from a region A to a region B, with concentrations C_A and C_B, and with speeds as V_A and V_B can also be expressed as

$$SR = \frac{c_B}{c_A} = \frac{v_A}{v_B} \tag{2.6}$$

In a similar method [43] the sample is introduced into the column by hydrodynamic flow, but the stacking process is similar.

In the second type of stacking, namely ITP-assisted stacking or transient ITP stacking, the method takes advantage of the concentrating nature of isotachophoresis [44, 45]. In this method, zone electrophoresis is combined with transient isotachophoresis. In this form of stacking, transient ITP is used to create a series of narrow zones of the sample. The advantage of ITP is the creation of narrow regions of very high stacking ratio due to its self-sharpening boundaries. Once stacking has been established, the leading or trailing electrolyte is appropriately changed, so the ITP process can transition to zone electrophoresis. Some configurations [35] of this process require special instrumentation and cannot be run on commercial capillary electrophoresis systems [34]. The method requires discontinuous buffer systems and its implementation can have two forms: on-column and coupled column arrangements [44]. In the on-column implementation, the leading and trailing buffers are dissimilar, so there is no need for any special instrumentation. However, it puts limitations on the reusability of the buffer.

The third form of sample stacking has been described by Gebauer et al. [34] and [35]. They have described the mode of stacking in which the sample consists of a major and one (or more) minor component(s). Within this type, two forms of stacking are described – sample stacking and sample self-stacking. Details of this method will be explained in a Section 2.12.

A fourth kind of stacking used is micellar electrokinetic chromatography (MEKC), called micellar sweeping [46]. Micellar electrophoresis has not been used in DNA electrophoresis, so this is not considered in detail.

Advantage of Sample Stacking

Sample stacking is extremely advantageous in separation. It causes a sample plug to become more concentrated causing enhanced detection signal-to-noise ratio. The components in the compact sample plug can be separated at a shorter distance, causing faster separation. The latter is also better because of decreased diffusion. With instrumentation and detection parameters held constant, sample stacking enhances the performance of electrophoretic separation. Sample stacking is also of tremendous importance also when the concentration of the sample by biochemical methods takes considerable effort.

3. *Review of Electrophoresis Modeling*

Electrophoresis is the transport of species under the action of an electric field. This method is used for the separation of analyte components based on the difference in their mobility. Electrophoresis is modeled by transport equations, which are also a form of conservation laws:

$$\frac{\partial c_i}{\partial t} + \frac{\partial \Gamma}{\partial x} = 0, \tag{2.7}$$

where c_i is the concentration of the species in mol/m^3 and Γ is the flux in mol/m^{2}s.

The number of conservation laws corresponds to the number of species involved in the system. In general, the conservation laws also have reaction and generation (or sink and source) terms, however, these effects are assumed to be negligible in the model for sample stacking. Considering two mechanisms of transport, advection (Γ_a) and diffusion (Γ_D), the conservation yields:

$$\frac{\partial c_i}{\partial t} + \frac{\partial}{\partial x}(\Gamma_a + \Gamma_D) = 0 \tag{2.8}$$

The flux due to advection is

$$\Gamma_a = v_i c_i \tag{2.9}$$

where the velocity of the species *i* is represented by v_i, and the flux due to diffusion is

$$\Gamma_D = -D_i \frac{\partial c_i}{\partial x} \tag{2.10}$$

which is a form of Fick's law of diffusion where D_i is the coefficient of diffusion of component *i*. Substituting these fluxes in the transport equation, we get

$$\frac{\partial c_i}{\partial t} + \frac{\partial}{\partial x}(v_i c_i - D_i \frac{\partial c_i}{\partial x}) = 0. \tag{2.11}$$

The relationship between the velocity of a particle (of species *i*), and the electric field (E) is

$$v_i = \mu_i z_i E. \tag{2.12}$$

where v_i is the velocity in m/s, μ_i is the mobility in m^2/sV, z_i is the valence, E is the electric field intensity in V/m. {When z=1, the velocity is $v = \mu E$. If the charge on the species is negative, $z = -1$ the velocity direction is reversed, and $v = -\mu E$.} Incorporating this constitutive relationship, the conservation laws have the form

$$\frac{\partial c_i}{\partial t} + \frac{\partial}{\partial x}(\mu_i c_i E - D_i \frac{\partial c_i}{\partial x}) = 0, \tag{2.13}$$

Consider a system with three species represented 1, 2, and 3:

$$\begin{aligned} \frac{\partial c_1}{\partial t} + \frac{\partial}{\partial x}(-\mu_1 c_1 E - D_1 \frac{\partial c_1}{\partial x}) = 0 \\ \frac{\partial c_2}{\partial t} + \frac{\partial}{\partial x}(-\mu_2 c_2 E - D_2 \frac{\partial c_2}{\partial x}) = 0 \\ \frac{\partial c_3}{\partial t} + \frac{\partial}{\partial x}(\mu_3 c_3 E - D_3 \frac{\partial c_3}{\partial x}) = 0 \end{aligned} \tag{2.14}$$

Since 1 and 2 are negatively charged anions, their advective terms show the mobility with a negative sign. The conservation laws are coupled by the electric field intensity *E*, which may be solved for by making use of Gauss' Law:

$$\nabla \cdot (\varepsilon_r E) = \frac{F(z_1 c_1 + z_2 c_2 + z_3 c_3)}{\varepsilon_0}. \tag{2.15}$$

where *F* is the Faraday Number and *F* = 96500 C/equivalent.

It is common practice in electrophoresis to assume charge neutrality [40].

$$z_1 c_1 + z_2 c_2 + z_3 c_3 = 0 \tag{2.16}$$

With the charge neutrality assumption, Gauss' equation becomes:

$$\nabla \cdot (\varepsilon_r E) = 0 . \tag{2.17}$$

Charge neutrality is consistent with a solenoidal electric field, or $\nabla \cdot E = 0$. This means that when there is no variation in the electric field, charge neutrality is guaranteed. However, it also means that when the electric field has sharp gradients, charge neutrality is not an accurate assumption.

This equation is insufficient to capture the effect of regions of varying conductivity. The effect of the varying conductivity may be incorporated by assuming Ohm's law which states that

$$\vec{J} = \sigma \vec{E} \text{ or } \vec{E} = \frac{\vec{J}}{\sigma} . \tag{2.18}$$

where σ is the conductivity. The validity of the charge neutrality assumption in electrophoresis was addressed by Fife *et al.* [47] who theoretically showed that the traveling wave solution of moving boundaries was possible under typical electrophoretic condition, even with the charge neutrality assumption. Applying the charge conservation equation:

$$\frac{\partial \rho}{\partial t} + \nabla \cdot \vec{J} = 0 . \tag{2.19}$$

Assuming that the charge flux is much larger than the rate of change of charge density,

$$\left| \frac{\partial \rho}{\partial t} \right| << \left| \nabla \cdot (\vec{J}) \right| \tag{2.20}$$

equation (A.8) reduces to

$$\nabla \cdot (\vec{J}) = 0 . \tag{2.21}$$

Neglecting the diffusion component of the current density and substituting Ohm's law, into (2.21) results in

$$\nabla \cdot (\sigma \vec{E}) = 0 . \tag{2.22}$$

The one dimensional form of equation (2.22) is

$$\frac{\partial (\sigma E)}{\partial x} = 0 , \tag{2.23}$$

and the two dimensional form is

$$\frac{\partial (\sigma E_x)}{\partial x} + \frac{\partial (\sigma E_y)}{\partial y} = 0 . \tag{2.24}$$

The conductivity σ (S/m) has contributions from the medium and the charges in the medium. In electrophoresis, the medium is water, but when the pH is close to 7 the dominant contribution of charges are the ions from the dissociation of salts/buffers (the electrolytes). Water also dissociates into H^+ and OH^- ions, but at pH 8.1 the dissociation may be neglected. The conductivity σ is a function of the concentrations, valence and mobility of ions.

The current density is a charge flux term:

$$J = \sum \rho_i v_i \,, \tag{2.25}$$

where $\rho_j = z_j c_j F$ and $v_j = \mu_j z_j E$.

$$J = \sum_j \left(z_j c_j F \cdot z_j \mu_j E \right) \tag{2.26}$$

$$J = \sum_j \left(z_j^2 c_j \mu_j F E \right) = \left[\sum_j \left(z_j^2 c_j \mu_j F \right) \right] E \tag{2.27}$$

Conductivity may be derived from Ohm's law:

$$J = \sigma E \tag{2.28}$$

Therefore, $\sigma = \sum_j z_j^2 c_j \mu_j F = F \sum_j z_j^2 \mu_j c_j = F\left(z_1^2 \mu_1 c_1 + z_2^2 \mu_2 c_2 + z_3^2 \mu_3 c_3 \right)$ (2.29)

The electric field may be expressed as

$$E = \frac{J}{\sigma} = \frac{J}{F\left(z_1^2 \mu_1 c_1 + z_2^2 \mu_2 c_2 + z_3^2 \mu_3 c_3 \right)} \tag{2.30}$$

For a uniform conductivity and equation (2.28), $\nabla \cdot (\vec{E}) = 0$ is obtained. Comparison with Gauss' law, $\nabla \cdot (\varepsilon \vec{E}) = \rho$, implies that for a region of uniform conductivity, the charge density is identically 0.

For a region with a non-uniform conductivity distribution, the equation $\nabla \cdot (\sigma \vec{E}) = 0$ may be expanded to $\sigma \nabla \cdot \vec{E} + (\nabla \sigma) \cdot \vec{E} = 0$ or $\nabla \cdot \vec{E} = -\frac{(\nabla \sigma) \cdot \vec{E}}{\sigma}$. Comparing with Gauss' Law, $\nabla \cdot \vec{E} = \rho / \varepsilon$, it can be seen that the non-uniform conductivity field gives rise to charge accumulation at regions of conductivity gradients. This is shown graphically in Figure 4. Charge neutrality is therefore valid for regions of uniform conductivity but not true for regions of conductivity changes. Also, the assumption $\nabla \cdot (\sigma \bar{E}) = 0$ is not equivalent to assuming charge neutrality.

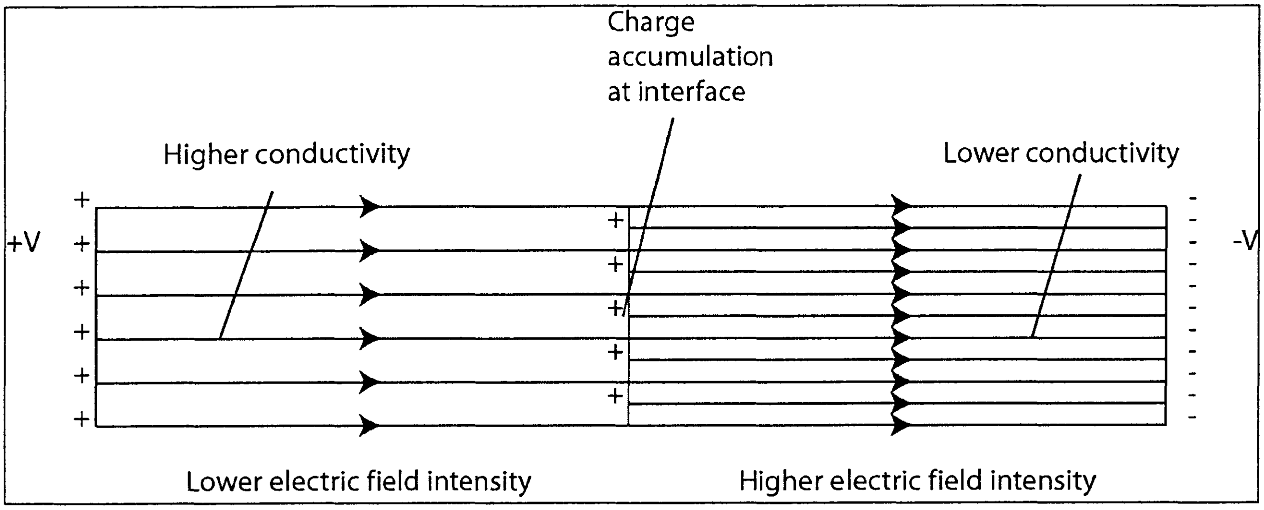

Figure 4. Electric field variation in region of non-uniform conductivity.

A change in conductivity results in a change in the electric field along a channel. A higher density of field lines indicates higher electric field. Charge accumulation occurs at the interface and this accounts for the difference in the electric field.

Time Scales

The time scale of the experimental observation is 0.01 s. The charge relaxation time scale for water is

$\tau_e = \varepsilon / \sigma \Rightarrow \tau_e = 80\varepsilon_o / \sigma \Rightarrow \tau_e = 80 \times 8.85 \times 10^{-12} / 10^{-3} \times 10^5 \times 80 \times 10^{-9} s \Rightarrow \tau_e = 80 \times 10^{-6}$ s.

Hence, in this case, charge relaxation occurs very fast. After that, a quasi-steady state is reached so that $\nabla \cdot (\sigma \bar{E}) = 0$ is valid. The time scale of consideration is two orders slower than the dynamics of charge relaxation.

4. Theory of Moving Salt Boundaries in Electrophoresis

Moving boundaries are formed by solutions of two salts with a common ion. An example of such a boundary could be KCl and KI. Here the co-ions are chloride and iodide and the common counter ion is potassium. When an electric current is passed through the system such that the two salt solutions are initially separated and the direction of the applied voltage is such that chloride ion moves away from this boundary and iodide moves towards this boundary, a boundary is formed which moves with the leading ions (chloride) in front and the trailing ions (iodide) at the rear. Tiselius [23] showed that the speed of motion of the boundary, v_b, is

$$v_b = J\frac{t_l}{FC_l} \tag{2.31}$$

where t_l is the transference number of the leading ion and C_l is the concentration of the leading ion.

Stationary Boundary

A concentration boundary is one where the constituents are the same on either side of the boundary, but their concentration is different. Consider a concentration boundary with two identical constituents on either side, the sides being A and B as shown in Figure 5. Let the constituents be species s_1 and species s_2. Assume charge neutrality and also assume the valences as $z_1 = 1; z_2 = -1$. The conductivity on both sides may be expressed as $\sigma_A = Fc_A(\mu_1 + \mu_2)$ and $\sigma_B = Fc_B(\mu_1 + \mu_2)$. From Ohm's law, we can express the current densities as

$$J_A = \sigma_A E_A = Fc_A(\mu_1 + \mu_2)E_A \tag{2.32}$$

and

$$J_B = \sigma_B E_B = Fc_B(\mu_1 + \mu_2)E_B \tag{2.33}$$

However, since J = constant everywhere from charge conservation, the current density is equal on either side of the moving boundary. Using $J = J_A = J_B$, results in

$$Fc_A(\mu_1 + \mu_2)E_A = Fc_B(\mu_1 + \mu_2)E_B \tag{2.34}$$

$$c_A E_A = c_B E_B \tag{2.35}$$

Considering a control volume that includes the boundary, and from the Rankine-Hugoniot [48] condition it is predicted that the speed of motion of boundary:

$$(c_A - c_B)v_S = c_A \mu_1 E_A - c_B \mu_1 E_B \tag{2.36}$$

$$(c_A - c_B)v_S = \mu_1 (c_A E_A - c_B E_B) \equiv 0 . \tag{2.37}$$

This condition is true only if

$$v_S \equiv 0 . \tag{2.38}$$

This shows that the boundary speed is identically zero. Hence, this is a stationary boundary.

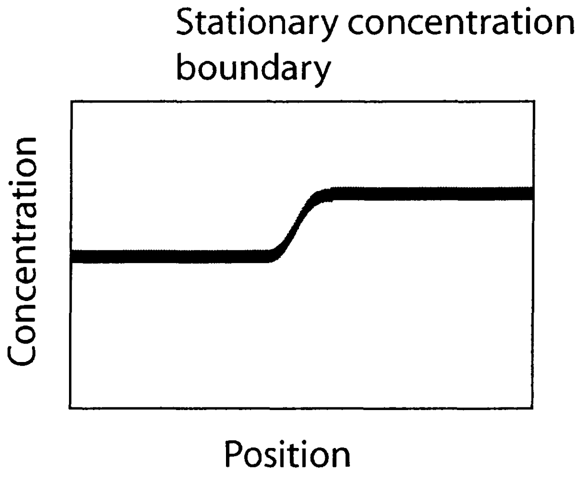

Figure 5. Concentration Boundary

A concentration boundary has the same components with different components on either side of the boundary.

Moving Boundary

A stable moving boundary, along with a stationary concentration boundary, is formed when there is an initial discontinuity across a boundary such that there is a common counter-ion across the boundary and there are distinct co-ions on either side. Consider a boundary such that the two sides are A and B. Let the species on the left side be s_1 and s_3 and the species on the right side be s_2 and s_3. It is assumed that (a) s_1 and s_2 are the co-ions with valence $z_1=z_2=1$, and s_3 is the counter-ion with $z_3=-1$ (b) the mobility of s_2 is greater than the mobility of s_1, or $\mu_2 > \mu_1$ and (c) the applied electric field is such that the faster co-ion (s_2) migrates away from the boundary, while the slower ion (s_1) migrates towards the boundary. The ion s_2 is the leading ion and s_1 is the trailing ion. Under these conditions, a stable moving boundary is formed with equal speeds of the co-ion components on both sides of the boundary. Therefore,

$$v_{1,A} = v_{2,B} \tag{2.39}$$

$$\mu_1 E_A = \mu_2 E_B \tag{2.40}$$

Incorporating Ohm's law:

$$\mu_1 \frac{J}{\sigma_A} = \mu_2 \frac{J}{\sigma_B} \tag{2.41}$$

$$\mu_1 \frac{J}{Fc_A(\mu_1 + \mu_3)} = \mu_2 \frac{J}{Fc_B(\mu_2 + \mu_3)} \tag{2.42}$$

$$\frac{\mu_1}{c_A(\mu_1 + \mu_3)} = \frac{\mu_2}{c_B(\mu_2 + \mu_3)} \tag{2.43}$$

$$\frac{\mu_1}{(\mu_1 + \mu_3)} \frac{(\mu_2 + \mu_3)}{\mu_2} = \frac{c_A}{c_B} \tag{2.44}$$

Define transference numbers as the proportion of the current carried by a particular ionic species

$$t_1 = \frac{\mu_1}{(\mu_1 + \mu_3)} \text{ and } t_2 = \frac{\mu_2}{(\mu_2 + \mu_3)} \tag{2.45}$$

Equation (2.44) is recast as:

$$\frac{c_B}{t_2} = \frac{c_A}{t_1}. \tag{2.46}$$

This is also a form of Kohlrausch's regulation function [42] and demonstrates a term $\left(c_i/t_i\right)$ that is constant across the boundary. From a Riemann problem perspective, this is a Riemann constant since it does not vary across a system discontinuity. To evaluate the speed of the boundary motion, the Rankine-Hugoniot condition is used, which shows that the boundary moves as fast as the ions on both sides. This is a verification of the assumption made earlier in equation (2.39).

$$(c_2 - c_1)v_S = c_2\mu_2 E_2 - c_1\mu_1 E_1 \tag{2.47}$$

$$(c_2 - c_1)v_S = (c_2 - c_1)\mu_1 E_1 \tag{2.48}$$

$$v_S = \mu_1 E_1 \text{ or } v_S = \mu_2 E_2 \tag{2.49}$$

In the case of a moving boundary, the concentration of the leading ion remains as it was initially. However, the relationship $c_A = c_B\left(t_1/t_2\right)$ constrains the value of the concentration of the trailing ion behind the moving boundary. The initial concentration of s_1 is prescribed and in general it may not satisfy the relationship dictated by equation (2.46). As a result, a concentration boundary is created at the original location of the boundary and a new region C is created such that the concentration of s_1 is consistent with the boundary constraint. The constituents across the boundary are s_1 and s_2 and their concentrations are c_A and c_C across the boundary. The concentration boundary remains stationary and a moving boundary is established across regions C and B. The relationship (2.46) between c_A and c_C, is true so that the moving boundary condition is satisfied $c_A = c_C \dfrac{t_1}{t_2}$.

Shape of the Moving Boundary

The two-component boundary can undergo smoothening due to diffusion. This boundary is always stable. It can also be formed with arbitrary (non-zero) values on either side of the boundary. The exact analytical solution of the shape of the boundary was predicted by Weber [49], and experimentally verified by Longsworth [50].

Assume there are three electrolyte species - two co-ions s_1 and s_2 and a counter ion s_3. Start with the following governing equations based on equation (2.14):

$$\begin{aligned}
&\frac{\partial c_1}{\partial t}+\frac{\partial}{\partial x}(z_1\mu_1 c_1 E - D_1\frac{\partial c_1}{\partial x}) = 0 \\
&\frac{\partial c_2}{\partial t}+\frac{\partial}{\partial x}(z_2\mu_2 c_2 E - D_2\frac{\partial c_2}{\partial x}) = 0 \\
&\frac{\partial c_3}{\partial t}+\frac{\partial}{\partial x}(z_3\mu_3 c_3 E - D_3\frac{\partial c_3}{\partial x}) = 0 .
\end{aligned} \tag{2.50}$$

The current density in general has both migration and diffusion components, and may be expressed as [51]

$$J = -F\left(\sum_{j=1}^{j=3} c_j\mu_j z_j \frac{\partial V}{\partial x} + D_j\frac{\partial c_j}{\partial x}\right). \tag{2.51}$$

A solution of the form

$$c = f(x - v_b t)$$

$$\partial c / \partial t = -v_b f'(x - v_b t) = -v_b \partial c / \partial x \tag{2.52}$$

Upon integration of the conservation laws and the characteristic equation

$$\frac{\partial c_j}{\partial t} = \frac{\partial}{\partial x}(z_j \mu_j c_j \frac{\partial V}{\partial x} + D_j \frac{\partial c_j}{\partial x})$$

$$-v_b \frac{\partial c_j}{\partial x} = \frac{\partial}{\partial x}(z_j \mu_j c_j \frac{\partial V}{\partial x} + D_j \frac{\partial c_j}{\partial x}) \tag{2.53}$$

$$v_b \frac{\partial c_j}{\partial x} + \frac{\partial}{\partial x}(z_j \mu_j c_j \frac{\partial V}{\partial x} + D_j \frac{\partial c_j}{\partial x}) = 0$$

These equations are solved to yield:

$$v_b \left(\frac{1}{k\mu_1} - \frac{1}{k\mu_2} \right) + \frac{\partial}{\partial x} \ln(c_1 / c_2) = 0 \text{ or } v_b \left(\frac{D_2 - D_1}{D_1 D_2} \right) + \frac{\partial}{\partial x} \ln(c_1 / c_2) = 0 . \tag{2.54}$$

The width of the boundary is defined as the distance between points where the ratio (c_1 / c_2) varies from (e^2) to $(1/e^2)$. From the definition, the width is thus

$$\frac{4RT}{Fv_B} \frac{\mu_2 \mu_1}{\mu_2 - \mu_1} \tag{2.55}$$

$$\frac{4}{v_B} \frac{D_2 D_1}{D_2 - D_1} \tag{2.56}$$

Thus, the width of the boundary is set by the balance between the applied electric field (or boundary speed) and diffusion. Details of this derivation are provided in Appendix 99.

Stability of Moving Boundary with Fast Ions Ahead of the Slow Ions

The stability of this boundary is due to the mobility of the leading ions being greater than the trailing ions ($\mu_2 > \mu_1$). The solution of the steady-state shape of the boundary expressed in terms of the concentrations of the electrolytes is obtained from (2.54):

$$c_1 / c_2 = K \exp\left(-\frac{v_b x}{k} \frac{\mu_2 - \mu_1}{\mu_2 \mu_1} \right). \tag{2.57}$$

As $x \to \infty$, $c_1 / c_2 \to 0$, and as $x \to -\infty$ $c_1 / c_2 \to \infty$. The steady state solution predicts that c_1 has a greater value in the left and c_2 is the dominant component on the right. This configuration is similar to the initial condition of the faster ion being ahead of the slower ion, and so the shape of the boundary is maintained.

Stability of Moving Boundary with Slow Ions Ahead of the Fast Ions

If the leading ion is slower than the trailing ion, s_2 is still the leading ion and s_1 is the trailing ion, but $\mu_2 < \mu_1$, the steady state boundary shape is predicted, again using (2.57). As $x \rightarrow \infty$, $c_1 / c_2 \rightarrow \infty$, and as $x \rightarrow -\infty$, $c_1 / c_2 \rightarrow 0$. The steady state solution predicts that c_1 has a greater value on the right and c_2 is the dominant component on the left. This steady state configuration is the reverse of the initial condition. The faster ion being behind the slower ion makes the boundary unstable. One way to conceptualize this is to realize that ions of both kinds are present in the boundary. At any given position, the electric field experienced by the ions is the same. Therefore, the faster ions get ahead of the slower ions. Since the faster ions were initially behind the boundary, it results in a spreading of the boundary. To summarize, the boundary with the slower ion ahead of the faster ion is not able to maintain its sharpness. In fact, it will undergo spreading.

Combination of Stable and Unstable Boundaries

In the case of a region B of fast ions sandwiched between two regions A of slow co-ions, all with one common counter-ion, the system now consists of two initial boundaries. Assume that the concentration in A is c_A and the concentration in B is c_B. Let the leading boundary be b_2 and the trailing boundary be b_1, as shown in Figure 6.

On the application of an electric field, the two boundaries respond differently. The leading boundary b_2, which is ahead, is an unstable boundary, and it spreads over time. The boundary b_1 which is behind is a stable boundary and it moves ahead as predicted in the previous section. As a result, new regions are formed (Figure 7). A region C is formed in the wake of the stable boundary b_1; a region D is at the wake of the leading boundary; and a region E which is the same as the spreading boundary b_2.

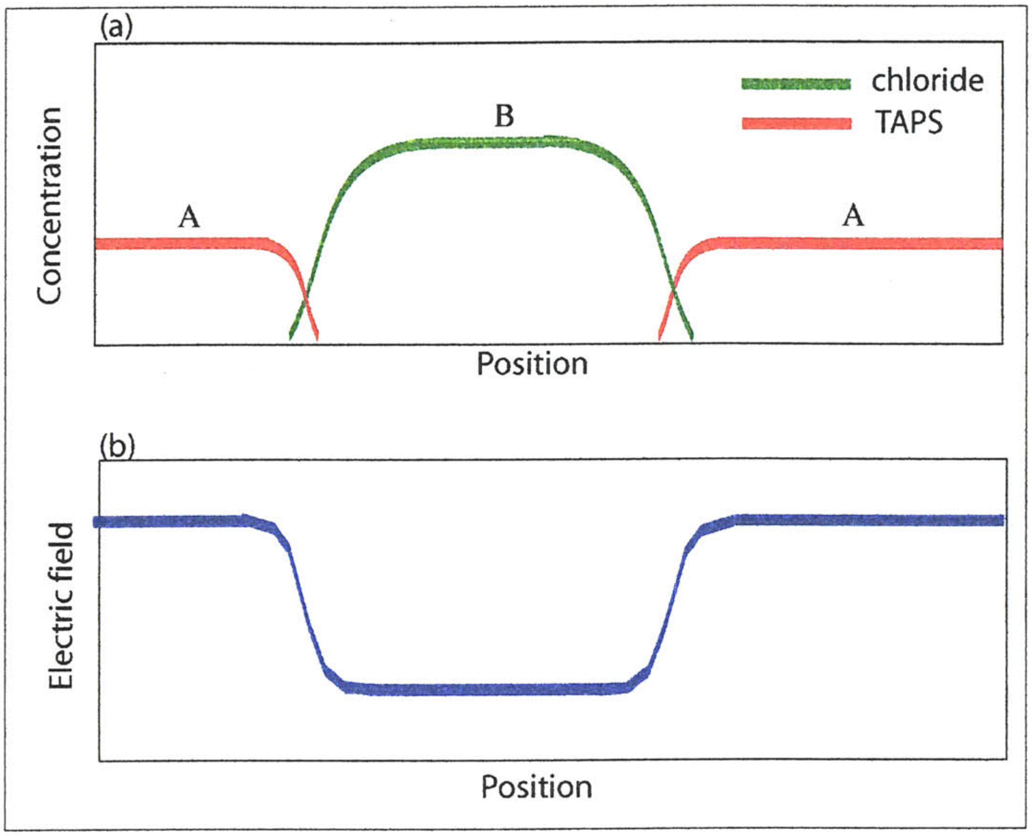

Figure 6. a. The initial concentration of TAPS and chloride co-ions. b. The initial electric field intensity.
Assuming quasi charge neutrality, the concentration of TRIS ions is the same of TAPS and chloride.

The concentrations of some of these regions may be predicted as follows. The concentration c_A and c_B are as given. In region C at the wake of the stable boundary b_1, the concentration is - $c_C = c_B \frac{\mu_1}{(\mu_1 + \mu_3)} \frac{(\mu_2 + \mu_3)}{\mu_2}$. The region between B and C has a stationary boundary with concentrations c_A and c_C across it. The concentration in region D is $c_D = c_A \frac{\mu_2}{(\mu_2 + \mu_3)} \frac{(\mu_1 + \mu_3)}{\mu_1}$. In the spreading boundary, the concentration changes from c_D to c_E. The speed at which this boundary spreads is $v_{spread} = \mu_2 E_A$. The conductivities in the different regions are:

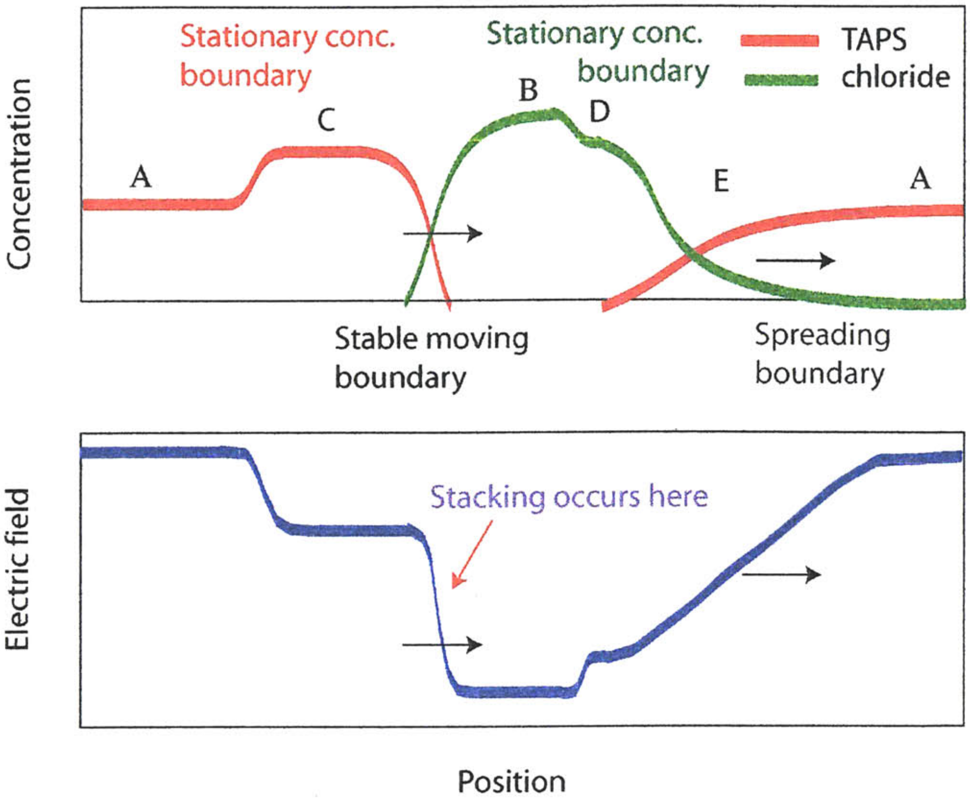

Figure 7. Evolution of Stable and Unstable Boundaries

The concentration profile of the electrolyte co-ions are shown as a result of the formation of two moving boundaries, one stable and one spreading, and two stationary concentration boundaries, one of TAPS and one of chloride. b. The resulting electric field profile due to its conductivity. Note that stacking occurs at the stable boundary at the rear of the sample plug. At this moving boundary, a high electric field replaces a lower electric field.

$$\text{A: } \sigma_A = c_A F(\mu_1 + \mu_3),$$

$$\text{B: } \sigma_B = c_B F(\mu_2 + \mu_3),$$

$$\text{C: } \sigma_C = c_C F(\mu_1 + \mu_3),$$

$$\text{D: } \sigma_D = c_D F(\mu_2 + \mu_3),$$

and in region E the conductivity varies from $\sigma_D = c_D F(\mu_2 + \mu_3)$ to $\sigma_A = c_A F(\mu_1 + \mu_3)$.

It is reasonable to assume the current density in the channel is invariant. Let it be J. The electric field in the region A is $E_A = J / \sigma_A$ or $E_A = \dfrac{J}{c_A F(\mu_1 + \mu_3)}$. Assume that the region A is much longer than the others. Then, assume that the electric field E in region A is the applied voltage per unit length. So given V and the length, we know E_A. Expressing the other electric field intensities:

$$E_B = E_A \frac{c_A(\mu_1 + \mu_3)}{c_B(\mu_2 + \mu_3)},$$

$$E_C = E_A \frac{c_A}{c_C}, \text{ and } E_D = E_A \frac{c_A(\mu_1 + \mu_3)}{c_D(\mu_2 + \mu_3)}.$$

$$\frac{E_C}{E_B} = \frac{c_B}{c_C} \frac{(\mu_2 + \mu_3)}{(\mu_1 + \mu_3)}$$

Since $\mu_2 > \mu_1$ this shows that the electric field is very high in region C and much lower in region B. This is the reason for a strong electric field gradient to exist in the moving boundary b_3.

5. Application to Sample Stacking in DNA Sequencing

The effect of the moving electric field boundary on the motion of the DNA sample causes sample stacking. Across the steady moving boundary, the electric field changes from from $E_C = E_A \frac{c_A}{c_C}$ to $E_B = E_A \frac{c_A(\mu_1 + \mu_3)}{c_B(\mu_2 + \mu_3)}$. The ratio of the electric fields is $\frac{E_C}{E_B} = \frac{c_B}{c_C} \frac{(\mu_2 + \mu_3)}{(\mu_1 + \mu_3)}$, Since $\frac{c_B}{c_C} = \frac{\mu_2}{(\mu_2 + \mu_3)} \frac{(\mu_1 + \mu_3)}{\mu_1}$, $\frac{E_C}{E_B} = \frac{\mu_2}{\mu_1}$. The speed of motion of this boundary is $v_{b3} = \mu_1 E_C = \mu_2 E_B$.

A sample particle s_X with mobility μ_X present in the region B at initial time will move at the speed $v = \mu_X E_B$. If the mobility of s_X is less than the mobility of the ion s_2, then the particle s_X will not move as fast as s_2 ions because they experience the same electric field. As a result, the s_X ions will fall relatively behind, and eventually come in contact with the moving boundary at the trailing edge of the region B.

Once the sample particle s_X crosses the boundary, it falls in a region with a much higher electric field. If the particle has a mobility higher than the species s_1, it will move ahead relative to the species s_1 and approach the boundary. Such particles with $\mu_1 < \mu_X < \mu_2$ will tend to accumulate in the interface of the two regions C and B. This is a case which can show very high stacking and is limited by diffusion.

If the particle of the sample s_X has a mobility lower than the mobility of the species s_1, $\mu_X < \mu_1 < \mu_2$, then the sample will fall relatively behind the moving boundary. In this case, the sample will still undergo stacking, though not as dramatically as in the previous case. The amount of stacking achieved can be predicted by

$$\frac{c_{X,C}}{c_{X,B}} = \frac{v_b - v_{X,B}}{v_b - v_{X,C}}$$

or

$$\frac{c_{X,C}}{c_{X,B}} = \frac{\mu_2 E_B - \mu_X E_B}{\mu_1 E_C - \mu_X E_C} = \frac{E_B}{E_C} \frac{\mu_2 - \mu_X}{\mu_1 - \mu_X} \tag{2.58}$$

or

$$\frac{c_{X,C}}{c_{X,B}} = \frac{\mu_1}{\mu_2} \left(\frac{\mu_2 - \mu_X}{\mu_1 - \mu_X} \right)$$

We can also use the concept of characteristics to understand this form stacking, as shown in a later section.

6. Riemann Approach

In the problem of moving boundaries, a single boundary of two different species on either side results in a moving boundary and a stationary boundary. The moving boundary can be of a stable form or can undergo spreading with time, depending on whether the leading ion is the faster or slower ion. Why should two waves emerge from one discontinuity? The answer to this question can be obtained by formulating this phenomenon as a Riemann problem.

In the Riemann problem the domain is divided into two parts by an initial discontinuity. The governing equations are of the form:

$$\frac{\partial \bar{u}}{\partial t} + A \frac{\partial \bar{u}}{\partial x} = 0, \tag{2.59}$$

where A is a constant n x n matrix and the initial conditions are of the form

$$u(x,0)=\begin{cases}\vec{u}_L & x<0\\ \vec{u}_R & x>0\end{cases}.$$

If A is diagonalizable, $A=Q\Lambda Q^{-1}$ where Q^{-1} is a constant ***n*** x ***n*** matrix whose rows I_i are left characteristic vectors of A. Λ is a constant ***n*** x ***n*** diagonal matrix whose diagonal elements λ_i are characteristic values of A. Consider the following change of variables $\vec{v}=Q^{-1}\vec{u}$ which results in

$$\frac{\partial\vec{v}}{\partial t}+\Lambda\frac{\partial(\vec{v})}{\partial x}=0, \tag{2.60}$$

where

$$\vec{v}(x,0)=\begin{cases}\vec{v}_L=Q\vec{u}_L & x<0\\ \vec{v}_R=Q\vec{u}_R & x>0\end{cases}.$$

The characteristics are indicated by

$$\frac{\partial\vec{v}_i}{\partial t}+\lambda_i\frac{\partial(\vec{v}_i)}{\partial x}=0, \tag{2.61}$$

where

$$\vec{v}_i(x,0)=\begin{cases}\vec{v}_{Li}=I_i\vec{u}_L & x<0\\ \vec{v}_{Ri}=I_i\vec{u}_R & x>0\end{cases}.$$

Since λ_i is constant, Equation (2.61) is just the linear advection equation. The Riemann problem for a linear system of *n* equations is equivalent to *n* Riemann problems for linear advection equations.

As illustrated in Figure 8, the solution to the characteristic form of Equation (2.61) is

$$\vec{v}_i(x,t)=\vec{v}_i(x/t)=\begin{cases}(\vec{v}_{L1}\ \ \vec{v}_{L2})^T & (x/t)>\lambda_2\\ (\vec{v}_{R1}\ \ \vec{v}_{L2})^T & \lambda_1<(x/t)<\lambda_2\\ (\vec{v}_{R1}\ \ \vec{v}_{R2})^T & (x/t)<\lambda_1\end{cases} \tag{2.62}$$

In general, *n* conservation laws yield n characteristic values/directions or *n* possible modes. Applying this theory to a Riemann problem in electrophoresis, yields three conservation laws:

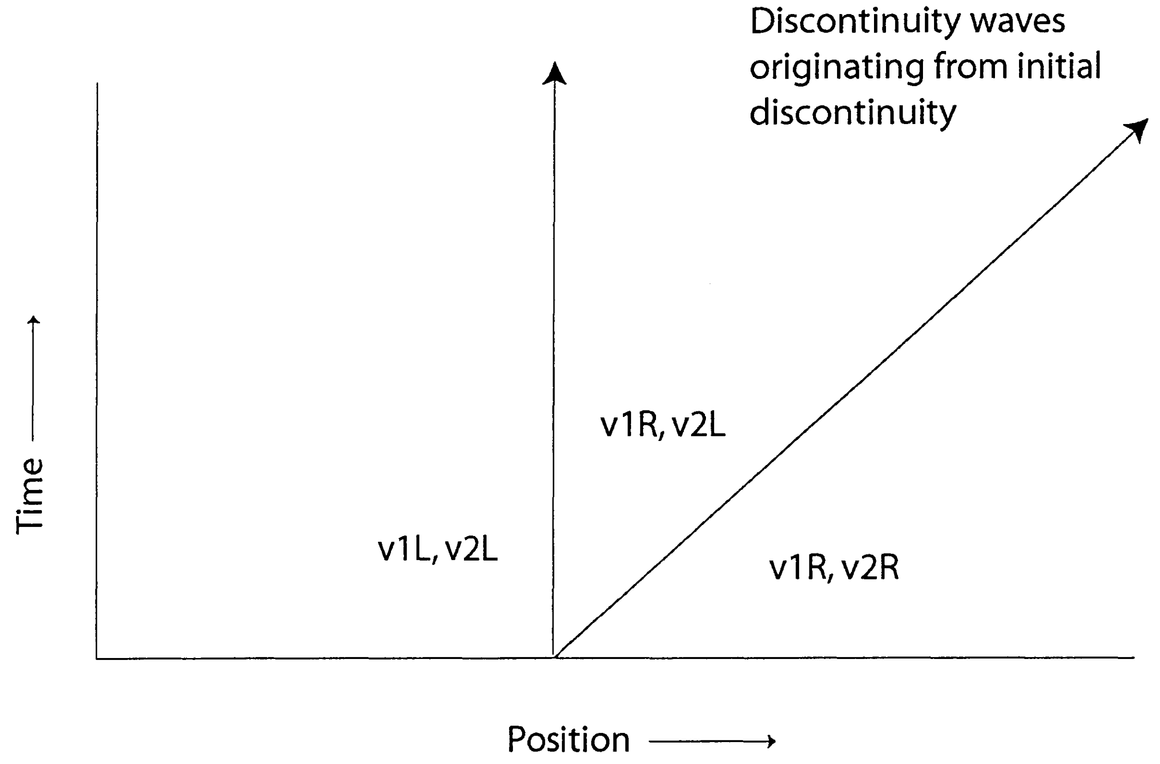

Figure 8. Solution of Riemann Problem Described by Two Conservation Laws

Initially the two regions have values at the left and right have different values of the variables v_1 and v_2. The emergence of two waves divides the domain into three regions.

$$\frac{\partial c_1}{\partial t}+\frac{\partial}{\partial x}(-\mu_1 c_1 E - D_1 \frac{\partial c_1}{\partial x}) = 0\,, \tag{2.63}$$

$$\frac{\partial c_2}{\partial t}+\frac{\partial}{\partial x}(-\mu_2 c_2 E - D_2 \frac{\partial c_2}{\partial x}) = 0\,, \text{ and} \tag{2.64}$$

$$\frac{\partial c_3}{\partial t}+\frac{\partial}{\partial x}(\mu_3 c_3 E - D_3 \frac{\partial c_3}{\partial x}) = 0\,. \tag{2.65}$$

Charge neutrality yields

$$c_1 + c_2 = c_3\,, \tag{2.66}$$

which is true everywhere, except at the boundaries because $\nabla \cdot (\sigma \bar{E}) = 0$, valid everywhere except at interfaces. This constraint results in two net conservation laws which results in two characteristics. The characteristics have already been computed in the previous section on moving boundaries.

7. The Concept of Characteristics

Consider a conservation law or advective transport equation of the form $\frac{\partial c}{\partial t}+v\frac{\partial c}{\partial x}=0$.

Expressing the total derivative as a sum of partial derivatives, yields $\frac{dc}{dt}=\frac{\partial c}{\partial t}+\frac{\partial c}{\partial x}\frac{dx}{dt}=0$.

Comparing the previous two equations $\frac{dc}{dt}=\frac{\partial c}{\partial t}+\frac{\partial c}{\partial x}\frac{dx}{dt}=\frac{\partial c}{\partial t}+v\frac{\partial c}{\partial x}=0$ yields $v=\frac{dx}{dt}$ which further yields $dx=v.dt$ or $x=vt+const$ or $x-vt=const$.

The line $x-vt=const$ represents a characteristic, and given the initial value of concentration (c_0), the concentration at any other time can be predicted by the use of such characteristics. One way of looking at this is that the variables have been changed from space and time to a single variable that depends on both space and time. This is also known as a similarity variable or a similarity solution.

8. Sample Stacking from a Characteristics Perspective

The concept of characteristics is helpful in understand sample stacking. There are two cases of stacking. In the first case, the sample is slower than the buffer. Its characteristics are as shown in Figure 9. Here, once the sample falls behind the moving boundary, it moves slower than the buffer. Since its speed is still increased due to the higher electric field in this region, it undergoes stacking.

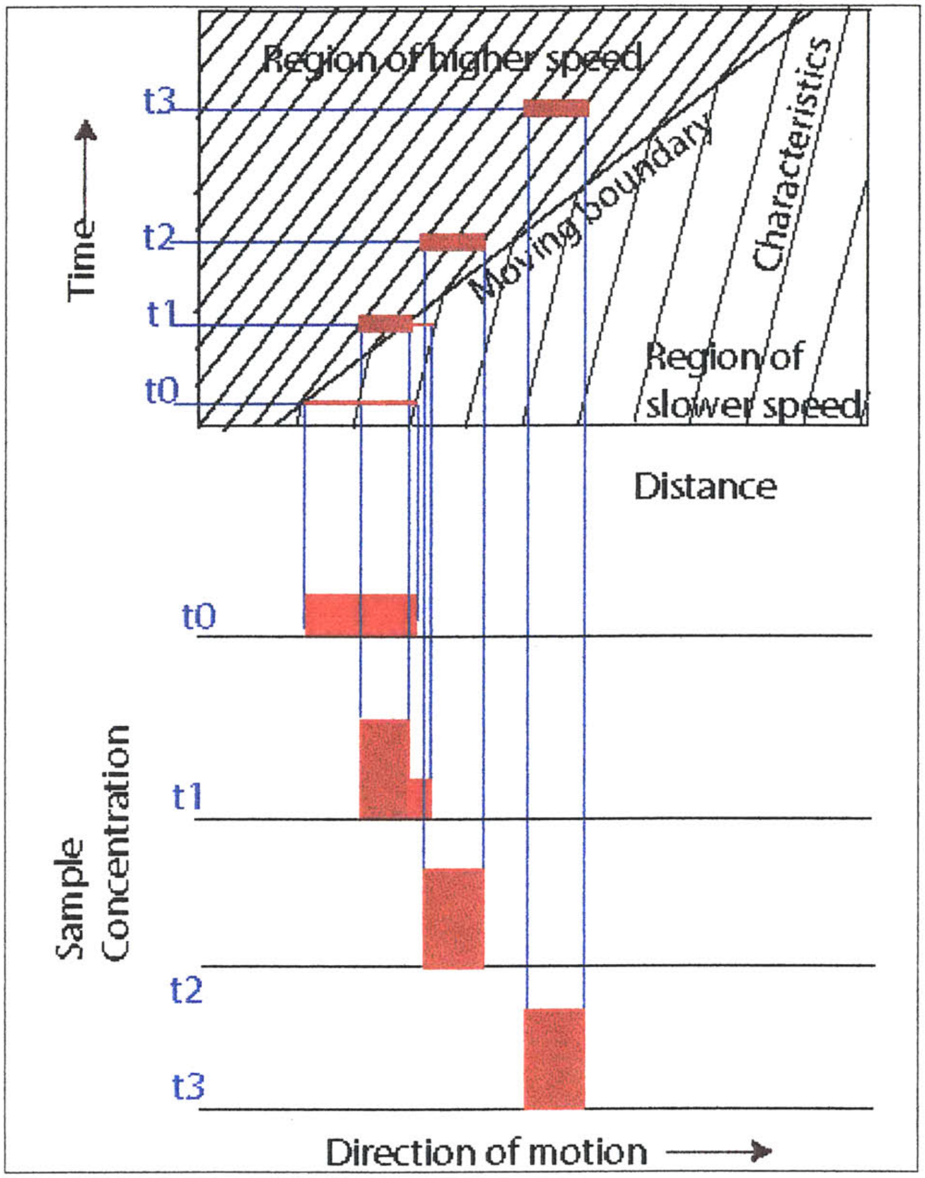

Figure 9. Sample Stacking with Sample Mobility Less Than Buffer Mobility

Characteristics describe the motion of particles in a region of higher speed and a region of lower speed. The boundary between the two regions moves at a speed defined by the characteristic of the boundary. The convergence of characteristics is a "shock." In this case, the sample mobility is less than the mobility of the buffer co-ion. A rise in concentration is seen at the region of the boundary. The rise in concentration depends on the ratio of sample mobility to buffer co-ion mobility.

In the next case, the sample moves faster than the buffer (Figure 10). When the rear part of the sample plug comes in contact with the boundary, it enters the region of high electric field behind the boundary. As a result, the sample speeds up and having a mobility higher than the buffer, it tends to go relatively ahead. Thus, the sample tends to go towards the boundary from either side. The sample accumulates in this boundary resulting in high stacking. In this case the result is the convergence of characteristics. This is an analog of a 'shock' in fluid mechanics.

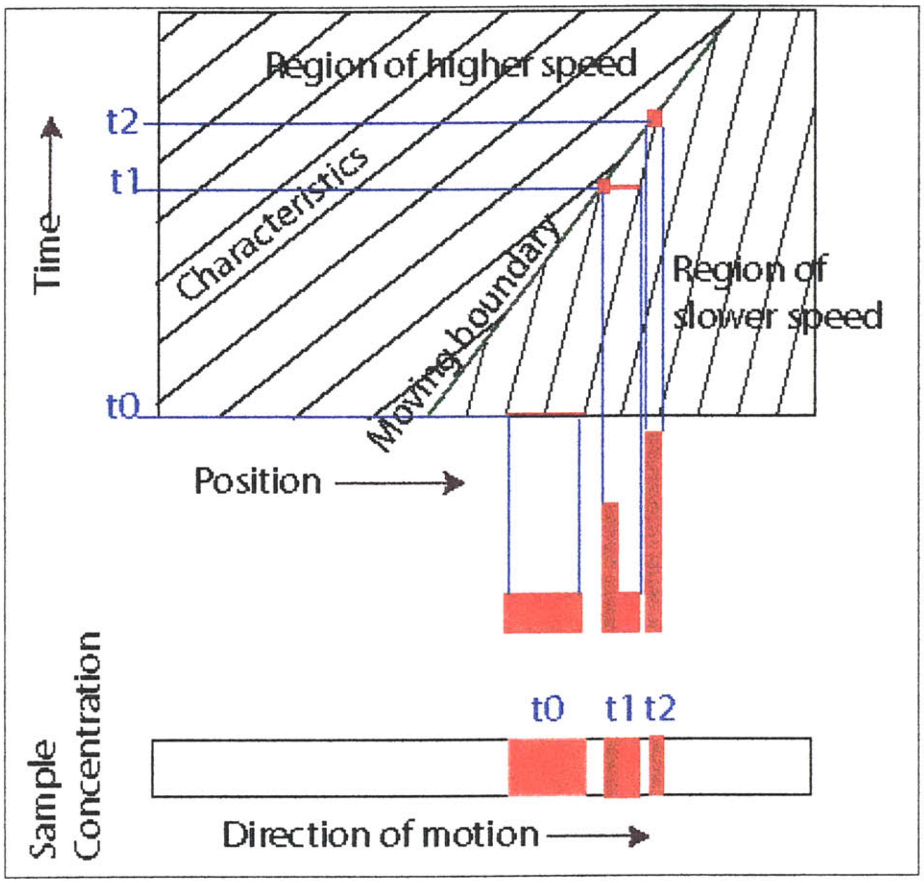

Figure 10. Sample Stacking with Sample Mobility More Than Buffer Mobility

Characteristics describe the motion of particles in a region of higher speed and a region of lower speed. The boundary between the two regions moves at a speed defined by the characteristic of the boundary. The convergence of characteristics is a "shock." In this case, the sample mobility is greater than the mobility of the buffer co-ion. A sharp rise in concentration is seen at the region of the boundary.

9. Modeling Different Types of Electrophoresis

The different forms of electrophoresis can all be modeled by a similar set of governing laws. What makes each type of electrophoresis different from a modeling perspective? One key difference is that ZE, MBE, and ITP have Dirichlet boundary conditions whereas IEF has Neumann type boundary conditions. In Dirichlet boundary conditions, the value of the independent variable is specified whereas in Neumann boundary conditions, its gradient is specified. Mixed boundary conditions have a linear combination of the independent variable and the gradient.

From the perspective of electric field the following observations may be made. In ZE, the electric field is reasonably constant along the length of the column. In MBE and ITP, the electric field shows sharp discontinuities at the boundaries. In IEF, the electric field shows variation across the column.

10. Types of Stacking

Field-Amplified Stacking

In field-amplified stacking, there is a concentration boundary of the buffer and the sample moves from a low concentration buffer to a high concentration buffer. As a result, the sample slows down as it enters the low field and low speed region from the high field region. Consequently, the concentration of the sample increases.

Isotachophoresis-Assisted Stacking

Also called transient isotachophoresis stacking, this form of stacking uses two distinct buffer systems between the sample to initiate the process of isotachophoresis. As a result, the sample separates into very narrow bands of high concentration. Once separation into bands occur, the buffer behind the sample region is changed to bring about zone electrophoresis. Once this happens, the narrow sample bands proceed to migrate down the separation channel and further separate into the constituents. The effect of stacking is to amplify the sample concentration, increasing its efficiency of separation and detection.

11. Review of Mathematical Modeling of Electrophoresis

Extensive work has been done on modeling of electrophoresis. Bier et al. [40] reported the first unified treatment of all forms of electrophoresis. Electrophoresis can be modeled by conservation laws for charged species under transport due to electro-migration and diffusion. Reaction or generation of the species may be considered where chemical equilibrium is significant. Dissociation of water must be accounted for in cases of very high or very low pH. Charge neutrality and charge conservation are assumed for all electrophoresis modeling. Charge conservation is a universal law, as shown from Maxwell's laws. Charge neutrality is assumed because charge relaxation times are much shorter than the time scale of electrophoresis and the electric fields are too small to maintain charge separation. Fife, Palusinsky and Su [47] have justified these assumptions in detail. The governing equations with the appropriate initial conditions and boundary conditions are solved numerically to obtain dynamic simulations of the electrophoretic process.

Mathematical models and numerical approaches for electrophoresis have been extensively studied. Saville et al. [52] has presented a general mathematical model for electrophoresis. Mosher et al. [53] developed a dynamic numerical model for isotachophoresis of proteins. Dose and Guichon [54] have reported a high-resolution modeling scheme of capillary zone electrophoresis and isotachophoresis. Martens et al. [55] modeled the transient phase of capillary electrophoresis for isotachophoresis and compared the results with earlier methods. Su [56] has shown the analysis and computational results of interface dynamics in isotachophoresis. Ermakov et al. [57] has focused on the simulation of capillary zone electrophoresis. Andreev and Lisin [58] have modeled capillary electrophoresis with electro-osmotic flow. Chien [59] has developed a model for field amplified stacking. Schwer et al. [60] developed a numerical simulation to show on-column sample pre-concentration in capillary zone electrophoresis in discontinuous buffer systems.

Moving salt boundaries had been studied by Tiselius [23]. Longsworth [51] demonstrated and modeled the shape of the steady, self-sharpening moving boundaries. Moore [61] has shown a more general analysis of the self-sharpening nature of these boundaries, which is based on the mathematical theory of quasi-linear equations developed by Gel'fand [62]. Although a treatment of the transient dynamics of the evolution of isotachophoretic boundaries is quite involved, the analysis of a steady state moving boundary is reasonably simple and example of this analysis has been provided by Mosher [63].

12. Model for Sample Stacking in Microcapillary DNA Electrophoresis

Experimental data of DNA stacking described in Chapter 4 and as seen under video microscopy has revealed a sample concentration peak moving from the trailing edge of the sample plug to the leading part of the sample. To understand and model the dynamics of stacking requires a combination of (a) the process of sample introduction into the microcapillary and (b) the dynamics of moving boundaries between two electrolytes. The microcapillary device geometry consists of a sample injector at one end of the channel as shown in Figure 2.

Sample Introduction

The sample is electrokinetically introduced from the sample reservoir. The cathode is immersed into the sample, and the anode is at the waste reservoir filled with the buffer. In the DNA sample, the major anions are chloride and the minor anions are DNA ions. An electric field is applied between the injector terminals causing the sample anions ($DNA^- \sim 10^{-10}$ M and Cl^-

$\sim 10^{-3}$ M) to enter from the anode reservoir and buffer cations ($TRIS^+$) to enter from the anode reservoir. The progress of sample loading is shown in Figure 11. After sample loading, the sample cations occupy the inlet arm, the injector column, and the outlet arm of the injector. The anions are primarily $TRIS^+$. Along the main separation channel of the micro-capillary, the sample plug is contiguous with the running buffer on either side. The buffer is 1X Tris⁻TAPS⁻EDTA (TTE). TAPS is N-tris(Hydroxymethyl)methyl-3-aminopropanesulfonic acid and TRIS is Tris(hydroxymethyl)aminomethane. Since the electric field remains nearly zero in the region outside the injector, it undergoes little electrokinetic activity.

Sample Injection

A potential is applied across the length of the injector causing the sample plug to electrokinetically move into the separation channel as shown in Figure 12. The DNA sample, immersed in a plug rich in chloride ions, undergoes stacking during the injection stage of the process. In previous studies, the role of sample stacking had been given cursory consideration or had not been understood. The dynamics of sample stacking is explained in this thesis.

Along the center line of the injector and separation chamber, the concentrations of the buffer and sample ions are evaluated. This concentration profile of buffer is non-zero before and ahead of the sample plug. The chloride concentration in the sample plug is of the order of the buffer concentration on either side of the sample plug. The concentrations of buffer ions are 10 mM $TAPS^-$ and 10 mM $TRIS^+$. The chloride ion concentration is estimated at 23 mM. These estimates are based on the conductivity of the channel and verified using their dissociation constant.

The effect of the applied electric potential across the separation channel is analyzed. The analysis is similar to that presented in Section 5. In the electrophoresis of DNA fragments for sequencing, the conductivity of the sample in the separation channel is dominated by electrolyte (Cl^-) ions. The buffer and chloride ion concentrations are of the order of 10^{-3} M, and the DNA concentration is approximately 10^{-10} M. The $Tris^+$, $TAPS^-$, and Cl^- ions form the primary charge

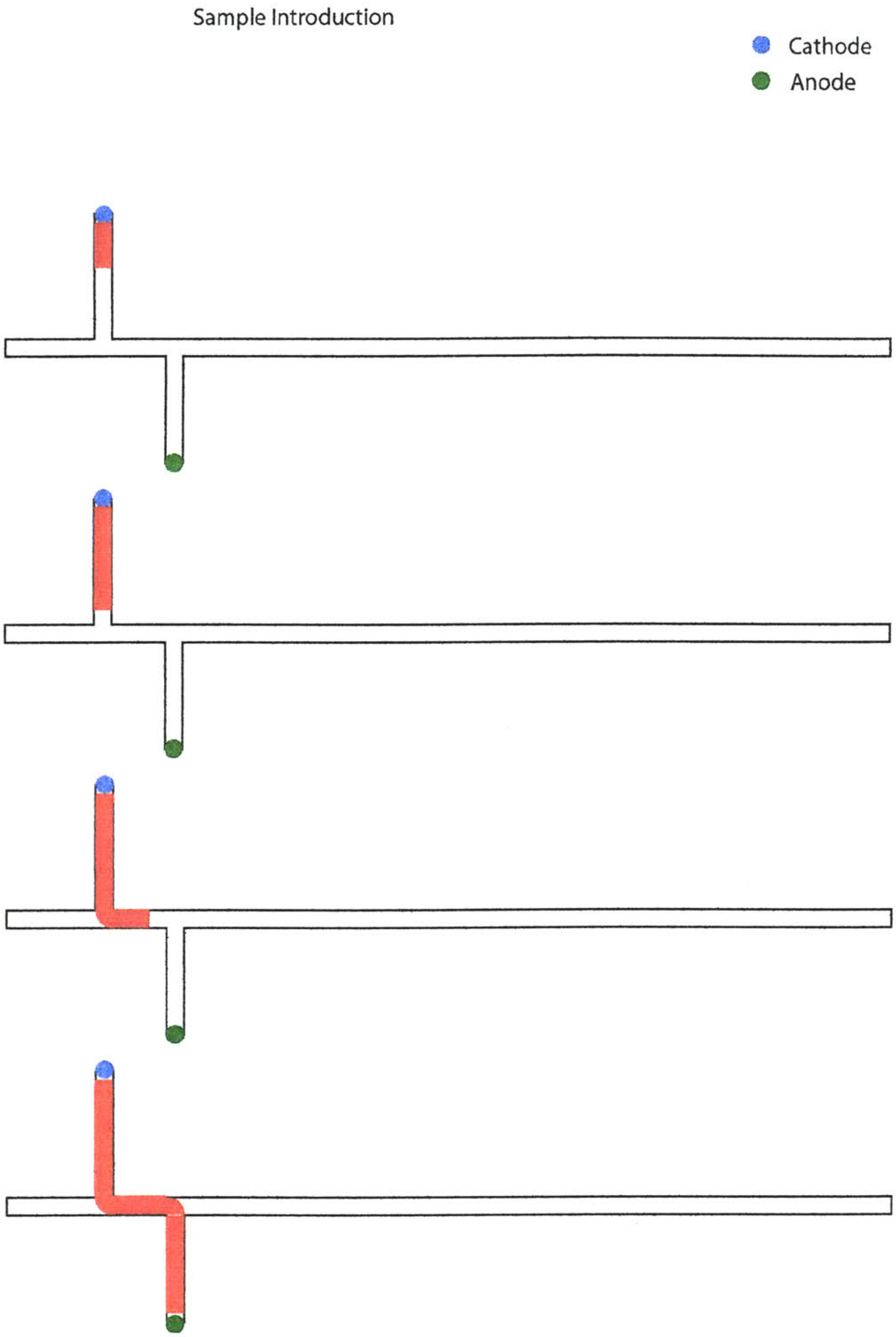

Figure 11. Sample Introduction in a Microcapillary

The DNA sample is introduced from the sample reservoir which also has the cathode immersed into the sample. The sample anions enter the microcapillary as indicated by the red shaded region. They occupy the injector displacing the buffer anion TAPS over time.

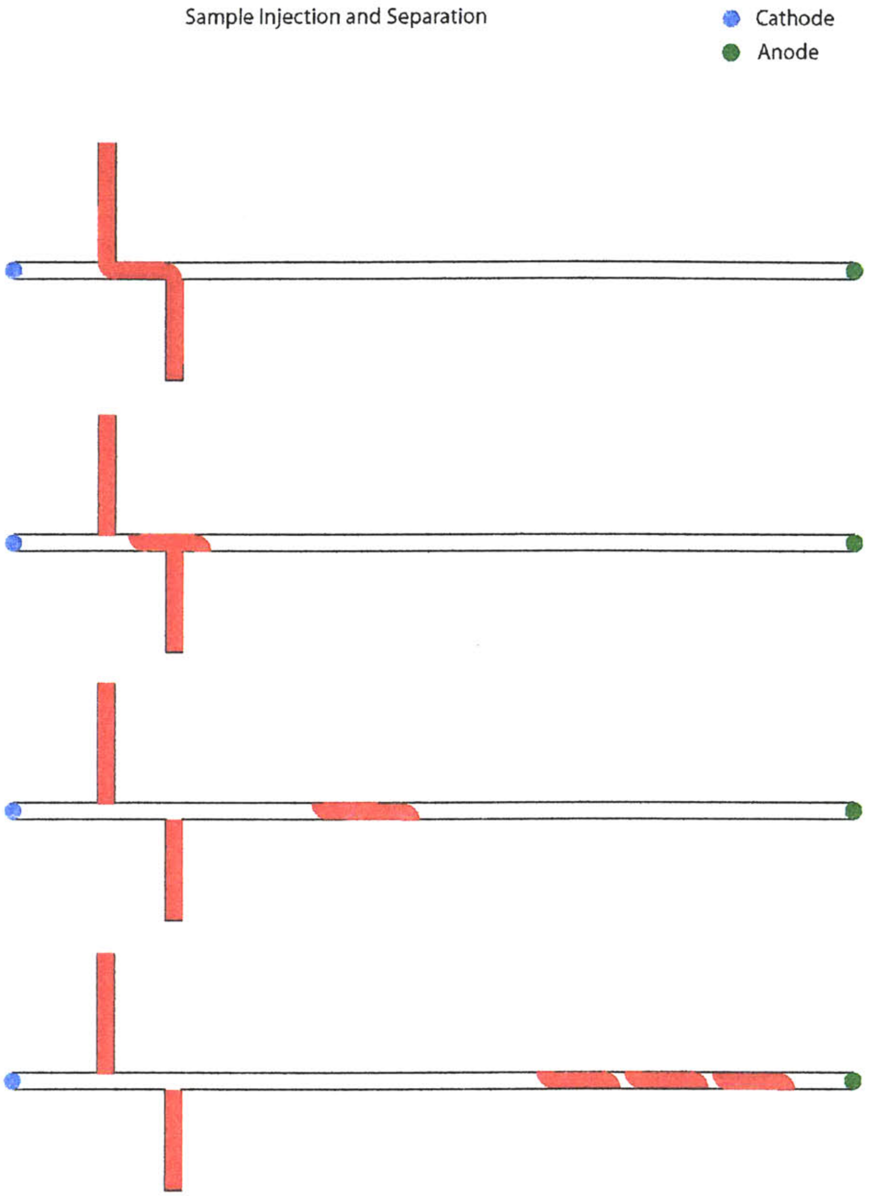

Figure 12. Sample Injection in a Microcapillary Electrophoresis Device

The sample is injected from the injector into the separation chamber as a voltage is applied across the separation chamber. Stacking occurs during sample injection. After stacking, the sample undergoes zone electrophoresis, in which it separates due to the difference in mobility and diffuses over time.

carriers for electric current conduction. The DNA sample, which contributes negligibly to the conductivity, undergoes motion due to the electric field.

The previous section demonstrated that the major component (chloride) in the sample forms two boundaries with the buffer - a leading boundary and a trailing boundary. When an external electric field is applied along the separation capillary, the two boundaries respond in different ways. The mobility of chloride is approximately four times higher than the mobility of TAPS. The trailing boundary turns out to be a stable moving boundary because the faster ion (chloride) is ahead of the boundary, followed by the slower ion (TAPS$^-$). The leading boundary is unstable because the slower ion (TAPS$^-$) is ahead of the boundary and the faster ion is behind the boundary. Consequently, this boundary spreads out over time with the passage of current.

The stable moving boundary causes a region of sharp electric field discontinuity to move along with it. This boundary is created at the trailing edge of the injector and moves along, creating a region of higher electric behind the moving boundary and a region of lower electric field ahead of the boundary. The electric field discontinuity at the leading boundary spreads out over time. Sample stacking takes place at the sharp discontinuity of the electric field which imposes a velocity field on the minor components causing the sample ions to stack.

Typical initial concentrations are

$$c(x,0+) = \begin{cases} c_{TAPS} = 10\ mM,\ c_{Cl} = 0,\ c_{TRIS} = 10\ mM & A \\ c_{TAPS} = 0,\ c_{Cl} = 22.5\ mM,\ c_{TRIS} = 22.5\ mM & B \end{cases}.$$

The mobility values are

$$\mu_{TAPS} = 21\times10^{-9} m^2/sV\ ,\ \mu_{Cl} = 79\times10^{-9} m^2/sV\ ,\ \mu_{TRIS} = 29\times10^{-9} m^2/sV\ .$$

With the application of an electric potential across the separation column, the electric field profile is

$$E(x,0+) = \begin{cases} 100V/cm & A \\ 20.6V/cm & B \end{cases}.$$

For an applied voltage of 1200 along a 12 cm device, the applied average electric field is 100 V/cm. Since region A has the lowest conductivity and the dominant length, the electric field in region A is 100 V/cm. The electric field in B is computed by the common current in all the regions and its conductivity.

At the application of an electric field and any time t, a new region C is created such that the concentrations are

$$c(x,0+) = \begin{cases} c_{TAPS} = 10\ mM,\ c_{Cl} = 0,\ c_{TRIS} = 10\ mM & A \\ c_{TAPS} = 12.9 mM,\ c_{Cl} = 0,\ c_{TRIS} = 12.9\ mM & \mathrm{C} \\ c_{TAPS} = 0,\ c_{Cl} = 22.5\ mM,\ c_{TRIS} = 22.5\ mM & B \end{cases}$$

and electric field is

$$E(x,0+)=\begin{cases}100\ V/cm & A\\ 77.5\ V/cm & C\,.\\ 20.6\ V/cm & B\end{cases}$$

The speed of the boundary is $v_b=\mu_2 E_B = 79\times10^{-9}\times20.6\times100$ m/s or $v_b=162.7\ \mu m/s$. The width of the moving boundary is estimated [63] by:

$$w=\frac{4RT}{Fv_b}\frac{\mu_2\mu_1}{\mu_2-\mu_1}, \tag{2.67}$$

$$w=\frac{4\times8.314\times323}{10^5\times162.7\times10^{-6}}\frac{79\times21\times10^{-9}}{79-21}=189\mu m.$$

To predict sample stacking, two cases are considered separately. The sample species is denoted as s_X. (a) In the first regime, the sample is slower than the buffer, or $\mu_X<\mu_{TAPS}$. The sample stacking ratio is

$$SR=\frac{\mu_{TAPS}}{\mu_{Cl}}\frac{\mu_{Cl}-\mu_X}{\mu_{Cl}\mu_X}. \tag{2.68}$$

(b) In the second regime, the sample is faster than the buffer, or $\mu_X<\mu_{Cl}$. Sample stacking occurs due to the entrapment of the sample in the boundary. The stacking ratio thus depends on the width of the boundary and the length of sample plug swept by the boundary:

$$SR=\frac{l_{swept}}{w_{boundary}}. \tag{2.69}$$

In this mode, the stacking ratio increases as the injector length increases. The maximum stacking occurs when the complete plug is swept by the injector. When the width of the moving boundary is less, the sample is constrained in a smaller area and as a result its concentration increases. The width of the moving boundary is evaluated as

$$w=\frac{4RT}{Fv_b}\frac{\mu_{Cl}\mu_{TAPS}}{\mu_{Cl}-\mu_{TAPS}}. \tag{2.70}$$

The width of the boundary depends upon the speed of the boundary, the mobility values of chloride and the buffer co-ion TAPS$^-$, the difference between the mobility values, and temperature. An increase in the translation speed of the boundary reduces its width. The width decreases with an increase in the difference between the leading and trailing co-ions at the boundary and increases as the product of the two mobility values.

The speed of the boundary is

$$v_b = \mu_{Cl} E_B . \tag{2.71}$$

The speed of the boundary depends upon the applied electric field. From Section 5, E_B, the electric field in region B may be expressed as

$$E_B = E_A \frac{c_A(\mu_{TAPS} + \mu_{TRIS})}{c_B(\mu_{Cl} + \mu_{TRIS})} . \tag{2.72}$$

Substituting the value for the electric field Equation (2.71) yields

$$v_b = \mu_{Cl} E_A \frac{c_A(\mu_{TAPS} + \mu_{TRIS})}{c_B(\mu_{Cl} + \mu_{TRIS})} , \tag{2.73}$$

and the boundary width, expressed in known quantities, becomes

$$w = \frac{1}{E_A} \frac{4RT}{F} \frac{c_B}{c_A} \frac{(\mu_{TAPS})}{(\mu_{Cl} - \mu_{TAPS})} \frac{(\mu_{Cl} + \mu_{TRIS})}{(\mu_{TAPS} + \mu_{TRIS})} . \tag{2.74}$$

This shows that the applied field, the concentrations of the buffer and stacking ions, the temperature, and the mobility values of the buffer ions and stacking ion play a role in determining the width of the boundary. The effects of these parameters can be explored. The effect of an increased electric field shows a decrease in width and therefore higher stacking for the regime of the sample faster than the buffer co-ion.

The amount of an increased electric field that will still yield a sharper boundary is limited by thermal effects. However, there are limits to process enhancements by increases in the applied injection voltage. Higher applied voltages result in higher currents and higher heating of the channel. Since heat generation causes a non-uniform temperature distribution in the channel, it can lead to convection and a widening of the boundary. The exact nature and treatment of this aspect is not developed further in this thesis. Another consequence of the thermal effect is the following. A non-uniform temperature results in non-uniform mobility values of the DNA since DNA mobility depends on temperature. One of the goals of sample stacking is a sharpening of the initial sample plug for improved resolution of separation. Since an increased applied voltage increases the variation of sample mobility in a plug, the sample plug undergoes spreading and reduces the potential resolution of separation.

The movement of the stable boundary is isotachophoretic until it reaches the leading end of the injector. When the stable boundary reaches the initial location of the leading boundary, the concentration of TAPS$^-$ ions becomes non-zero throughout the region. At this stage, the conditions for ITP - non-intersecting concentration profiles of leading and trailing ions - are no longer satisfied, and the process transitions into zone electrophoresis. The sample electrolyte anion (Cl$^-$) plug undergoes zone electrophoresis along with the stacked DNA samples. The sample electrolyte, being faster than the sample DNA moves ahead of the sample along the separation chamber.

Two types of stacking have been described. When the sample mobility is less than the trailing ion mobility, stacking occurs because the trailing part of the sample moves faster than the leading part. In the case where the sample ion has a higher mobility than the trailing ions, the stacking is very strong and may be modeled as a shock. Although this section treats the stacking of DNA sample specifically for microfabricated capillaries, the analysis presented will still be valid as long as the sample is loaded electrokinetically such that the stacking ion displaces the buffer ion upon sample introduction and that the buffer ahead of and behind the sample has a similar co-ion as the sample.

In this thesis, the following model uses governing conservation laws or transport equations for each electrolyte species s_1, s_2 and s_3. (1 represents the TAPS$^-$ ion, 2 represents the chloride$^-$ ion, and 3 represents the TRIS$^+$ ion.) c_1, c_2, and c_3 represent the concentration of species s_1, s_2 and s_3

$$\frac{\partial c_1}{\partial t}+\frac{\partial}{\partial x}(-\mu_1 c_1 E - D_1\frac{\partial c_1}{\partial x}) = 0 \qquad (2.75)$$

$$\frac{\partial c_2}{\partial t}+\frac{\partial}{\partial x}(-\mu_2 c_2 E - D_2\frac{\partial c_2}{\partial x}) = 0 \qquad (2.76)$$

$$\frac{\partial c_3}{\partial t}+\frac{\partial}{\partial x}(\mu_3 c_3 E - D_3\frac{\partial c_3}{\partial x}) = 0 \qquad (2.77)$$

Since 1 and 2 are negatively charged anions, they have a negative sign in Equations (2.75) and (2.76).

In general, the conservation laws have reaction and generation (sink or source) terms. Such terms arise due to the chemical reaction of species or dissociation of species. In the case of DNA electrophoresis under the conditions under study, the parameter that could cause a deviation of the concentrations of the ionic species from this model is the pH, which is maintained nearly constant at 8.1-8.3. As a result, the assumption of zero reaction and generation terms is reasonably well justified.

The analytical approach for sample stacking in DNA electrophoresis using microcapillaries has been developed and predictions have been made using this model.

Chapter 3. Numerical Model and Simulation

1. *Review of Numerical Simulation Methods in Electrophoresis*

A mathematical model can describe a dynamical system with the aid of partial differential equations that capture the relevant interactions. The partial differential equations in the model for electrophoresis are a set of coupled advection diffusion equations. Additionally, these equations have reaction and generation terms that represent the reaction and dissociation of the species. The dissociation and reaction terms are defined by algebraic equations. In general, the partial differential equations governing electrophoresis do not have a closed form solution although it may be possible for very simple cases. Numerical methods are used to understand the mathematical model and enhance our capability to predict the behavior of the system. Numerical methods can help to perform numerical experiments to optimize the process. They are also useful in observing the results of all variables, some of which may not be easy to measure in reality. In the model for electrophoresis developed in this thesis, the independent variables are the concentrations of the electrolytes and sample. The model is based on theory developed in Chapter 2. The electric field distribution and the concentrations of the electrolytes are evaluated at all positions at every time step in the numerical experiment. The experimental data available has information on only the applied voltages and the DNA sample distribution. Concentration profiles of the other electrolytes are derived from theoretical principles that have been experimentally tested in other applications [50].

Two numerical approaches are commonly used –the finite difference method (FDM) and finite element method (FEM). The advantage with finite difference is that it is a simpler technique and easier to implement. On the other hand, FEM is a more complex tool that can analyze unstructured meshes, and it is possible to consider arbitrary shapes of the domain under consideration. Although commercial FEM packages are available, they are usually specialized in application. Most finite element packages are targeted towards structural analysis and fluid mechanics. General purpose software packages usually have limited capabilities. One commercial package, FEMLAB® was very useful for computation of electric field. However a moving boundary problem with the transport and coupled electric field could not be successfully implemented. Currently there is no commercially available software capable of solving the problem described in this chapter.

Finite difference methods were introduced by Courant, Friedrichs, and Lewy [64] in 1928 but were put to practical use after fifteen years with the development of computers. They are also credited with the well-known Courant-Friendrichs-Lewy stability criterion. A text by Richtmyer and Morton [65] covers the fundamentals of finite difference methods.

Mosher [63] has described the numerical modeling of electrophoresis in a text. Earlier, Bier et al. [40] had shown that the model for all types of electrophoresis had a unified foundation. All the forms of electrophoresis could be modeled with a common set of partial differential equations, the difference arising from the differences in the boundary conditions. They implemented a simple numerical scheme for the different forms of electrophoresis. Since then, significant work has been done on developing advanced numerical methods with higher accuracy and more efficient computation. Palusinski et al. [66] have shown that for ZE, MBE and ITP the rate of change of the concentrations at the domain boundaries are zero. In contrast, the boundary conditions in IEF are expressed in terms of the permeability to the various ions.

In the approach of Palusinski et al. [66], they have shown the use of an observational window that defines a movable grid. The computational algorithm advances at the migration rate of the fastest moving species, enabling a saving of computational time and memory. Such methods can be applied only to ZE, MBE, and ITP. They are not applicable to IEF because the ends of the column are fixed.

The first set of developments, from Dose and Guiochon [54], who have shown that the numerical method can be improved by using fine grids in active regions and coarser grids in inactive regions, thus taking advantage of the process physics and evolution of the field values. The application of this method was in capillary zone electrophoresis and isotachophoresis. The results compared favorably with experimental data.

The credit for raising the sophistication of numerical methods in electrophoresis modeling goes to Ermakov [67], who showed that the methods previously developed by Bier and Dose were insufficient for the current densities typically used in practical electrophoresis. It was pointed out in practice, a quantitative comparison of experimental and computed results was largely absent due to these limitations. Ermakov et al. [67] [68] [69] [57] [70] [71] developed numerical schemes based on the addition of artificial dispersion terms to the convection-diffusion equation which improved simulation results, reducing numerical oscillations and diffusion.

Martens et al. [55] reviewed the performance of different explicit and implicit schemes for 1-dimensional electrophoresis specifically for ITP. Schwer [60] conducted numerical simulations of sample preconcentration as part of a study for capillary zone electrophoresis with discontinuous buffer systems. Everaerts [72], Mosher [53] and Poppe [73] have each implemented numerical methods for isotachophoresis.

For a spatial 1-dimensional problem, the finite difference method is well suited. Once a numerical method is chosen, the spatial and temporal grid size is selected. The choice of these parameters depends on the electric field values and gradients as shown by Bier [40] and Dose et al. [54]. The physics of this problem is dominated by the hyperbolic terms. The approximation of the $\partial(cv)/\partial x$ term is the critical step. The two simplest and commonly used methods are upwind difference and central difference approximations. Upwind methods cause numerical dispersion whereas central difference methods cause numerical diffusion [55]. Ermakov [69], borrowing a concept from computational fluid dynamics , applied a method that introduces numerical dispersion to enhance the stability of the method.

Developments in other frontiers of numerical methods would later have an impact on electrophoresis modeling. One significant development was in the area of numerical methods for hyperbolic conservation laws with sharp discontinuities in the solution by Lax and Wendroff [9]. The method was designed for discontinuities confined to a narrow band of two-three mesh points. The method is found to be stable under a mild strengthening of the Courant-Friedrichs-Lewy condition. The additional terms introduce artificial viscosity into the solution. Although this method can treat shocks, it has some inherent accuracy issues, namely numerical dispersion that manifests itself in overshoots and undershoots.

Further advances in methods of solving conservation laws were made which reduced the problem of overshoots and undershoots. A well-known scheme called flux-corrected transport (FCT) by Boris and Book [10] has been particularly noteworthy. FCT falls within a class of solutions called flux limiters, which prevent the fluxes from reaching non-physical values. The method solves within it, a high order method and a low order method and uses a non-linear filter to choose the weighted form of the solution. The scheme of choice for numerical solutions with sharp gradients is the FCT method. FCT was implemented for electrophoresis by Sounart and Baygents [74] and its performance further evaluated and compared with other methods [75].

In this thesis, a forward in time and central in space (FTCS) scheme was developed for a 1-dimensional case. The advantage with FTCS is that it is a remarkably stable scheme, although its ability to handle sharp discontinuities is limited. Although it has been stated by Ermakov [68] that FTCS methods are not capable of handling high current densities, this thesis demonstrates that it is possible. Perhaps the implementation is possible because the length scales of this problem are very small compared to the process modeled earlier. The length of a region modeled in the present study is typically 500-1000 μm whereas the length scales in capillary electrophoresis can be 2-3 orders of magnitude higher. Another reason is that in the present investigation, the reaction and generation terms are assumed to be identically zero so the computational load is reduced. Despite the lower efficiency of FTCS and its ability to handle lower Peclet numbers, this method has proven sufficient for the current application. The Peclet number is the ratio of flux due to advection to flux due to diffusion.

A two-dimensional problem has also been solved using the finite-element flux corrected method. The flux corrected scheme is the method of choice for numerically solving hyperbolic conservation laws. The method was originally developed for 1-dimensional problems [10], [76], [77]. Zalesak [78] helped to make the FCT method used more widely. FCT was adapted to finite elements by Lohner et al. [79]. It is reasonably optimized for sharp boundaries in the solution, without creating spurious overshoots and undershoots. Georghiou [80, 81] implemented a finite element flux corrected method for studying gas discharge problems. The physics of gas discharge and electrophoresis have strong inherent similarities. The governing equations of both are advection-diffusion conservation laws coupled by the electric field. The media in both cases have bipolar charges. The differences are that electric fields in electrophoresis are lower and that the density of space charge is much smaller. In this thesis, existing numerical tools, developed by Georghiou [81] have been modified and applied to the problem of DNA sample stacking in electrophoresis. The advantage of using the numerical finite element flux-corrected transport (FE-FCT) method is that it is a two-dimensional model.

Since the physical transport conservation laws have electric field driving terms, the electric field must be computed. Electric field computation is based on Gauss' law for homogeneous media. For regions with non-uniform conductivity, charge conservation laws are used. The general solution involves convergence of the two approaches. Extending the current methods from one spatial dimension to two spatial dimensions brings additional complexity to this problem. Significant progress has been made in the computation of electric fields, as shown in a review by Takuma [82]. Takuma and Kawamoto [83] developed methods independent of Deutsch's assumption which states that the direction of electric field does not depend on conductivity. Al-Hamouz [84, 85] applied finite element methods to electric field computations.

In electrophoresis literature, it is commonly assumed that charge neutrality is guaranteed. Charge neutrality is a useful assumption for simplifying a numerical simulation. However, charge neutrality is not truly valid in regions of conductivity gradients. The validity of the charge neutrality assumption was addressed by Fife *et al.* [47] who theoretically showed that the traveling wave solution of moving boundaries was possible, under some limitations, even with the charge neutrality assumption. In the one-dimensional (1-D) model described in this thesis, the charge neutrality assumption has been used. In the two-dimensional (2-D) model, this simplifying assumption was not needed since it had an existing Poisson solver in its numerical procedure. A quantitative estimate of the error introduced without Poisson solver for similar transport algorithms is not available, although it is assumed to be negligible under typical electrophoresis conditions.

2. Selection of Numerical Approach

A finite difference method with the forward in time and central in space scheme has been used. The discretization used was to obtain very low Courant Number $Co \sim 0.005$ and $Pe < 2$. Typical discretization ranges are such that $Co < 0.5$ and $Pe < 2$. The use of such fine discretization has allowed the simulations to exceed the reported current density limitation compared with approaches that had coarser discretization. The FTCS method has the advantage of being extremely stable. As the speed of the wave is increased, this method introduces some numerical dispersion at marginal stability. The use of a low Courant number limits the errors to within acceptable limits.

3. Numerical Model for 1-Dimension: FTCS

The numerical model for the 1-D problem had the following parameters. The time step was $\Delta t = 5\times10^{-5}\ s$, and the spatial step was $\Delta x = 10^{-6}\ m$. The number of time steps could be up to $n_t = 30000$, depending on the current density or applied voltage. The number of spatial steps were $n_x = 500$, since the size of domain, *L*, was $500\mu m$. The time represented by the complete simulation was generally $T = 1.5\ s$, depending on the applied current density, which was typically $J = 1000\ A/m^2$. The mobility of TAPS, TRIS and chloride ions are 21×10^{-9}, 29×10^{-9}, 79×10^{-9} m^2/sV respectively as shown in Table 1. The diffusion coefficients are D_1, D_2, and D_3 which are 5.4×10^{-10}, 20.3×10^{-10}, 7.6×10^{-10} m^2/s, respectively. The mobility and diffusion of DNA are shown in Table 1 and in Table 2.

As described in the previous chapter in Section 2.4, the initial region consisted of a buffer region (A) with TAPS and TRIS ions, and a sample region (B) with chloride, DNA and TRIS ions, as well as another region A on the other side of the sample. There were two initial boundaries within the domain. After application of a current, a new region C was created and new boundaries propagated from the initial boundaries.

The concentration profiles in the initial condition are shaped as quarter-cosine curves which provided enhanced numerical stability compared with half-gaussian profiles. Additionally, this profile is representative of the natural diffusion that occurs at the free boundaries between the sample and the buffer. In this case, the numerical scheme is maintained at a high enough resolution such that the electrolyte boundaries are as sharp as the physical boundaries. The following parameters and relationships are used. All species in this model are considered to have a valence of +1 or –1. Due to charge neutrality, $c_1 + c_2 = c_3$. The conductivity at any position is $\sigma = F(c_1\mu_1 + c_2\mu_2 + c_3\mu_3)$. A standard explicit

Table 1. Mobility of Ions in Electrophoresis

Abbreviations are: LPA = linear polyacrylamide, pDMA = linear poly-N,N-dimethyl acrylamide, and ssDNA = single-stranded DNA

Species	**Mobility**
TRIS	$+29.5 \times 10^{-9}$ m^2/sV
acetate	-42.4×10^{-9} m^2/sV
borate	-65×10^{-9} m^2/sV
phosphate	-73×10^{-9} m^2/sV (approx. at pH 8.1)
cacodylate	-23.1×10^{-9} m^2/sV
TAPS	-21×10^{-9} m^2/sV
chloride	-79.1×10^{-9} m^2/sV

ssDNA	**mobility**
50	-35×10^{-9} m^2/sV
100	-32×10^{-9} m^2/sV
500	-21×10^{-9} m^2/sV
800	-18×10^{-9} m^2/sV
1000	-17×10^{-9} m^2/sV
5000	-16×10^{-9} m^2/sV

(2% pDMA, 0.5X TBE, 50°C, urea denaturing) [86]

ssDNA	**mobility**
50	-28×10^{-9} m^2/sV
100	-23×10^{-9} m^2/sV
200	-19×10^{-9} m^2/sV
500	-10×10^{-9} m^2/sV
800	-9.5×10^{-9} m^2/sV
1000	-9×10^{-9} m^2/sV
5000	-8×10^{-9} m^2/sV

(4% pDMA, 0.5X TBE, 50°C, urea denaturing) [86]

Experimental Values

(2% LPA, 1X TBE, 50°C, urea denaturing)

ssDNA	mobility
800	$-8.10^{-9} m^2/sV$

Table 2. Diffusion Coefficients of DNA in Electrophoresis

4% polyacrylamide gel at 45 C [6]

Size of ssDNA	Diffusion Coefficient
100	$2x10^{-11}$ m^2/sV
200	$8x10^{-12}$ m^2/sV
300	$6x10^{-12}$ m^2/sV
400	$5.5x10^{-12}$ m^2/sV
500	$5x10^{-12}$ m^2/sV

FTCS form as described by Martens [55] has been used. The numerical scheme for the buffer (TAPS) co-ion is

$$\begin{aligned} c_1(t+\Delta t,x) = c_1(t,x) &+ \frac{D_1\Delta t}{(\Delta x)^2}\big(c_1(t,x+\Delta x)-2c_1(t,x)+c_1(t,x-\Delta x)\big) \\ &- \frac{\Delta t}{2\Delta x}\big(c_1(t,x+\Delta)v_1(t,x+\Delta x)-c_1(t,x-\Delta x)v_1(t,x-\Delta x)\big) \end{aligned} \quad . \tag{3.1}$$

The scheme for the major sample component (chloride) co-ion is

$$\begin{aligned} c_2(t+\Delta t,x) = c_2(t,x) &+ \frac{D_2\Delta t}{(\Delta x)^2}\big(c_2(t,x+\Delta x)-2c_2(t,x)+c_2(t,x-\Delta x)\big) \\ &- \frac{\Delta t}{2\Delta x}\big(c_2(t,x+\Delta x)v_2(t,x+\Delta x)-c_2(t,x-\Delta x)v_2(t,x-\Delta x)\big) \end{aligned} \quad , \tag{3.2}$$

and the explicit scheme for the buffer counter ion (TRIS) is

$$\begin{aligned} c_3(t+\Delta t,x) = c_3(t,x) &+ \frac{D_3\Delta t}{(\Delta x)^2}\big(c_3(t,x+\Delta x)-2c_3(t,x)+c_3(t,x-\Delta x)\big) \\ &- \frac{\Delta t}{2\Delta x}\big(c_3(t,x-\Delta x)v_3(t,x-\Delta x)-c_3(t,x+\Delta x)v_3(t,x+\Delta x)\big) \end{aligned} \quad . \tag{3.3}$$

In the case of the counter-ion (TRIS), the direction of travel of the particles is reversed with respect to the other ions. This improves stability of the advection term

$\left(c_3(t,x-\Delta x)v_3(t,x-\Delta x)-c_3(t,x+\Delta x)v_3(t,x+\Delta x)\right)$ since the reversed terms cause the (*x-dx*) term ahead of the (*x+dx*) term.

As regards boundary conditions, in a hyperbolic system, the direction of the wave determines the direction in which the boundary conditions are specified. The boundary conditions at the start of the wave are given. Values that are ahead of the wave are determined by the wave itself. In this problem, the boundary values are fixed to reflect the dominant nature of the hyperbolic term, because the real boundary is far from the boundary in the domain for computation. The following Dirichlet boundary conditions were supplied to the numerical model. The subscript A denotes that these boundary conditions are in the A region.

$c_{1,A}(t,0)=cA$ (given)

$c_{1,A}(t,n_x)=c_{1,A}(t,n_x-1)$ value fixed by the approaching wave

$c_{2,A}(t,0)=0$ (given)

$c_{2,A}(t,n_x)=c_{2,A}(t,n_x-1)$ value fixed by the approaching wave

$c_{3,A}(t,1)=c_{3,A}(t,2)$ value fixed by the approaching wave

$c_{3,A}(t,n_x)=0$ (given)

Since there are two A regions on either side of the sample region (B), both the boundaries are in region A.

The solution of Equations (3.1), (3.2), and (3.3) yields the updated concentration of the three major components at the next time step. This is used to compute the local conductivity at any point. Since the current density is known, the local electric field can be computed. This electric field can be used to compute the velocity of the sample particle, given the mobility of the sample. The resulting sample concentration can be explicitly expressed as:

$$\begin{aligned} c_4(t+\Delta t,x) &= c_4(t,x)+\frac{D_4\Delta t}{(\Delta x)^2}\left(c_4(t,x+\Delta x)-2c_4(t,x)+c_4(t,x-\Delta x)\right) \\ &\quad -\frac{\Delta t}{2\Delta x}\left(c_4(t,x+\Delta x)v_4(t,x+\Delta x)-c_4(t,x-\Delta x)v_4(t,x-\Delta x)\right) \end{aligned}, \qquad (3.4)$$

where $v_4=\mu_4 E$, and E has been computed from the interaction of the three major ion components. Depending upon the mobility of the sample with respect to the buffer co-ion mobility, the simulations show different regimes of stacking.

Results of Simulations

The concentration c_1 is the concentration of TAPS$^-$ ion, c_2 is the concentration of chloride$^-$ ion and c_3 is concentration of TRIS$^+$ ion. In this simulation, the initial concentration was

$$c_1(x,0) = \begin{cases} 10 & x > 50 \\ 0 & 50 < x < 300, \\ 10 & x < 500 \end{cases}$$

$$c_2(x,0) = \begin{cases} 0 & x > 50 \\ 22.5 & 50 < x < 300, \\ 0 & x < 500 \end{cases}$$

$$c_3(x,0) = \begin{cases} 10 & x > 50 \\ 22.5 & 50 < x < 300. \\ 10 & x < 500 \end{cases}$$

The concentrations are in mM and the distances are in µm. The evolution of the sample concentration is shown in Figure 13 where the speed of the stable boundary in the sample region is 640 µm/s. In the numerical simulation, the size of the time steps are 5×10^{-5} s. Figure 13 shows every 1000th step of the simulation, hence the time step of the consecutive profiles displayed in the graph is 0.05 s.

The numerical simulation shows the evolution of the concentration profile forming a sharp self-stabilizing concentration boundary moving from the rear boundary of the initial sample location. The concentration of the buffer in the region just behind the moving boundary is different from the concentration in the buffer region outside the sample region and behind. A stationary concentration boundary is formed at the initial location of the rear sample boundary. The concentration boundary is initially relatively sharp and undergoes diffusion over time.

In the region of the leading boundary, the reverse case is observed. The boundary proceeds from its original position, spreading progressively. At the original position, a concentration boundary is formed which undergoes diffusion with time.

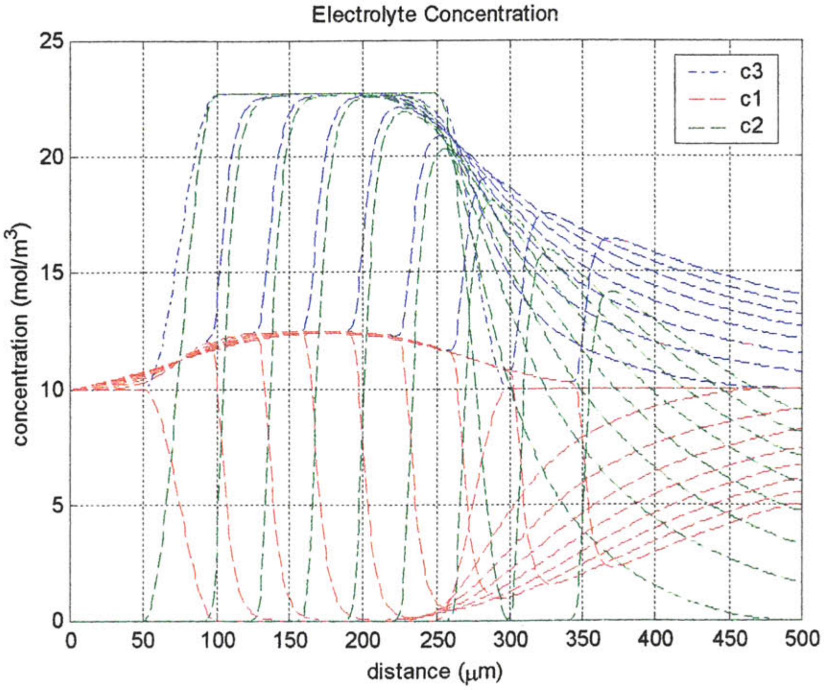

Figure 13. Concentration Profiles

Red, green and blue lines show TAPS, chloride and Tris ion concentrations. The time step between consecutive profiles displayed in the graph is 0.05 s. The speed of the stable boundary in the sample region is 640 μm/s. The Taps ion concentration changes at the trailing boundary to match the moving boundary concentration. The stable moving boundary maintains its shape. The leading moving boundary displays strong spreading behavior.

The electric field (Figure 14) profile after application of the electric field is inversely proportional to the conductivity. The electric field in the sample region is lower than the field in the region occupied by the buffer. As the rear stable boundary (on the left) moves to the right, it forms a region behind with a lower conductivity and hence a higher electric field compared with the sample region ahead of the boundary. Consequently, a wave of high electric field gradient moves along with the moving boundary. At the location of the leading boundary, the electric field gradient decreases with time, i.e. the electric field discontinuity is spread out across a longer length. At the two concentration boundaries, the electric field shows discontinuities which diffuse over time.

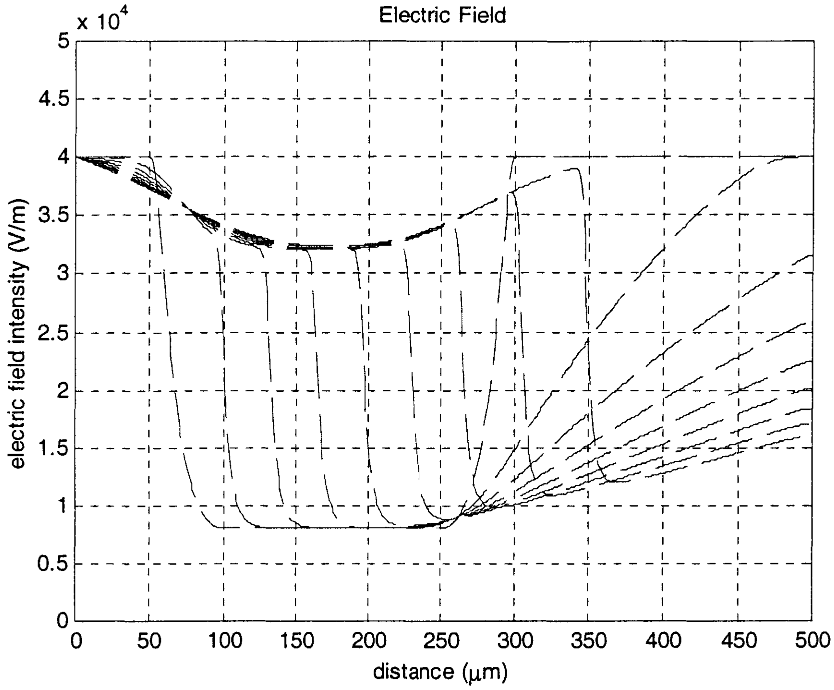

Figure 14. Electric Field Profile

This figure shows the corresponding electric field profile at time steps of 0.05. The initial electric field profile is shaped like a well. The high conductivity region of chloride has a lower electric field. The stable moving boundary moves ahead creating a high electric field as it progresses into the sample region. The interface between the high field and the region of low field is the location where stacking occurs.

The effect of the electric field on the minor sample component is shown. Two cases are considered. In the case of a sample which has a mobility less than the mobility of the buffer co-ion, the moving boundary from the rear crosses the sample. The sample, being in a region of higher electric field intensity, is sped up and its concentration increases as predicted by theory in Chapter 2, Section 4. The rear boundary of the sample undergoes stacking and reaches steady state after the width of the boundary crosses the sample. As time progresses, the moving boundary crosses over more sample, increasing the sample concentration to a similar value, as shown in Figure 15. This is a characteristic feature of sample stacking when the sample is slower than the buffer co-ion.

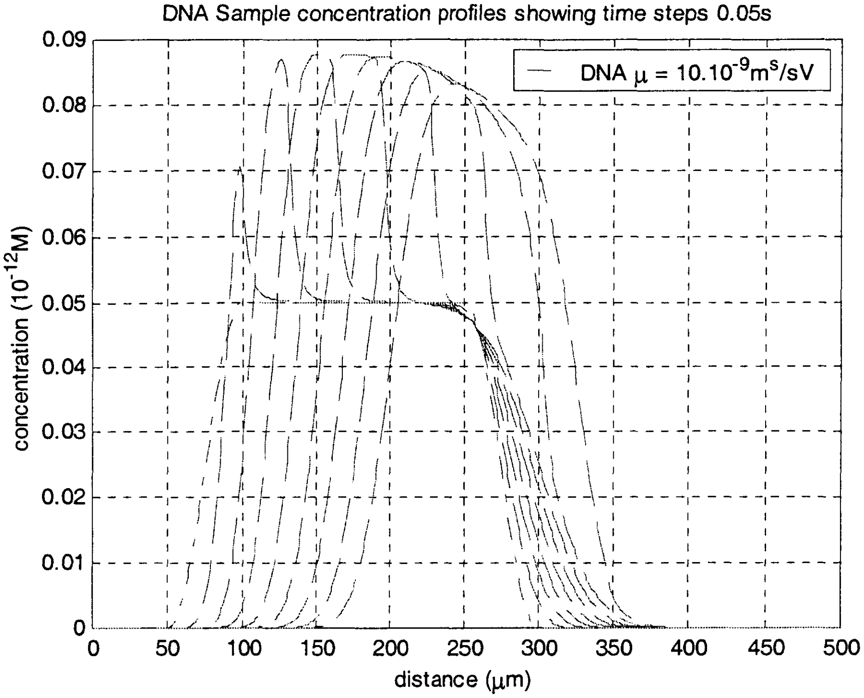

Figure 15. Sample Stacking

Sample stacking demonstrated by the concentration profiles of the sample. In this case, the sample concentration after stacking is 0.875 x 10^{-12} M. The analytical predicted maximum concentration is 0.0873 x 10^{-12} M. The numerical method and the analytical method are in good agreement.

In the second case of sample stacking, the sample has a mobility higher than the mobility of the buffer co-ion. A sharp sample peak is shown following the moving boundary. The rear part of the sample plug, which comes in contact with the moving boundary, gets trapped in the moving boundary. This form of stacking lead to relatively higher factors of stacking compared with the previous case. The amount of stacking is limited by the width of the boundary in which it is constrained. The width of the moving boundary has been shown to be proportional to the diffusion constants of the electrolytes and inversely proportional to the speed of the moving boundary. This form of stacking is shown in Figure 16.

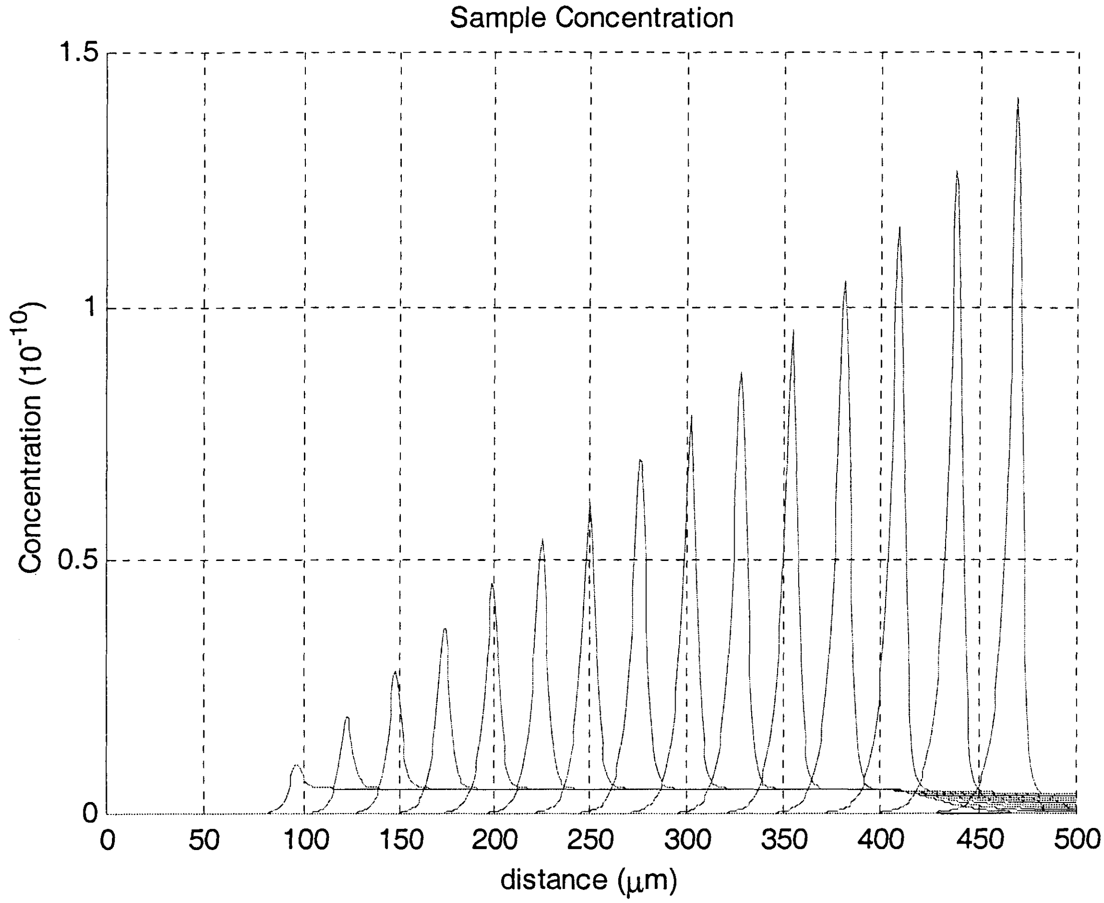

Figure 16. Sample Self-Stacking

Sample self stacking demonstrated by the concentration profiles of the sample. In this case, the sample concentration increases as the boundary moves across the injector. Stacking is sharp due to the sample being constrained at the moving boundary.

4. Comparison of Numerical Result with Theoretical Prediction

The stacking ratio of 1.75 from analytical model compares very well with the result from the numerical model of 1.746. The difference is 2.2%.

The boundary speed obtained from analytical model is 664 μm/s whereas the speed obtained from the numerical model is 640 μm/s. The difference is speed is 3.75%.

The width of the boundary as measured using the Longsworth [87] criterion resulted in a width which different from that predicted by theory. The theoretically computed width of the boundary is 4.725 μm whereas the numerical simulation results in approximately 15 μm.

5. Numerical Model for Two Dimensions

Two numerical models were implemented to demonstrate the process of electrophoresis in two-dimensional geometries of microfabricated capillaries. The double-T injector is inherently a two-dimensional configuration. The two-dimensional model can be used to demonstrate the phenomenon of sample loading and sample injection. Moreover, a complete consideration of the two dimensional geometry can show how the sample plug concentration varies across the channel width. This seems to be important since the electric field undergoes sharp turns and their curvature can result in unexplored effects on the concentrations.

Preliminary Model

The first method was implemented using FEMLAB. This model utilized a geometry defined by a double T injector. The sample used in this model consisted of only one species of DNA. The electric field was solved for voltages applied at the respective electrodes. Insulation boundary conditions were assumed at all other boundaries. As a result, for any given set of applied voltages, the electric field was constant over time. The electric field variation was due to the geometry effects. The simulation consisted of two steps. In the first step, the sample was introduced into the injector and in the following step, the sample was injected from the injector into the separation channel for separation. The results from these simulations showed profiles across the channel which resembled real experimental images. However, this model did not reveal any sample stacking.

The channels in this model are 100 μm wide, and an injector offset of 200 μm is used. A voltage is applied so as to obtain approximately 1500 V/m in the injector. The inner corners where the electric field lines bend are found to have a higher electric field.

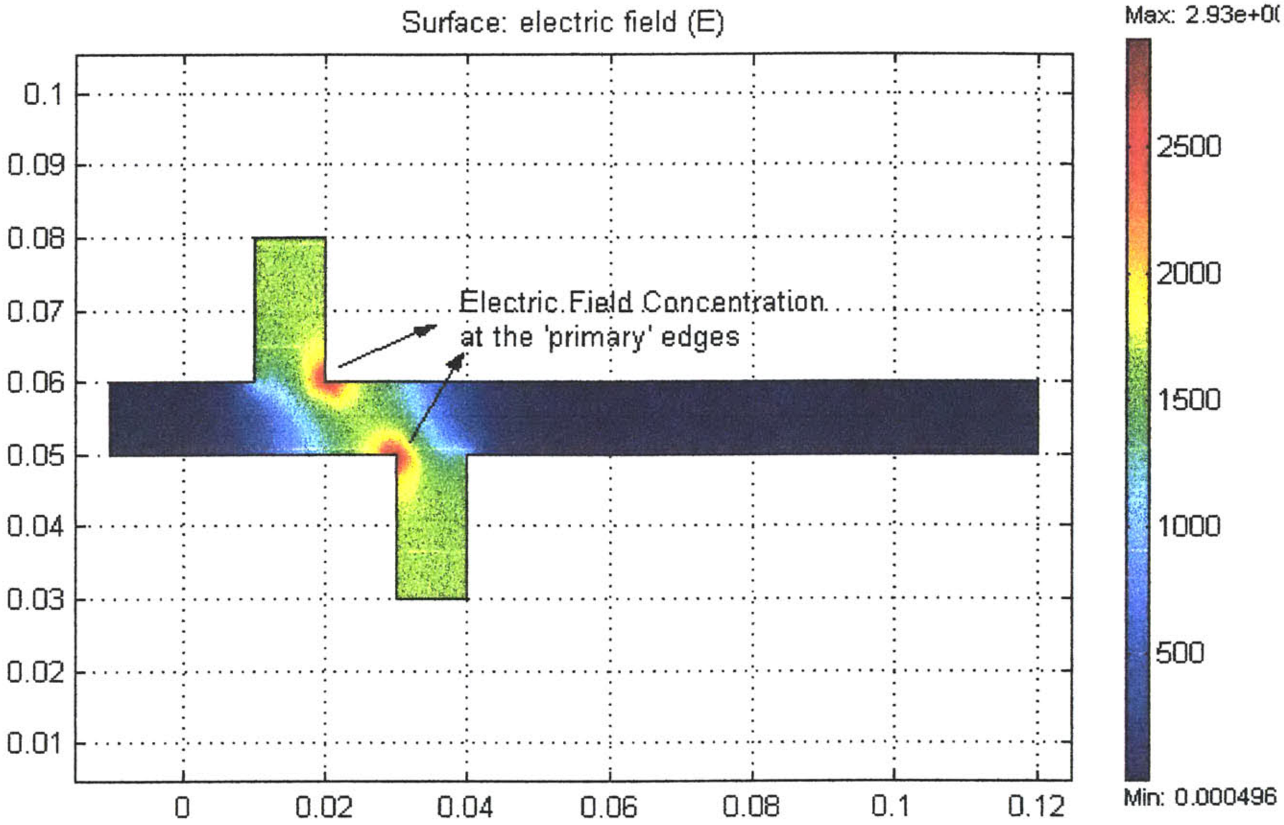

Figure 17. Electric Field Intensity
The scale bar for the electric field is in units of V/m. The units of the channel in both dimensions is in 10^{-2} m. The effect of geometry on electric field shows that a voltage applied between the sample and waste ends causes electric field concentration at the inner edges. This is an effect of the geometry of the domain.

The electrokinetic effect of the applied electric field is shown in the following simulations. The first part is the sample introduction and the second part is the sample injection. The simulation shows the concentration distribution during sample introduction. This distribution has a strong visual resemblance with experimental observations of sample loading done in the BioMEMS Lab. The sample is seen to proceed faster at the inner corners. In this model only one species of DNA sample is used and the electric field is kept constant.

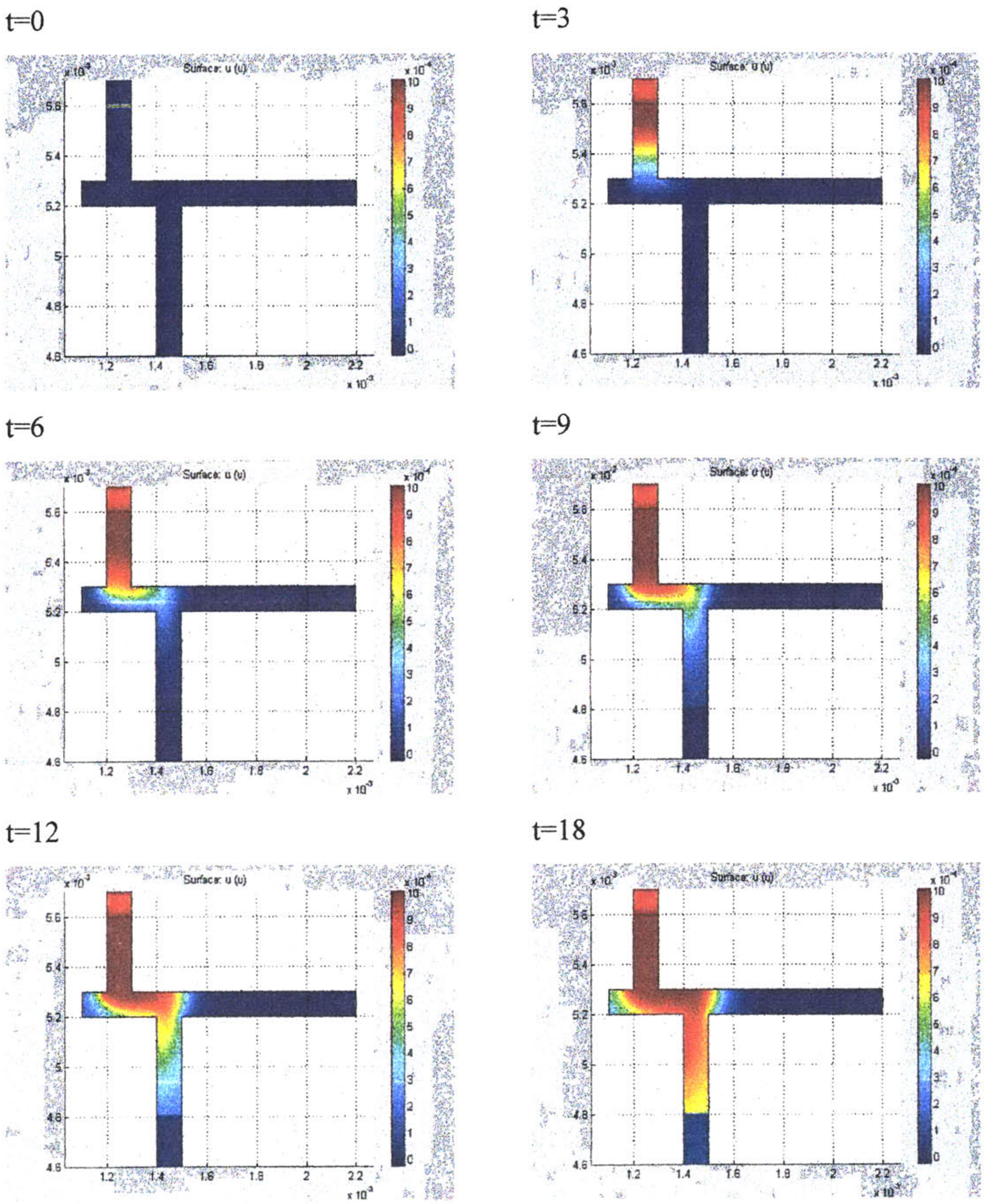

t=0

t=3

t=6

t=9

t=12

t=18

Figure 18 Sample Introduction in Microdevice

The scale bar for the electric field is in units of V/m. The units of the channel in both dimensions is in meters. Simulation of sample loading performed with a preliminary model using FEMLAB.

In the second part, the voltage is applied across the main channel causing a nearly uniform electric field in it and a smaller field at the interfaces with the two arms of the injector. The leakage of the sample from these arms can be seen in Figure 19 for the case of *t* = 12. A

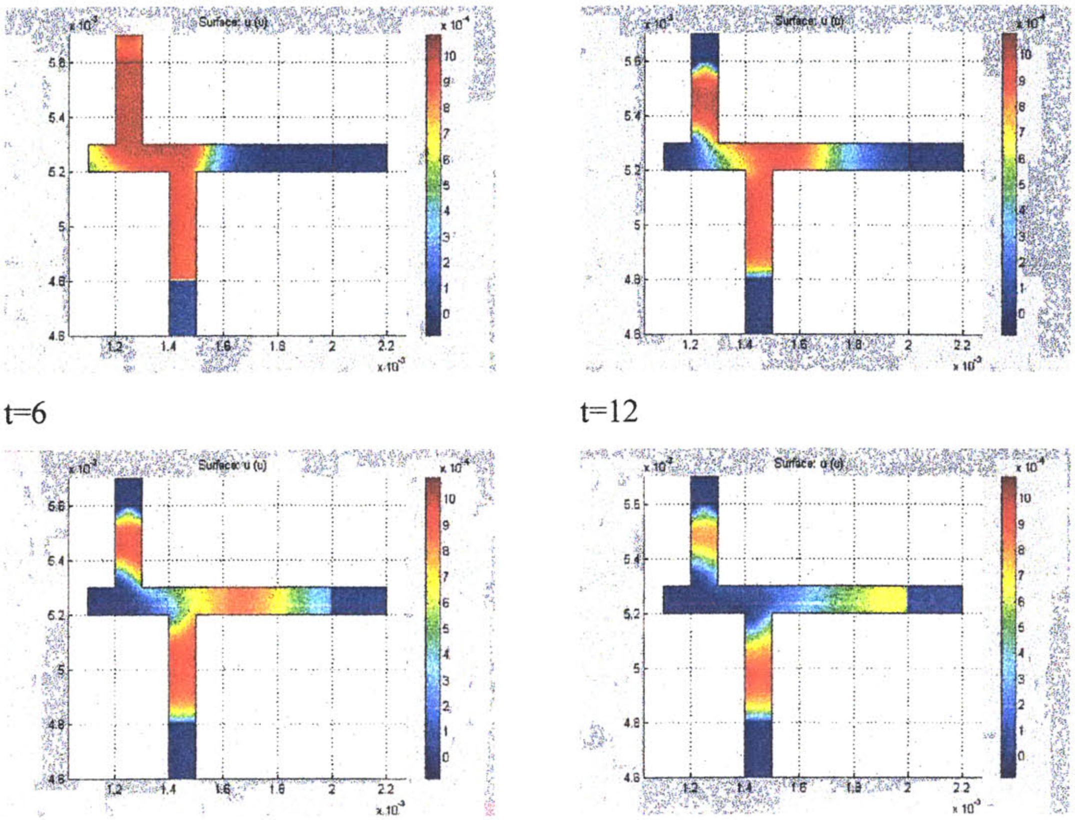
t=0

t=3

t=6

t=12

Figure 19. Simulation Sample Injection

The scale bar for the electric field is in units of V/m. The units of the channel in both dimensions is in meters. Simulation of sample injection using preliminary model does not demonstrate sample stacking.

pullback voltage has also been applied which restricts the sample leakage from the sample arm in the same figure. This model could not demonstrate any stacking because the electrolyte dynamics could not be incorporated into the solver. Another limitation of the method was its excessive numerical diffusion, which would have made the solution less exact, even if the electrolyte dynamics had been incorporated. The limitations of modeling electrolyte dynamics and numerical diffusion have been minimized in the method shown in the next section.

Improved Model with Electrolyte Dynamics

In the second method, a more comprehensive model has been implemented. Utilizing a finite element method (FEM) solver for advection and diffusion transport along with a Poisson solver for the computation of electric field. The conservation equations are coupled by the electric field. The transport equations are solved by the use of the flux-corrected transport (FCT) algorithm. The implementation details of FCT are described in the following section. The details of this method of solution are described in [81] and [80].

The geometry of the domain was defined and the initial conditions and boundary conditions were applied. The domain consisted of a double T injector of 100 μm width and injector offset of 100 μm. The initial condition is the complete channel filled with the buffer ions.

Two steps are used in the model for sample injection. The first step is sample introduction from the sample well. This process is essentially a moving boundary electrophoresis (MBE) process. As the sample progresses, it occupies the injector and moves towards the waste well. The final condition of sample introduction serves as the initial step of sample injection. In the following step of sample injection, the voltage is applied across the length of the domain. The dynamics of the sample and the electrolytes are seen to be similar to the results observed using the one-dimensional analysis. This model had the additional advantage of predicting variations across the channel, and the feature can be used to study the effect of the pull-back or constraining voltage at the sample and waste injectors on the sample leakage into the chamber.

FCT: The Flux Corrected Transport Scheme

This description is based on Zalesak's [78] method. A hyperbolic system of conservation laws may be represented as

$$w_t + f_x = 0 . \tag{3.5}$$

w and f are defined at the spatial grid points x_i and temporal grid points t^n, and

$$\Delta x_i = \frac{1}{2}(x_{i+1} - x_{i-1}) . \tag{3.6}$$

The transportive fluxes $F_{i+1/2}$ are functions of *f* at one or more of the time levels t^n. The finite difference approximation is

$$w_i^{n+1} = w_i^n - \frac{1}{\Delta x_i}[F_{i+1/2} - F_{i-1/2}] . \tag{3.7}$$

The functional dependence of F on *f* defines the integration scheme. It is well known that higher order schemes cause dispersive ripples and low order schemes cause excessive diffusion.

Steps of the FCT Method

1. The flux according to a low order method $F_{i+1/2}^L$ is computed.
2. The flux according to a high order method $F_{i+1/2}^H$ is computed.
3. The "antidiffusive flux" is computed:

$$A_{i+1/2} = F_{i+1/2}^H - F_{i+1/2}^L . \tag{3.8}$$

3. The updated low order "transported and diffused" solution is computed:

$$w_i^{td} = w_i^n - \frac{1}{\Delta x_i}[F_{i+1/2}^L - F_{i-1/2}^L] . \tag{3.9}$$

5. $A_{i+1/2}$ is limited in a manner such that w_i^{n+1} as computed in step 6 below is free of extrema not found in w_i^{td} or w_i^n

$$A_{i+1/2}^C = C_{i+1/2} A_{i+1/2} \text{, where } 0 \le C_{i+1/2} \le 1 . \tag{3.10}$$

6. The limited antidiffusive fluxes are applied:

$$w_i^{n+1} = w_i^{td} - \frac{1}{\Delta x_i}[A_{i+1/2}^C - A_{i-1/2}^C] . \tag{3.11}$$

The critical step is 5. In the absence of a flux limiting step, $(A_{i+1/2}^C = A_{i+1/2})$ or $C_{i+1/2} = 1$. The solution would simply be the time advanced high order solution.

Flux Limiting Algorithm

As indicated by step 5, the antidiffusive flux $A_{i+1/2}$ is limited such that $A^C_{i+1/2} = C_{i+1/2}A_{i+1/2}$, with $0 \le C_{i+1/2} \le 1$ and such that $A^C_{i+1/2}$ acting in concert with $A^C_{i-1/2}$ does not allow Equation (3.11) to exceed some value $w_i^{\max}$ nor fall below $w_i^{\min}$. Determination of $w_i^{\max}$ and $w_i^{\min}$ is performed from the following:

$$w_i^a = \max(w_i^n, w_i^{td}), \tag{3.12}$$

$$w_i^{\max} = \max(w_{i-1}^a, w_i^a, w_{i+1}^a), \tag{3.13}$$

$$w_i^b = \min(w_i^n, w_i^{td}), \text{ and} \tag{3.14}$$

$$w_i^{\min} = \min(w_{i-1}^b, w_i^b, w_{i+1}^b). \tag{3.15}$$

Three quantities are defined:

$$\begin{aligned} P_i^+ &= \text{the sum of all antidiffusive fluxes into grid point } i \\ &= \max(0, A_{i-1/2}) - \min(0, A_{i+1/2}) \end{aligned} \tag{3.16}$$

$$Q_i^+ = (w_i^{\max} - w_i^{td})\Delta x_i \tag{3.17}$$

$$R_i^+ = \begin{cases} \min(1,\ Q_i^+ / P_i^+) & \text{if } P_i^+ > 0 \\ 0 & \text{if } P_i^+ = 0 \end{cases} \tag{3.18}$$

If it is assumed that $w_i^{\max} \ge w_i^{td}$ (it must be), all three of the above quantities are positive and R_i^+ represents the least upper bound on the fraction which must multiply all the antidiffusive fluxes *into* grid point *i* to guarantee no overshoot at the grid point *i*.

Similarly three more corresponding quantities are defined:

$$\begin{aligned} P_i^- &= \text{the sum of all antidiffusive fluxes away from grid point } i \\ &= \max(0, A_{i+1/2}) - \min(0, A_{i-1/2}) \end{aligned} \tag{3.19}$$

$$Q_i^- = (w_i^{td} - w_i^{\min})\Delta x_i \tag{3.20}$$

$$R_i^- = \begin{cases} \min(1,\ Q_i^- / P_i^-) & \text{if } P_i^- > 0 \\ 0 & \text{if } P_i^- = 0 \end{cases} \tag{3.21}$$

It is again assumed that $w_i^{\min} \leq w_i^{td}$, and as a result R_i^- represents the least upper bound on the fraction which must multiply all antidiffusive fluxes *away from* grid point *i* to guarantee no undershoot at the grid point *i*.

Finally, it is observed that all antidiffusive fluxes are directed away from one grid point and into an adjacent one. Limiting will therefore take place with respect to undershoots for the former and with respect to overshoots for the latter. A guarantee that neither event comes to pass demands a minimum be taken:

$$C_{i+1/2} = \begin{cases} \min(R_{i+1}^+, R_i^-) & \text{if} \quad A_{i+1/2} \geq 0 \\ \min(R_i^+, R_{i+1}^-) & \text{if} \quad A_{i+1/2} < 0 \end{cases} . \tag{3.22}$$

6. Results of Simulations

The numerical simulation using two-dimensions provided the following results. The concentration distribution of the three major electrolytes was obtained. The resulting concentrations of chloride, TAPS and TRIS 2 seconds after injection are presented in the following plots. The units of concentration are molecules/m^3. The conversion for molecules/ m^3 to mM is the following – 1 mM = 6.02x10^{23} molecules/m^3.

In Figure 20, there is a region where TAPS is nearly absent, this being the region where chloride and the sample are present. The region rich in chloride is the region where sample is present (Figure 21). Just behind it, there is no chloride present. This shows the formation of a stable boundary. The leading part of the chloride region shows a spreading effect, consistent with the 1-dimensional result. In the figure showing the concentration of TRIS (Figure 22), a higher concentration is observed in the region where chloride is present. Since TRIS acts to neutralize the other ions, and due to the high concentration of chloride, its concentration is higher too.

The concentration of the sample shows stacking at the rear boundary (Figure 23). The effect of changing the pullback voltage after injection can also be demonstrated by this model. The effect of the applied pullback voltage is shown in [88].

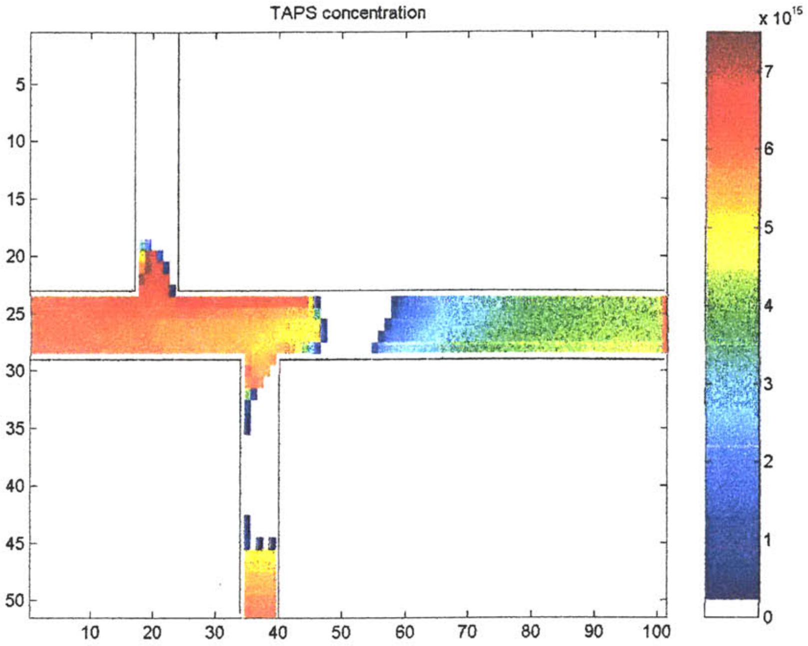

Figure 20. TAPS Concentration After 2 s of Injection

The concentration scale bar is in units of molecules/m^3. The horizontal channel dimensions are in units of 16 x10^{-5} m, and the vertical channel dimensions are in units of 20x10^{-5} m. The region where TAPS is nearly absent is also where chloride is present.

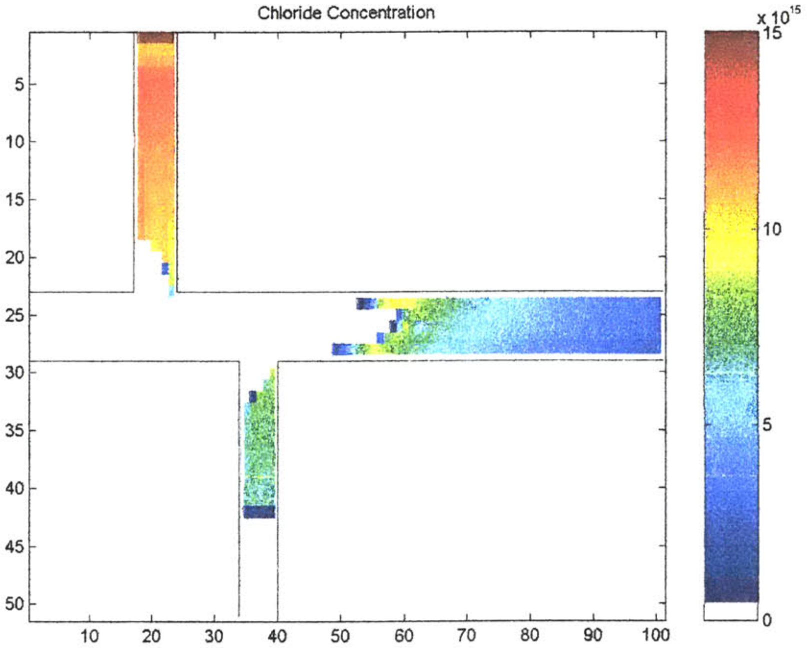

Figure 21. Chloride Concentration After 2 s of Injection

The concentration scale bar is in units of molecules/m^3. The horizontal channel dimensions are in units of 16 x10^{-5} m, and the vertical channel dimensions are in units of 20x10^{-5} m.

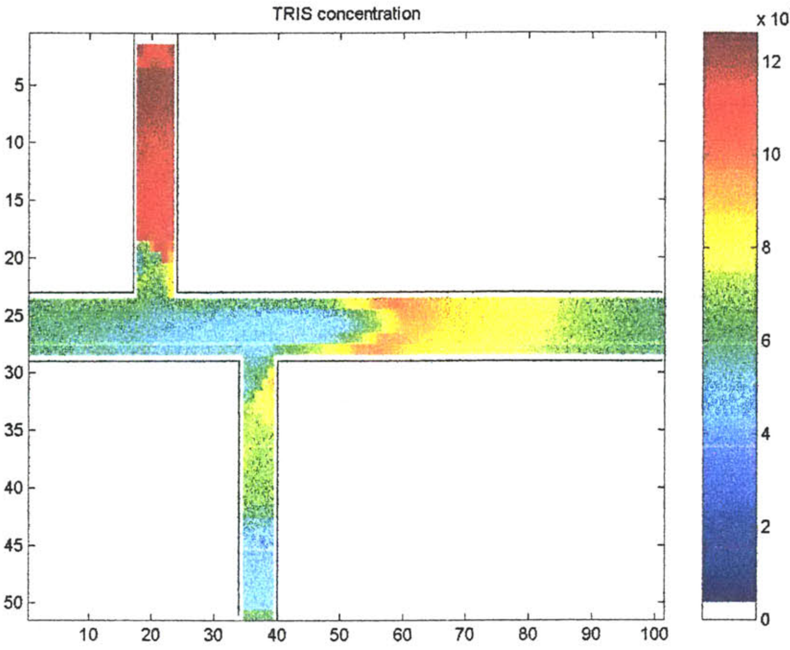

Figure 22. TRIS Concentration After 2 s of Injection

The concentration scale bar is in units of molecules/m^3. The horizontal channel dimensions are in units of 16 x10^{-5} m, and the vertical channel dimensions are in units of $20\text{x}10^{-5}$ m.

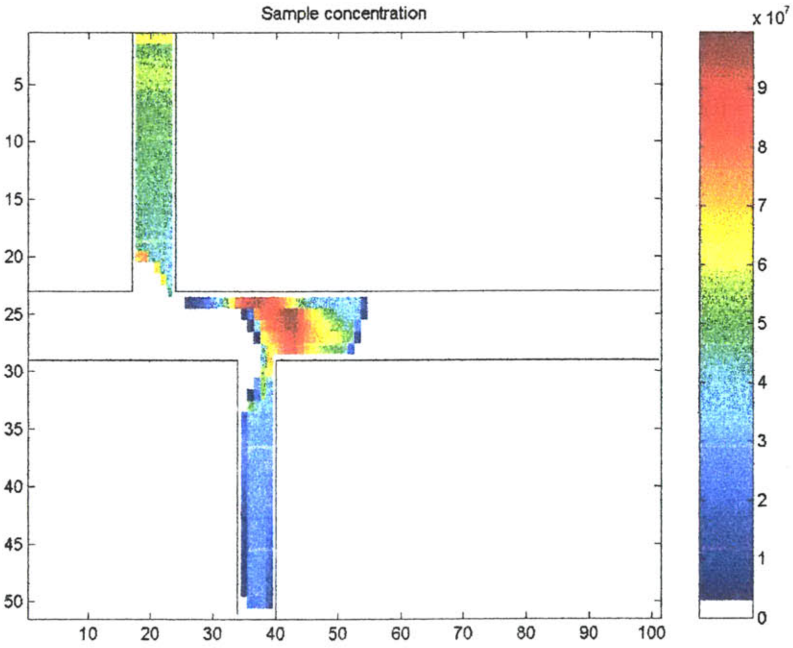

Figure 23. DNA Sample Concentration after 2 seconds.

The concentration scale bar is in units of molecules/m^3. The horizontal channel dimensions are in units of 16 x10^{-5} m, and the vertical channel dimensions are in units of $20\text{x}10^{-5}$ m. The figure shows sample stacking of DNA to form a sharp peak at the rear end of the plug. No pullback voltages were applied in the model. Sample leakage as a result occurring at the sample arm after the sample plug has passed the sample arm can be seen.

7. Predictions of the model

The model can predict the effects of the following factors on stacking:

Case 1: mobility of sample < mobility of buffer co-ion
    (a) sample mobility
    (b) buffer mobility,
Case 2: mobility of sample > mobility of buffer co-ion
    (c) injector length
    (d) width of boundary, which depends on the applied electric field and buffer mobility

The Effect of Sample Mobility

The effect of sample mobility on stacking has been described earlier in the previous chapter. Stacking is predicted for the case when the sample mobility is less than the buffer mobility. However, as the sample mobility approaches, or exceeds the buffer ion mobility, the sample stacking predicted becomes infinite. In reality, this mode of stacking undergoes a transition and stacking becomes diffusion limited. For samples slower than the buffer, the effect of diffusion is not as strong due to the relatively lower concentration gradients. For the case of samples faster than the buffer, the sample is constrained to stay in the boundary, and therefore the boundary thickness becomes an important parameter. The thickness of the boundary can also be estimated theoretically. This width is proportional to the product of the leading and trailing ion mobility and inversely proportional to the difference between them. The width is also inversely proportional to the speed of the moving wave. Since the speed of the wave is proportional to the applied field and the concentration/conductivity of the sample mixture, a higher electric field results in a sharper boundary.

The distinction between the cases of sample of mobility greater than or less than the buffer is very important. The slower samples show stacking which depends only on the concentration and mobility of the sample major component, and it is independent of the applied voltage. The faster samples undergo stacking in which they are constrained to stay in the boundary, hence their stacking is affected by the applied voltage, sample conductivity, and difference between the mobility of the leading and trailing buffer.

The effect of sample mobility on stacking is shown in Figure 24. For a given buffer, stacking is higher when the sample mobility is higher. In these cases, chloride is the stacking ion and TRIS is the counter ion.

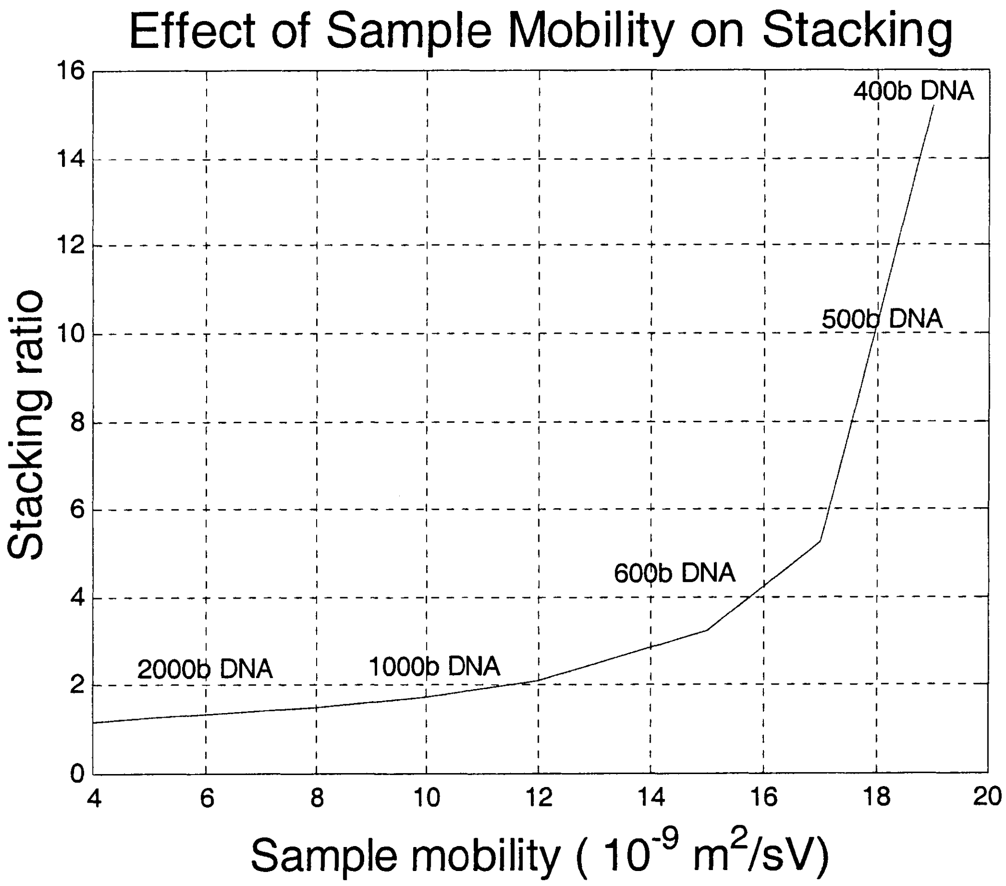

Figure 24. Effect of Sample Mobility on Sample Stacking

In this analysis, diffusion has been neglected. In reality, the stacking ratios achieved for the cases which predict higher stacking ratios will be reduced due to diffusion. This model over predicts the stacking ratio, especially for faster ions. For sample stacking such that sample mobility is less than the mobility of the buffer co-ion, the stacking ratio depends on the following:

$$\text{Stacking ratio} = \frac{v_{b3} - v_{X,C}}{v_{b3} - v_{X,B}} = \frac{(\mu_2 - \mu_X)E_B}{(\mu_1 - \mu_X)E_C} = \frac{(\mu_2 - \mu_X)\mu_1}{(\mu_1 - \mu_X)\mu_2}. \tag{3.23}$$

The Effect of Buffer Mobility

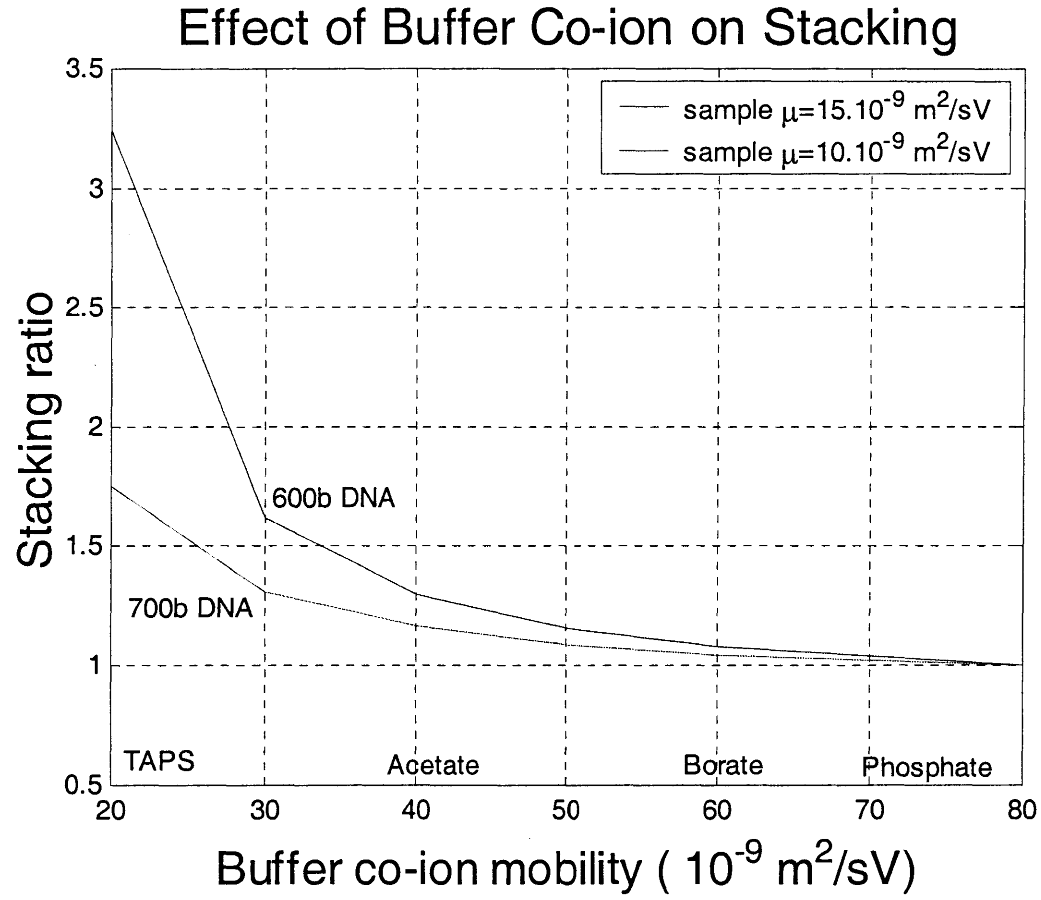

Figure 25. Effect of Buffer Ion Mobility on Stacking

This effect is true for the sample mobility less than the buffer mobility. Two effects are demonstrated: a) higher mobility of the sample results in higher stacking, and b) for the same sample, stacking decreases with an increase in buffer ion mobility with respect to the stacking ion (chloride) mobility. The mobilities of common buffer co-ions are also shown. This explains why phosphate buffer stacks less than acetate buffer.

The equation for stacking ratio also reveals the effect of changing the mobility of the buffer. A graphical representation is made for two cases of sample mobility and the effect of buffer for samples with compositions as shown in Figure 25. For a given sample mobility, stacking increases as the buffer mobility is reduced. In these cases, chloride is the stacking ion and TRIS is the counter ion. Two effects are demonstrated: a) higher mobility of the sample results in higher stacking, and b) for the same sample, stacking decreases with an increase in buffer ion mobility with respect to the stacking ion mobility. The mobilities of common buffer co-ions choice (TAPS, acetate, borate, and phosphate) are also shown in Figure 25. This explains why phosphate buffer stacks less than acetate buffer.

The Effect of Injector Length

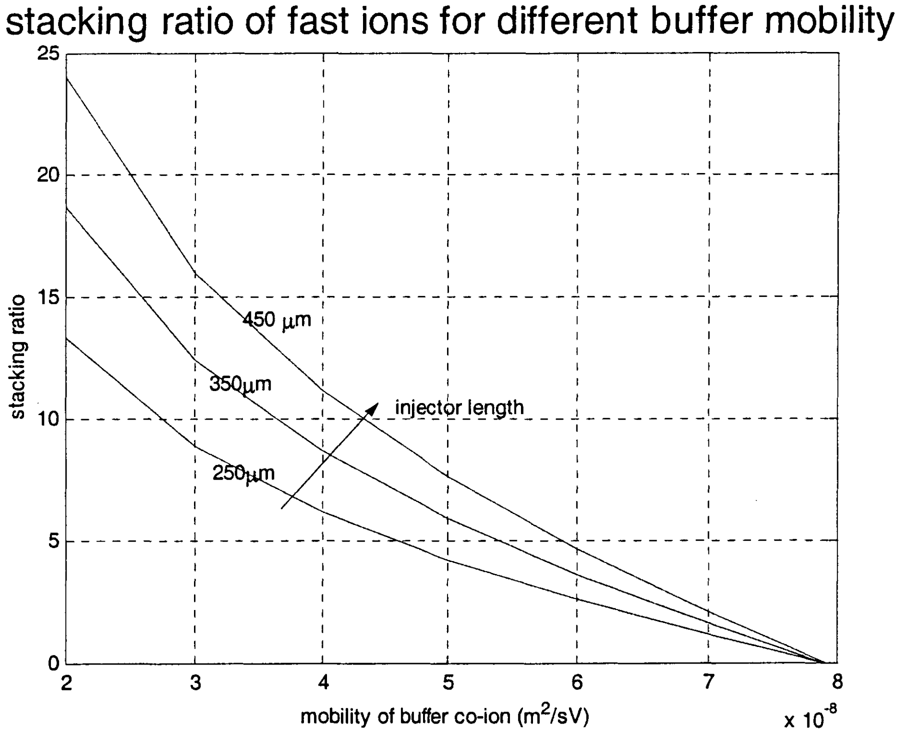

Figure 26. Sample with mobility higher than buffer co-ion mobility stacks as buffer mobility and injector length are changed.

As the buffer becomes slower with respect to the stacking ion (chloride), the width of the boundary decreases, causing higher stacking. An increase in the length of the injector also causes higher stacking as more sample is swept into the boundary of the same width.

The effect of injector length on stacking depends on the type of stacking. In sample stacking for which the sample mobility is less than the buffer mobility, the injector length plays no role in sample stacking. In the case of sample self-stacking, the sample is swept into the moving boundary as it passes the sample. As a result, the sample stacks proportional to the length of the injector as shown in Figure 26. As the buffer becomes slower with respect to the stacking ion (chloride), the width of the boundary decreases, causing higher stacking. An increase in the length of the injector also causes higher stacking as more sample is swept into the boundary of the same width.

Effect of Electric Field and Buffer Mobility in Sample Self-Stacking

When the DNA sample mobility is greater than the buffer co-ion, the DNA sample is confined to the width of the moving boundary. The width of the moving boundary has been shown by Longsworth [89] to be

$$w = \frac{4RT}{Fv_b} \frac{\mu_2 \mu_1}{\mu_2 - \mu_1}, \tag{3.24}$$

where w = width of the boundary, R = universal gas constant, T = temperature, F = Faraday number, v_b = boundary speed, μ_1 = mobility of the leading ion, μ_2 = mobility of the trailing co-ion and v = speed of the boundary.

The Effect of Boundary Speed and Applied Electric Field

The speed of the boundary is obtained from

$$v_b = \frac{Jt_2}{Fc_B}, \tag{3.25}$$

where J is the current density, t is the transference number of the leading ion, F is the Faraday number, and c is the concentration of the leading ion. Since $J = \sigma_A E_A = c_A FE(\mu_1 + \mu_3)$, the current density is proportional to the electric field. The boundary speed is then

$$v_b = E_A \mu_2 \frac{c_A}{c_B} \frac{(\mu_1 + \mu_3)}{(\mu_2 + \mu_3)}, \tag{3.26}$$

which shows that the width of the boundary decreases as the applied electric field increases. When the applied voltage is increased, the boundary width is decreased. The sample is constrained in a narrower region so sample self-stacking is higher. It also shows that the width is proportional to the conductivity ratio of the sample (chloride + TRIS) and to the conductivity of the running buffer (TAPS + TRIS).

The speed can also be increased by decreasing the concentration of the chloride with respect to the concentration of the buffer. As an example, with TTE buffer and chloride, E = 100 V/cm, cA = 10 mM, cB = 23 mM, $\mu_1 = 21\times10^{-9} m^2/sV$, $\mu_2 = 79\times10^{-9} m^2/sV$ and $\mu_3 = 29.1\times10^{-9} m^2/sV$. Then, v_b = 160 μm/s. As shown in the next chapter, this is verified from experimental data.

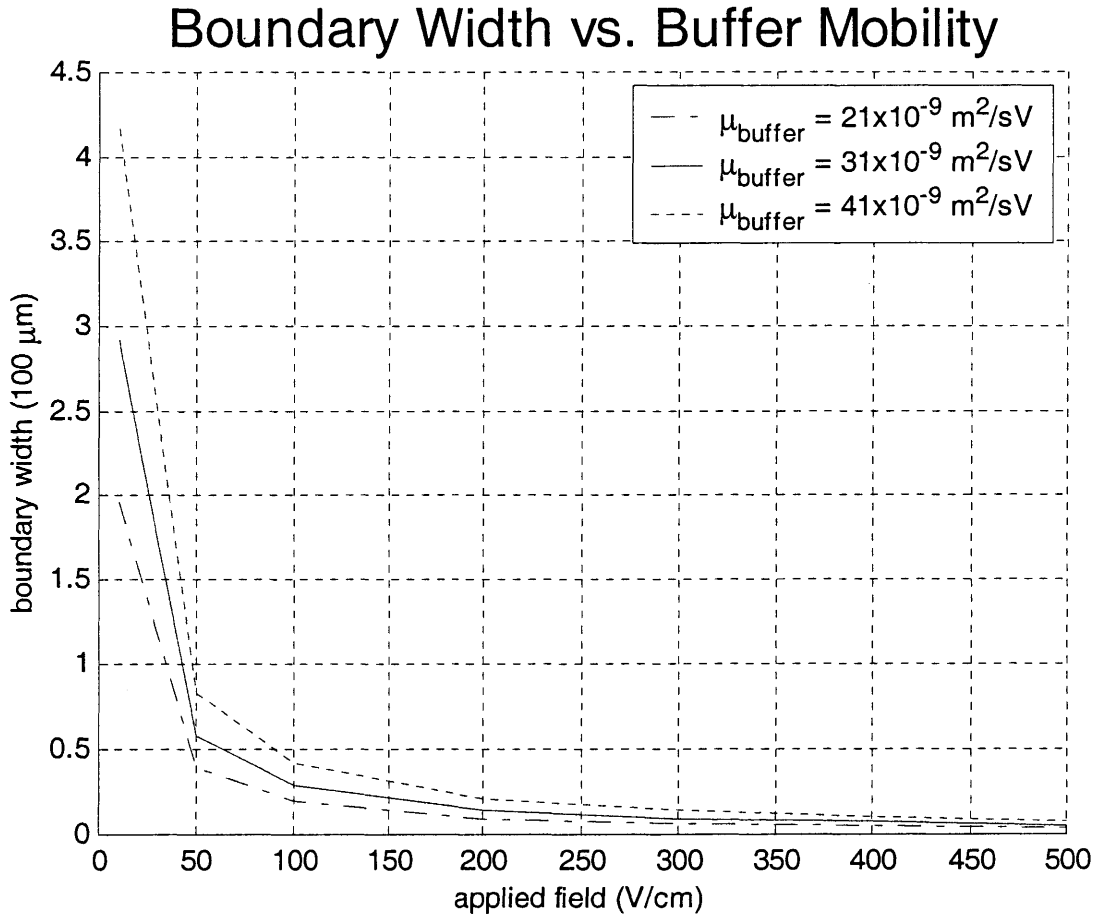

Figure 27. Stacking of sample with mobility higher than buffer co-ion mobility stacks higher for higher applied electric fields.

The boundary width is in units of 10^{-4} m. The higher electric field decreases the width of the boundary and therefore the fast ions stack higher. An increased electric field does not directly affect the stacking of slow sample ions. Slower buffer ions cause formation of narrower boundaries causing higher sample stacking for fast sample ions. The current density varies from 49 to 2462 A/m^2 for applied field of 10 to 500 V/cm, and the speed of the moving boundary changes from 16 to 795 μm/s for the case of buffer with mobility 21×10^{-9} m^2/sV.

. The estimated width of the boundary using Longsworth's [89] criterion is $w = 20$ μm based on the example values given above. This indicates that DNA with size 500 bases or less will be stacked in that boundary. As the voltage is increased, the boundary width will change as shown in Figure 27. The higher electric field decreases the width of the boundary and therefore the fast ions stack higher. An increased electric field does not directly affect the stacking of slow sample ions.

Chapter 4. Validation of Numerical Model

In this chapter, the results of the numerical model are compared with experimental data. The experimental data is available in the form of images obtained from video microscopy. Each experiment of imaging sample stacking of DNA was performed on a microcapillary device and imaged using a microscope as described in Section 1.7. The images were analyzed to obtain information which could yield a clear understanding of the phenomenon of sample stacking. The analytical model described in Chapter 2 is based on the theory of moving salt boundaries and applicable simplifying assumptions. The goal of this part of the thesis was to quantitatively verify the validity of the numerical model for prediction of sample stacking.

1. Extraction of Key Information from Image Data

The experimental data used in this thesis was made available by M. Vazquez who performed the experiments for her thesis [5].

Experimental Method and Image Pre-Processing

The experimental data files were created using Openlab® software. Each data file in this format is a series of images. The files were viewed using the software Volocity®, which is another product from Improvision Inc., the maker of Openlab. Volocity is compatible with Openlab, and it has superior image viewing and processing features. A very helpful feature of Volocity was its ability to display a set of good resolution images simultaneously.

The images in the data files were sampled at 1/8 seconds. This information was helpful in understanding the rate of change of position of the stacked sample. Sets of images were displayed as an array on the computer monitor to view their features. Since the images did not have time stamps on them, extra care was taken to ensure that the number of frames between the images were counted correctly.

The initial images display the sample occupying the sample injector. During sample injection, the sample not only moved ahead but also showed a characteristic sharpening at its rear boundary as shown in Figure 28.

frame_01 (t = 0 s)

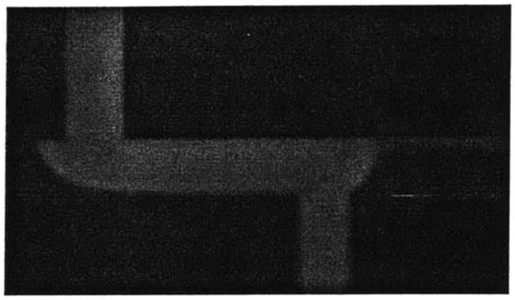

frame_06 (t = 0.625 s)

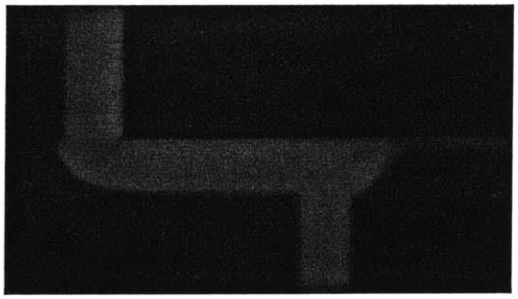

frame_11 (t = 1.25 s)

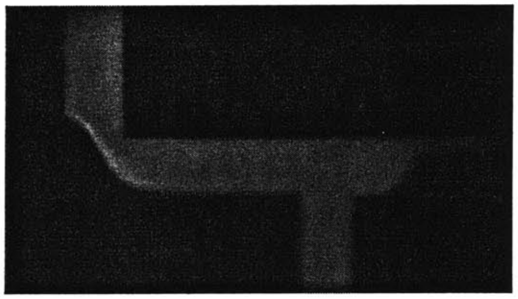

frame_16 (t = 1.875 s)

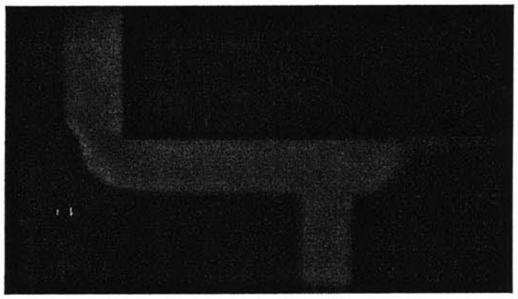

frame_21 (t = 2.5 s)

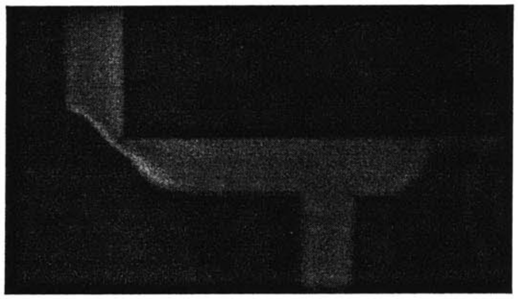

frame_26 (t = 3.125 s)

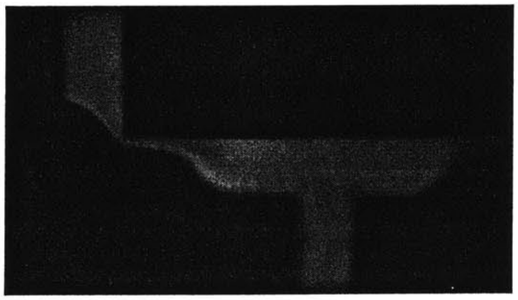

frame_31 (t = 3.75 s)

frame_36 (t = 4.375 s)

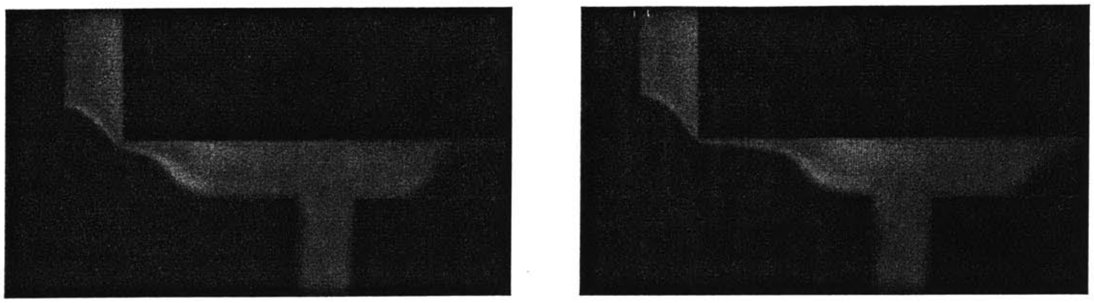

frame_41 (t = 5 s) frame_46 (t = 5.625 s)

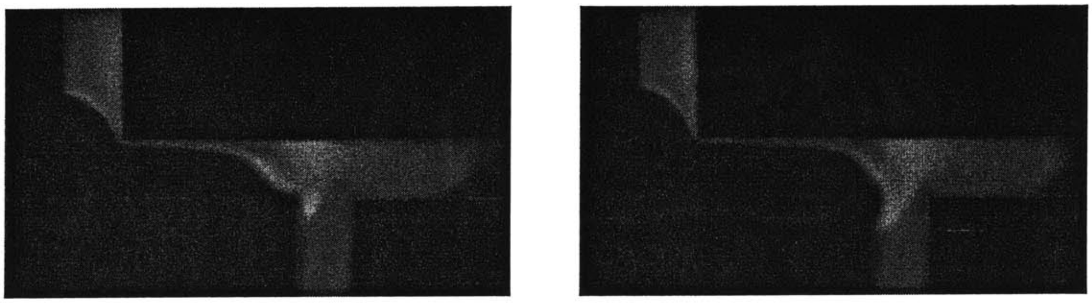

Figure 28. Video Microscopy Images
Frames shown are at 5/8 second intervals. Every fifth image recorded at 1/8 second intervals is shown. The conditions of these images were: type of sample = 500b ssDNA, applied voltage = 250 V, field = 21 V/cm, injector offset = 350 μm, channel width = 90 μm and depth = 45 μm. The sample had been introduced from the upper left arm, and the other small arm is the waste arm. The sample is injected from the injector to the right. Experimental data provided by Vazquez [5]. Name of data file - m05310250cc.

The speed of the stacking peak can be measured easily from proper analysis of the images. The speed of the stacking peak is important because it corresponds to the speed of the moving boundary. This parameter thus is an important link between theory and experimental data.

The images from Openlab® format were saved in a TIFF format to maintain image quality with each step of processing. For a detailed study of the evolution of the concentration profiles at each step, these files were pre-processed using Photoshop. The pre-processing included three steps, wherever necessary. The first step was to rotate the images to make the length of the channel parallel to the horizontal axis. This amount of rotation required varied from approximately 2 to 30 degrees. Next, the images were inverted to show the injector in the conventional configuration where the sample enters the injector from the top, the waste is at the lower part of the injector, and the sample is transported to the right during sample injection. In the third pre-processing step, the image was cropped to maintain a rectangular image. The pre-processed image files were opened with NIH Image software. A narrow strip of the domain along the center line of the channels was selected, and the intensity data along this region was saved. This data was plotted using Matlab®. These plots are shown in Figure 28 for analysis of profiles.

The following information has been extracted from the experimental data – (a) the speed of the sample peak as it moves through the injector, (b) ratio of sample peak concentration to initial sample concentration, and (c) width of the peak. An example of image data file is shown Figure 28. More experimental data is available under CD1 in Appendix 3.

Moving Boundary Velocity

The moving boundary velocity speed was evaluated by the following method. The images were opened with Volocity® and displayed on the computer in an array format. The position of the sample was observed in each image.

The sample was initially along the length of the injector. The physical marker to identify position in these figures was the channel boundary. The channel width was approximately 90 μm. The offset between the sample arm and the waste arm was known. Taking advantage of these markers, the wave of stacking was tracked from the first inner corner of the injector to the next inner corner. The distance traveled by the wave between these two markers was the difference between the injector offset and the channel width. The time taken for the wave to travel this distance was estimated from the difference between the number of frames between the images with the wave at the two extremes and the time lapse between individual frames. It is known that the frame rate for image capturing was maintained at a constant rate of 8 frames/second.

It was seen that the speed of the wave increased monotonically with applied voltage. At higher voltages, because the waves propagated faster, there were fewer images of the wave between the markers. As a result, there were instances when there were no frames with the wave at the markers. In such cases, an estimate was made of the time it would have arrived, based on interpolation from the nearest neighbors.

The following parameters were varied in the study of wave speed: the applied electric field, the injector size, and the constitution of the sample with respect to single size (500 base single stranded) DNA and a sequencing reaction mixture consisting of DNA from 40 bases to 7800 bases in length. The sequencing reaction products were purified by either spin column or by ethanol precipitation. The analysis of individual sets of data, detailed in Table 3, are shown in Figure 29, Figure 30, Figure 31, Figure 32, Figure 33 and Figure 34. The speed of the waves is shown as a function of the applied electric field. These analyses show the wave speed varying for an electric field of 100 V/cm varying from 130 μm/s to 278 μm/s. Linear regression plots are also shown. The speed of the stacking wave is proportional to the applied electric field. The average of all the cases shows that a 100 V/cm applied field will cause the wave to move at 166 μm/s, as shown in Figure 35.

Table 3. Data Sets Analyzed for Speed of Moving Boundary

Data Set	Sample type	Injector Offset	Voltage Range
CD 1	500 b DNA	350 μm	250-1750 V
CD 3	Sequencing Mix	350 μm	500-1500 V
CD 4	Sequencing Mix	350 μm	2000-9000 V
CD 5	Sequencing Mix	250 μm	3000-9000 V
CD 11	Sequencing Mix	500 μm	1000-1750 V
CD 13	Sequencing Mix	350 μm	1000-1750 V

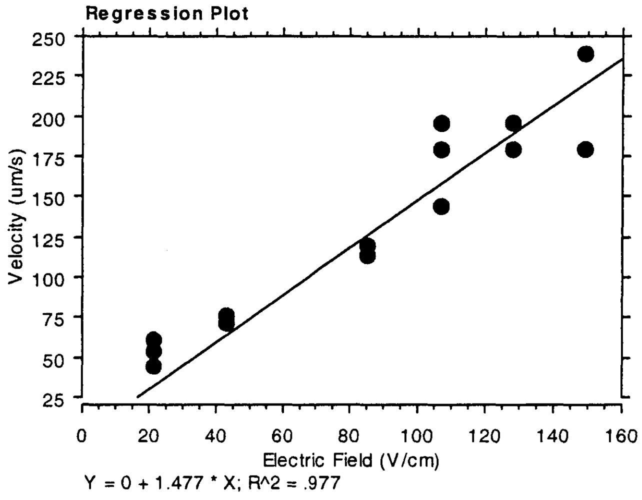

Figure 29. Stacking Wave Speed Vs. Applied Electric Field for 500 b DNA (a)

Data used is from CD1 dated 05/31/2000. The sample is 500 base monodisperse DNA. The regression plot indicates that the a 100 V/cm applied field results in the stacking wave propagating at a speed of 147 μm/s.

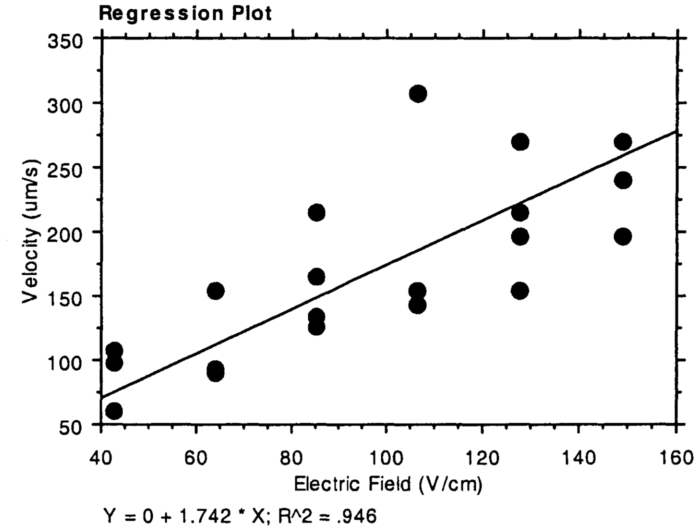

Figure 30. Stacking Wave Speed Vs. Applied Electric Field for 500 b DNA (b)

Data used is from CD3 dated 7/13/2000. The sample is a sequencing reaction product (40-7800 base long DNA). The regression plot indicates that a 100 V/cm applied field results in the stacking wave propagating at a speed of 174 μm/s.

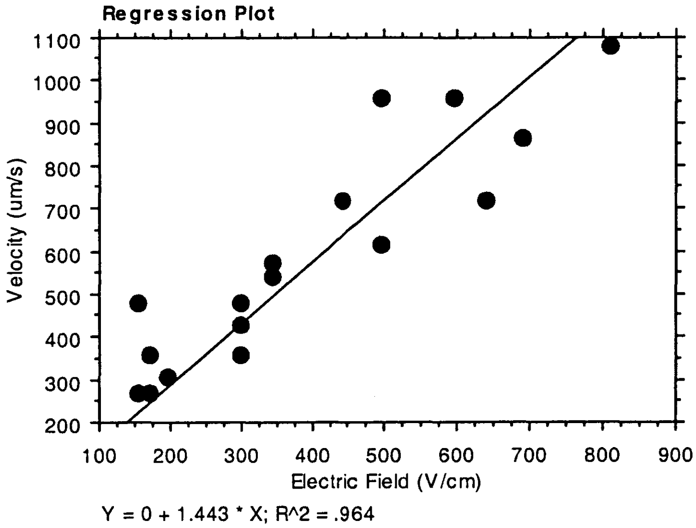

Figure 31. Stacking Wave Speed Vs. Applied Electric Field for Ethanol Precipitated DNA Mixture

Data used is from CD4 dated 2/28/2001. The sample is a sequencing reaction product (40-7800 base long DNA). The sample has been purified using ethanol precipitation. The regression plot indicates that the a 100 V/cm applied field results in the stacking wave propagating at a speed of 144 μm/s.

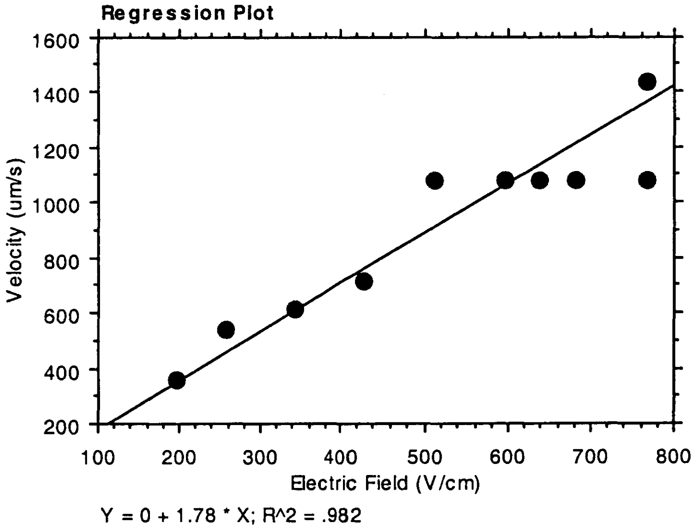

Figure 32. Stacking Wave Speed Vs. Applied Electric Field for Spin Column Purified DNA Mixture

Data used is from CD5 dated 3/20/2001. The sample is a sequencing reaction product (40-7800 base long DNA). The sample has been purified using spin column. The regression plot indicates that the a 100 V/cm applied field results in the stacking wave propagating at a speed of 178 μm/s.

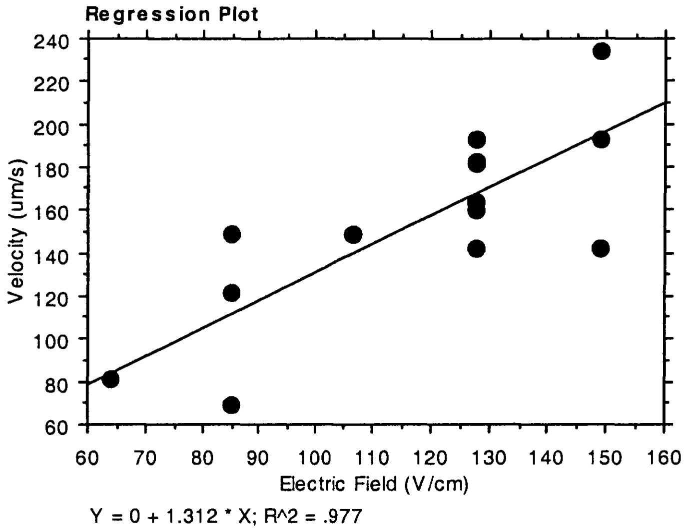

Figure 33. Stacking Wave Speed Vs. Applied Electric Field for DNA Mixture
Data used is from CD11 dated 8/3/2000. The sample is a sequencing reaction product (40-7800 base long DNA). The regression plot indicates that the a 100 V/cm applied field results in the stacking wave propagating at a speed of 131 μm/s.

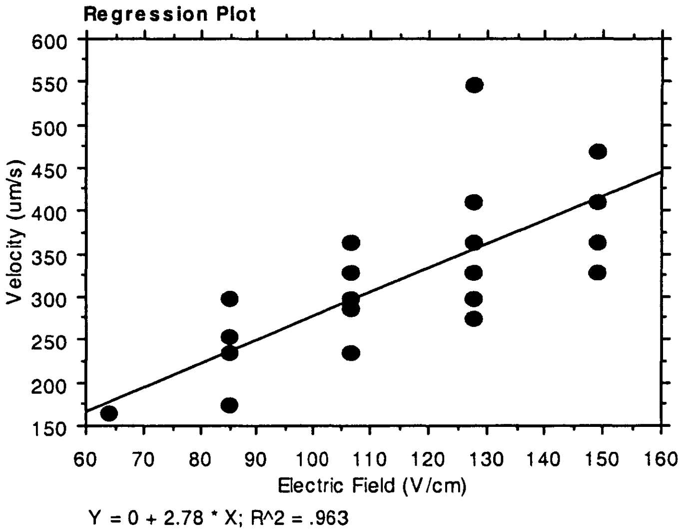

Figure 34. Stacking Wave Speed Vs. Applied Electric Field for DNA Mixture
Data used is from CD13 dated 7/20/2000. The sample is a sequencing reaction product (40-7800 base long DNA). The regression plot indicates that the a 100 V/cm applied field results in the stacking wave propagating at a speed of 278 μm/s.

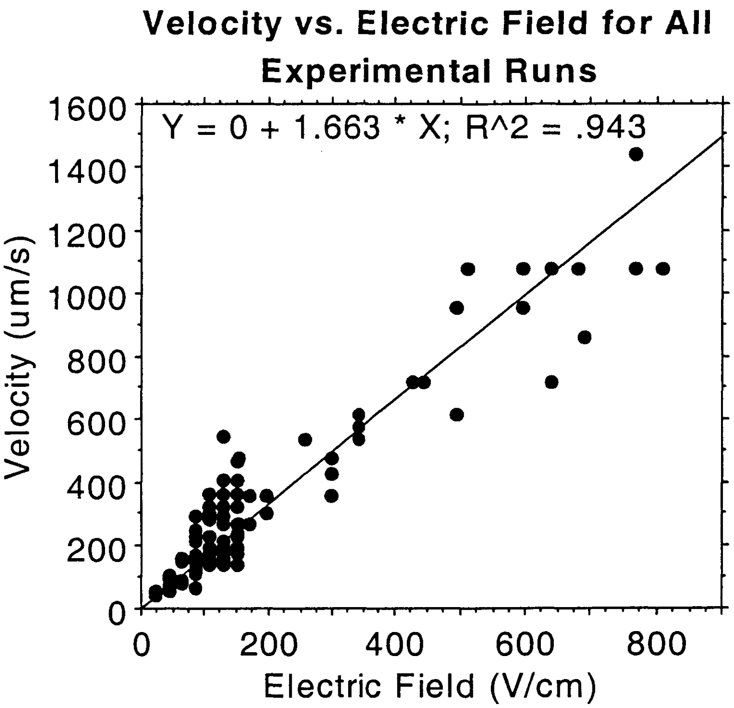

Figure 35. Composite of Stacking Wave Speed Vs. Applied Electric Field
The results from individual cases are combined as one. Regression analysis shows that the expected speed of wave propagation under these conditions for a 100 V/cm applied field is 166 μm/s for the conditions used in all the experiments.

A combined analysis of all the above data was used to obtain the expected speed of the wave. The expected speed of the stacking wave for the combined case is 166 μm/s. This speed was used in developing the model for numerical simulations. The variations in the speed are probably due to differences in the salt composition in the sample. Although the results indicate variation by a factor of two, it could be due to higher salt concentration by evaporation from a sample droplet and dilution by water in the sample chamber after a wash cycle.

Time Evolution of the Concentration Profile

The profiles of concentration of the DNA sample along the center of the injector were obtained and plotted using Matlab®. The results of different cases are presented below.

Figure 36 shows the concentration profiles of 500b DNA sample in a micro-fabricated device with 350 μm injector offset and electric fields ranging from 20 V/cm to 150 V/cm. Each frame is 1/8 second or 125 ms apart from the next, however, the profiles shown are in steps of 5 frames. For example, in the case of **21 V/cm** frames 1-46 means frames 1, 6, 11, 16, 21, 26, 31, 36, 41, 46 or t = 0, 0.625, 1.25, 1.875, 2.5, 3.125, 3.75, 4.375, 5, 5.625. In the other cases, the data as follows: (a) **21 V/cm** (frames 1 - 46) , (b) **42 V/cm** (frames 31 - 46), (c) **85 V/cm** (frames 1- 26), (d) **105 V/cm** (frames 1- 16), (e) **127 V/cm** (frames 1 – 21). (f) **150 V/cm** (frames 1 – 21). In the case of E = 85 V/cm, the data had a higher overall value, probably due to a change in the signal amplification, so it was rescaled to follow similar un stacked concentration as the rest. Stacking ratio increased with increase in applied voltage. This indicates the mechanism of sample self stacking. The sample is constrained in the moving boundary, the width of which decreases with an increase in applied voltage. That the stacking of the sample

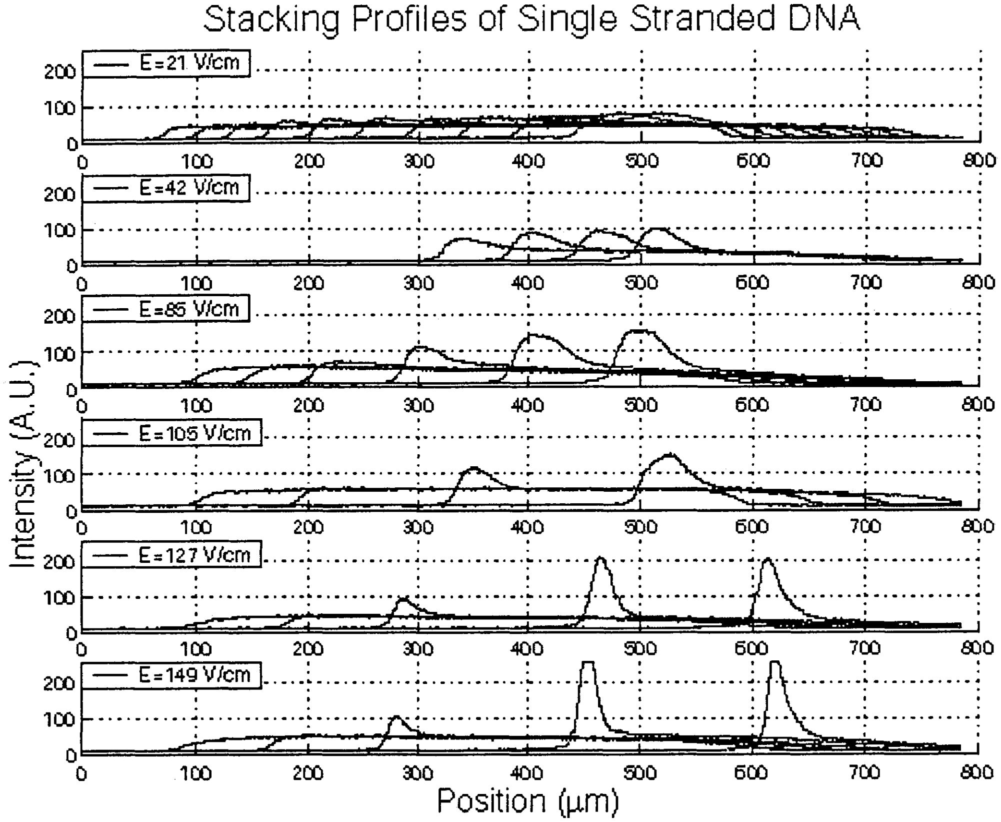

Figure 36. Stacking Profile during Stacking of 500 base Single Stranded DNA
Each frame is 1/8 second or 125 ms apart from the next, however, the profiles shown are in steps of 5 frames. The injector offset was 350 μm here.

increases as the applied field is increased corresponds to the case of sample stacking for samples with mobilities greater than or equal to that of the buffer co-ion. Another observation from these plots is that stacking increases as the wave progresses through the injector.

Figure 37 shows the concentration profiles of a sequencing reaction product of DNA sample in a micro-fabricated device with a 350 µm injector offset and electric fields ranging from 43 V/cm to 150 V/cm. The profiles shown are in steps of 5 frames, each frame at 1/8 second steps. The sample was purified after the sequencing reactions using spin column purification. The subplots are shown for (a) **43 V/cm** (frames 1 - 51), (b) **64 V/cm** (frames 1 - 46), (c) **85 V/cm** (frames 1 - 31), (d) **105 V/cm** (frames 1-26), (e) **128 V/cm** (frames 16-21) and (f) **149 V/cm** (frames 1-21).

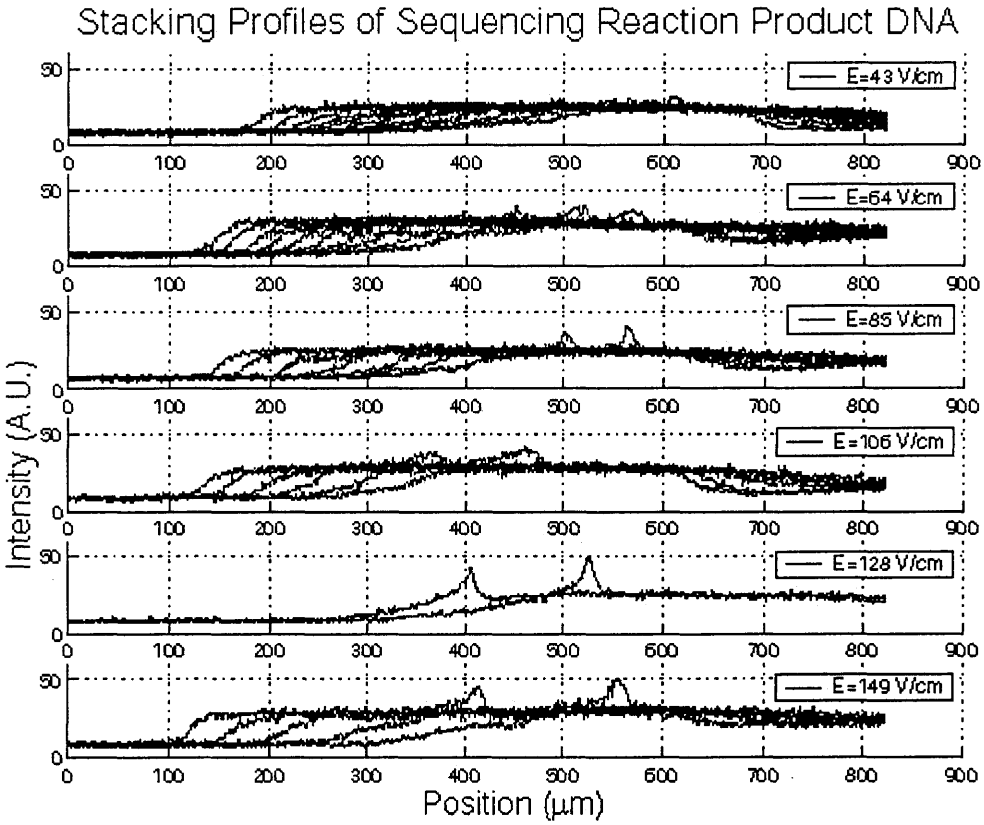

Figure 37. Stacking Profile during Stacking of a Sequencing Reaction Product of a Single Stranded DNA 40-7800 Bases Long
The profiles shown are in steps of 5 frames, each frame at 1/8 second steps. The injector offset was 350 µm here.

In this case of a DNA mixture obtained from Sanger's sequencing reactions, it is seen that there is relatively little stacking in most of the sample region, which remains so with the application of a higher electric field. However, there is a small peak that is formed which grows higher with the application of an electric field. This is because the mixture consists largely of longer fragments of DNA with very low mobility and therefore low stacking. A small fraction of the sample that is faster than TAPS$^-$, the buffer co-ion, undergoes stacking similar to the case demonstrated by the 500b DNA. The net result is due to the slow DNA which hardly stacks and some fast DNA which stacks sharply.

Figure 38 shows the concentration profiles of a sequencing reaction product of DNA sample in a micro-fabricated device with a 250 μm injector offset and electric fields ranging from 213 V/cm to 596 V/cm. The profiles shown are in steps of **2** frames, each frame at 1/8 second steps (except for the $E = 298$ case, which shows every frame). The sample was purified after sequencing reactions using spin column purification. Cases shown are for (a) **213 V/cm** (frames 2-10), (b) **298 V/cm** (frames 2-9), (c) **426 V/cm** (frames 2-10), (d) **511 V/cm** (frames 39-47), (e) **596 V/cm** (frames 20-26).

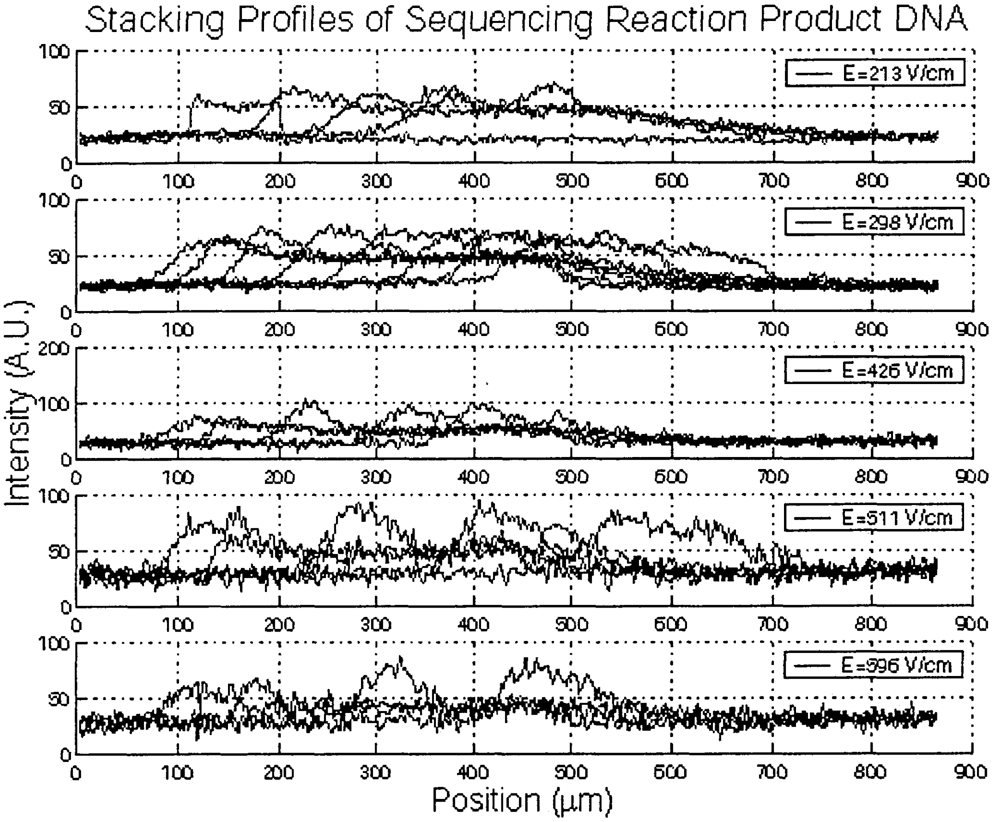

Figure 38. High Voltage Stacking of a Sequencing Reaction Product with Spin Column Purification

The profiles shown are in steps of **2** frames, each frame at 1/8 second steps (except for the *E* = 298 case, which show every frame). The injector offset was 250 μm here.

Figure 39 shows the concentration profiles of a sequencing reaction product of DNA sample in a micro-fabricated device with a 250 μm injector offset and electric fields ranging from 213 V/cm to 596 V/cm. The profiles shown are not in regular steps of frames, each frame at 1/8 second steps. The sample was purified after sequencing reactions using ethanol precipitation. The data from the cases was as follows: (a) **213 V/cm** (frames 27, 30, 33, 36, 39), (b) **298 V/cm** (frames 2, 10, 13), (c) **426 V/cm** (frames 36, 39, 42, 45), (d) **511 V/cm** (frames 60, 63, 66), and (e) **596 V/cm** (frames 40, 42, 44, 46).

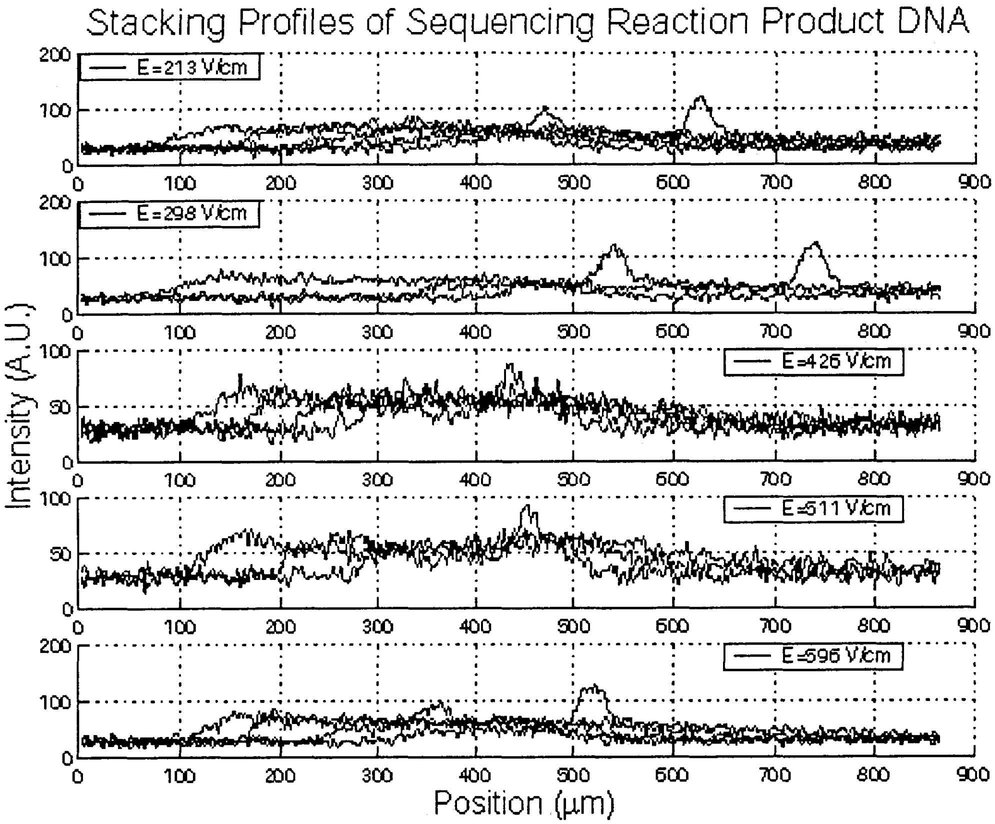

Figure 39 High Voltage Injection of a Sequencing Reaction Product Purified with Ethanol Precipitation

The injector offset was 250 μm.

A comparison of results obtained from spin column and ethanol precipitation shows the following. The distance traversed by the sample wave at equal time intervals is relatively higher for spin column. However, the shape of the sample peak is sharper in the case of the sample purified by ethanol precipitation.

Figure 40 shows the concentration profiles of a sequencing reaction product of DNA sample in a micro-fabricated device with 500 μm injector offset and electric fields ranging from 64 V/cm to 150 V/cm. The profiles shown are in steps of 5 frames, each frame at 1/8 second steps. The data in the cases was as follows: **64 V/cm** (frames 1 - 56), **85 V/cm** (frames 1 - 41), **106 V/cm** (frames 1-36), **128 V/cm** (frames 1-41), and **149 V/cm** (frames 1-26).

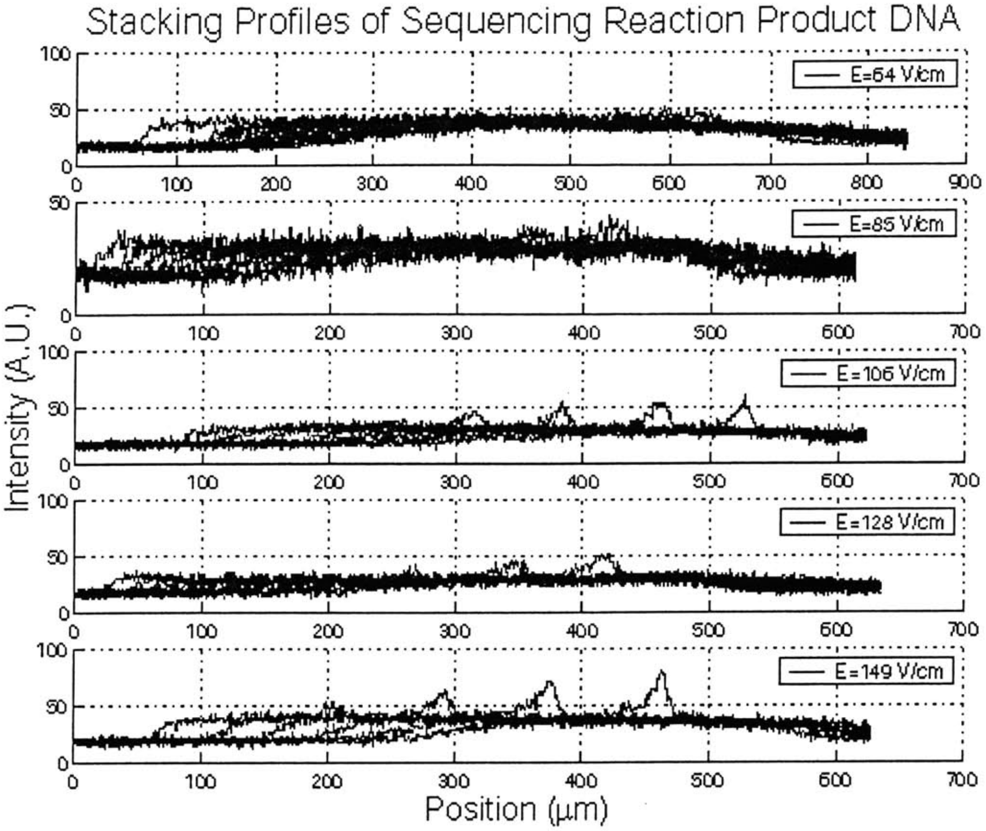

Figure 40. Stacking Profile for a 500 µm Injector Offset
The profiles shown are in steps of 5 frames, each frame at 1/8 second steps. The injector offset was 500 µm here.

Longer injectors cause a greater amount of sample to be swept into the moving boundary, causing higher stacking due to the sample being faster than the buffer co-ion. It should be noted that only the faster DNA contributes to this effect. A higher applied field results in faster and therefore a sharper moving boundary, causing an increase in self stacking

2. Comparing Profiles of Experimental Data with Numerical Results

To compare the experimental data with the numerical results, the following factors were considered: (a) stacking ratio, which is the ratio of the final or peak concentration, (b) the width of peak, and (c) the shape of the peak. This comparison is made for case of (i) 500 b DNA sample and (ii) for the sequencing reaction mixture sample.

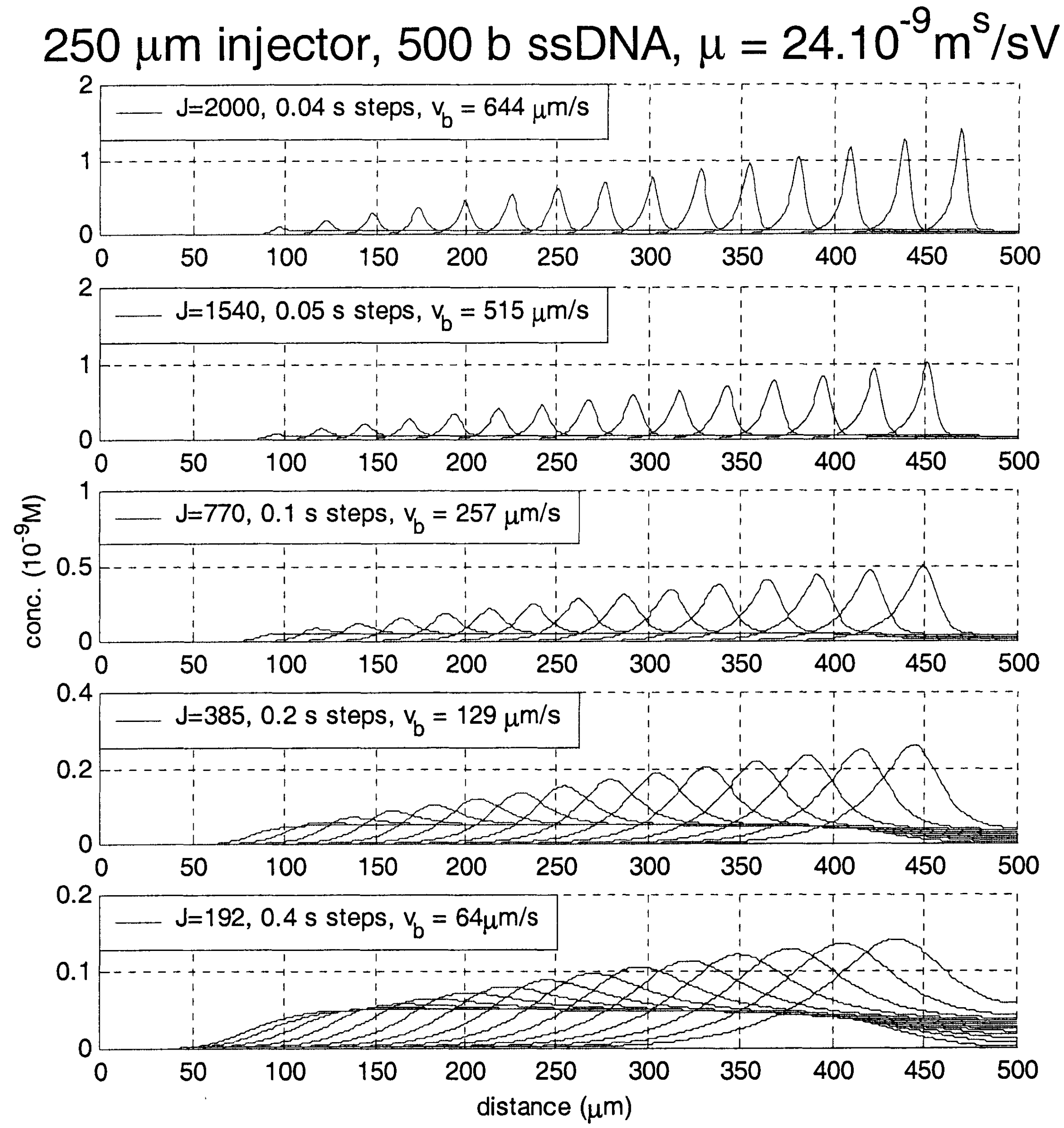

Figure 41. Stacking Profiles for 500 b ssDNA

In Figure 41, the concentration profiles of sample stacking are shown at different time steps. These numerical results show that an increase in the stacking ratio is obtained with an increase in the applied current. In practice, the increased current is due to an increase in the higher voltage applied, so an applied voltage or current are equivalent because any change in the resistance of the separation chamber is negligible due to the electrolyte dynamics. The relation between the current and voltage is $\frac{I}{A} = \sigma \frac{V}{L}$, where I is the current through the separation channel, A is the area of cross section of the channel, σ is the conductivity of the electrolytes in the channel, V is the voltage applied across the channel, and L is the length of the channel.

Discussion

An increase in the applied current or field results in faster movement of the moving boundary. These faster boundaries are also narrower and result in higher stacking for samples with mobility higher than the buffer co-ion. These results are compared with experimental data shown in Figure 36. The stacking ratio with the sample faster than the buffer increases monotonically, an aspect demonstrated in both the numerical and experimental profiles. In both cases, the stacking at approximately 300 μm of travel of the sample peak results in a stacking ratio of 6-7 for a wave speed of about 250 μm/s.

Width of Peak

The width of the peaks obtained from numerical results are shown in the Table 4, which shows reduced width for a higher applied current or voltage.

Table 4. Width of 500 b DNA Sample Peak

Current density (A/m^2)	2000	1540	770	385	192
Width of Peak (μm)	8	10	20	40	80

Shape of Peak

The peaks in the numerical result show a diffusive tail at the rear. In the experimental profiles, the peaks are sharp at the rear but diffuse at the front. Diffusion in the numerical result is introduced from the numerical method, which tends to be diffuse at the tail of a moving wave. The greater sharpness at the front is due to the presence of the sharp moving boundary. In the experimental data, the diffuse front is likely due to the two-dimensional effects of injection. Such features have not been modeled in this one-dimensional case.

3. *Numerical Results for Sample having DNA of Different Mobility*

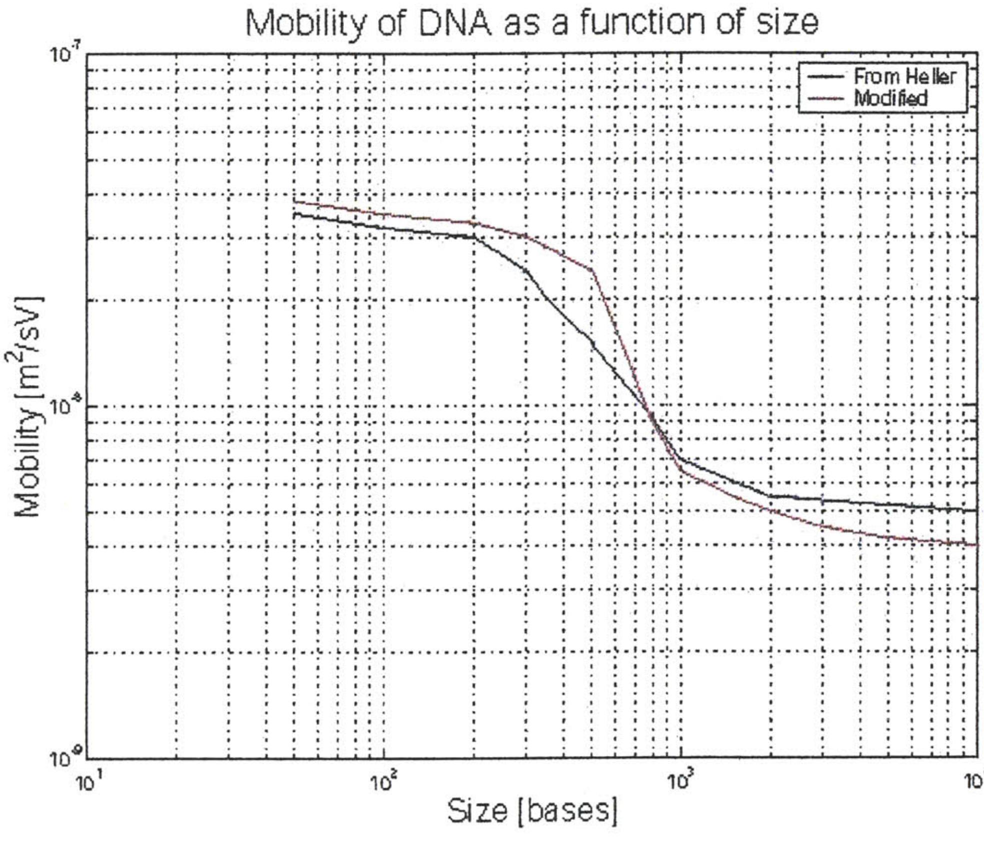

Figure 42. Mobility as a Function of Size
Data from Heller [86] is for ssDNA in 4% pDMA. The modified distribution is from experimental values used in the BioMEMs lab. Mobility of single-stranded DNA in 1X TTE buffer in 2% linear polyacrylamide gel solution. Mobility values obtained in the two plots are similar. It shows three regimes of separation – Ogston sieving on the left, reptation without orientation in the middle and reptation with orientation on the right.

For a sample with a range of DNA sizes, the relation between the size and mobility under the conditions in the microcapillary channels is needed. The sequencing reaction products used in the experiments consisted of DNA fragment lengths from 40b to 7800b in the sample. The mobility of DNA in a 2% linear polyacrylamide gel solution is estimated from known BioMEMs lab data and interpolated similar to the pattern of DNA mobility in related conditions [86] (Figure 42). A few discrete DNA sizes were selected from this curve to represent the complete mixture, with the appropriate weighting. The plot shows three regimes of separation – Ogston sieving on the left, reptation without orientation in the middle and reptation with orientation on the right.

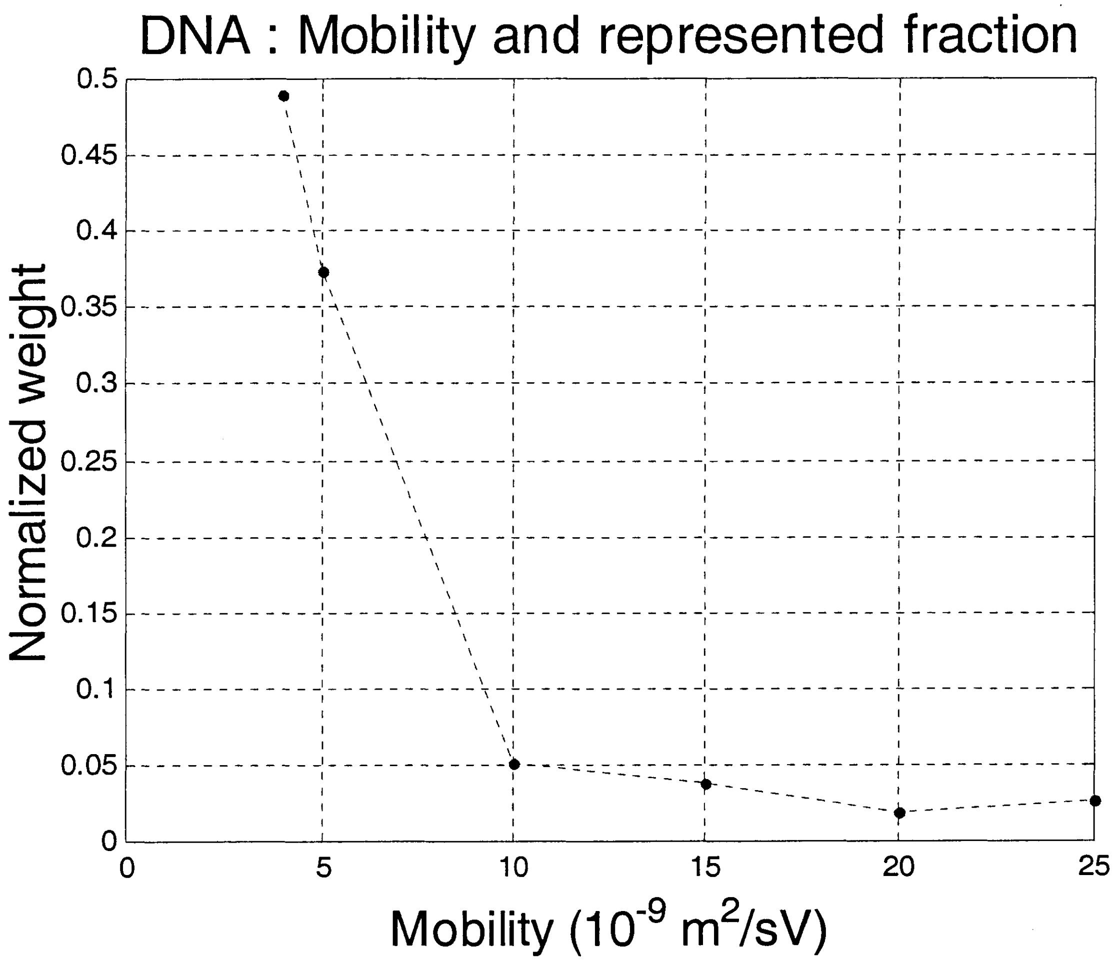

Figure 43. Representative Mobility Values and Density for Numerical Simulations

Having obtained the distribution of mobility as a function of size, the next step is to determine the representative mobility values and the densities of sample those mobility values represent. It is assumed that every size of DNA has an equal probability of existence in the sample due to the nature of chain growth and termination. From this assumption and the data in Figure 42, the representative mobility values and their corresponding density values are obtained (Figure 43).

The weights or density of the mobility values used to represent the complete sample are shown in Table 5. Since each fragment is as likely to exist, the weight of the representative fraction is proportional to the range of DNA it can represent as shown. The weights of the different components are obtained by normalizing with respect to the size range represented, since the size range represents the density of the species (Table 6). This shows that most of the DNA fragments present in the sequencing reaction product are very large, about a few thousand bases, and have relatively low mobility with respect to TAPS$^-$ (21 x 10^{-9} m^2/sV). The smaller, faster DNA strands have a relatively lower fraction in the sample composition. However, their sharp stacking can still reveal a stacking peak, as seen in the experiment.

Table 5. Mobility and Representative Size Ranges

Mobility (10^{-9}m^2/sV)	Size – min	Size – max	Size- range
4	4000	7800	3800
5	1100	4000	2900
10	700	1100	400
15	400	700	300
20	250	400	150
25	50	250	200

Table 6. Mobility and Relative Density of DNA

Mobility	4	5	10	15	20	25
Weight	0.4903	0.3742	0.0516	0.0387	0.0194	0.0258

4. Numerical Simulation of Total DNA in Sample

The results of the simulations for samples with the representative mobility values are shown in Figure 44). The use of samples with the representative mobility values simplifies the problem of simulating sample stacking for every sized DNA to a smaller set of representative DNA constituents. A linear combination of the solutions of the profiles weighted by the density associated with that mobility is the resulting solution for stacking of the total DNA in the sample.

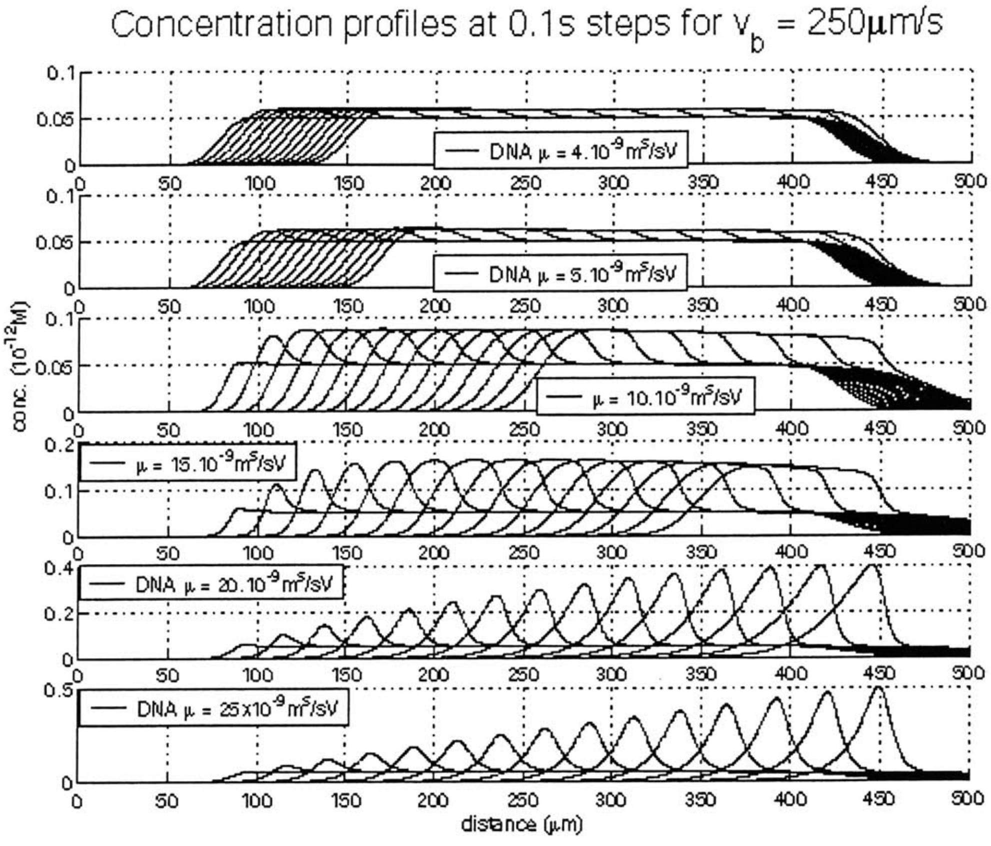

Figure 44. Stacking of Representative Components of a Sample
The first four samples show stacking which shows a fixed amount of stacking throughout. The last two show stacking which increases as it goes across the sample injector.

Figure 44 shows the stacking of samples of different mobility values in a 350 μm sample injector. The stacking ratios for samples slower than the buffer, as shown in the first four cases, were as predicted in Section 3.7. The last two cases show samples faster than the buffer, and hence stacking is much higher and diffusion-limited.

The composite effect of a few representative sizes of DNA fragments with the corresponding weights, is Figure 45. The net stacking achieved after 250 μm of travel is 1.8. The corresponding value of stacking obtained in the experiment is 2.0, a 10% error.

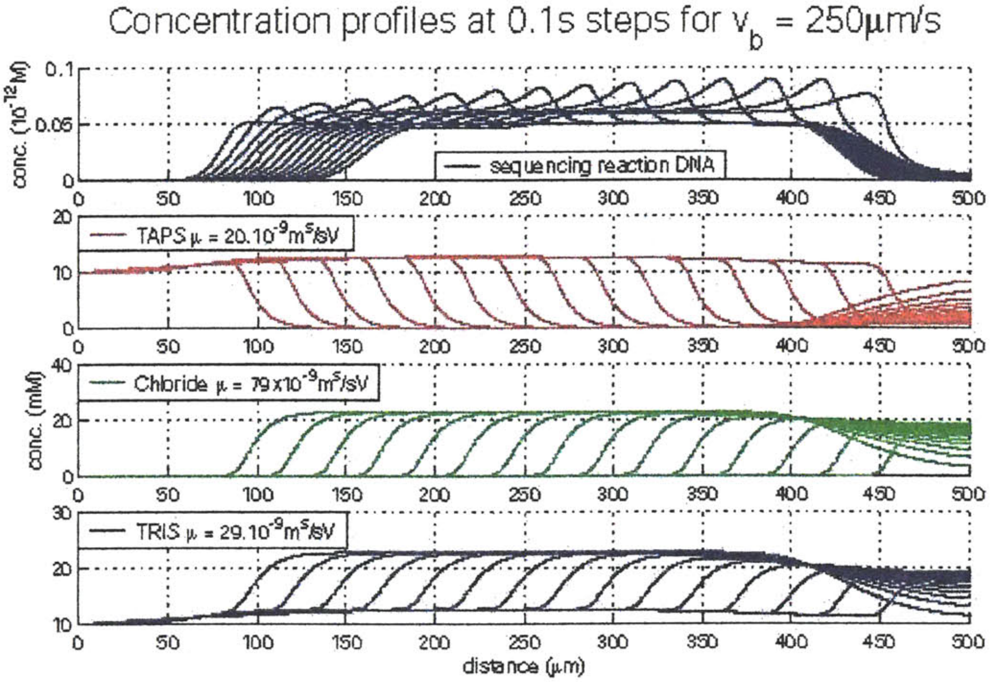

Figure 45. Sequencing Reaction Product DNA Stacking
Sample stacking of a composite mixture of all components represented by a few DNA and weighted by their expected density. Profiles of the sample major component (top), the buffer (TAPS, TRIS), and stacking ions (chloride) are shown.

Comparing Figure 46 with Figure 47, it is seen that an increase in the applied field increases stacking of the sample for cases where the sample mobility is higher than the buffer mobility. The other samples undergo stacking with little effect of the electric field on the stacking ratio. More cases are shown in Appendix 11.

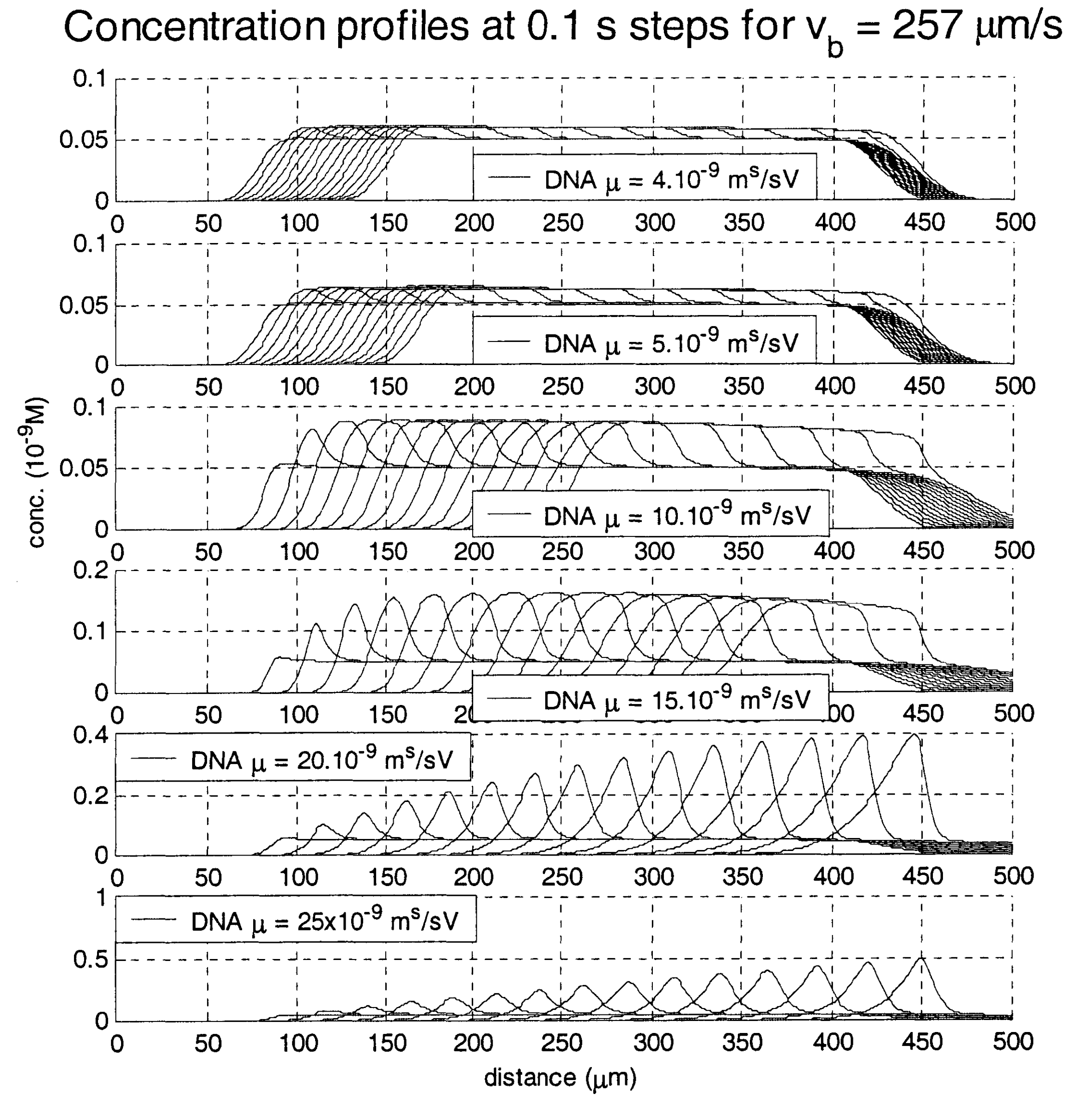

Figure 46. Stacking of Different Components for a Moving Boundary Speed of 257 μm/s

Comparison of Profile and Evolution for Sequencing DNA

The stacking of a composite mixture of DNA, as represented by a discrete set of DNA with specified mobility values as selected earlier and weighted to best represent the mixture, is shown in Figure 48. When these results were compared with the corresponding figures of experimental data (Figure 30), it is evident that for stacking of composite DNA in a 350 μm

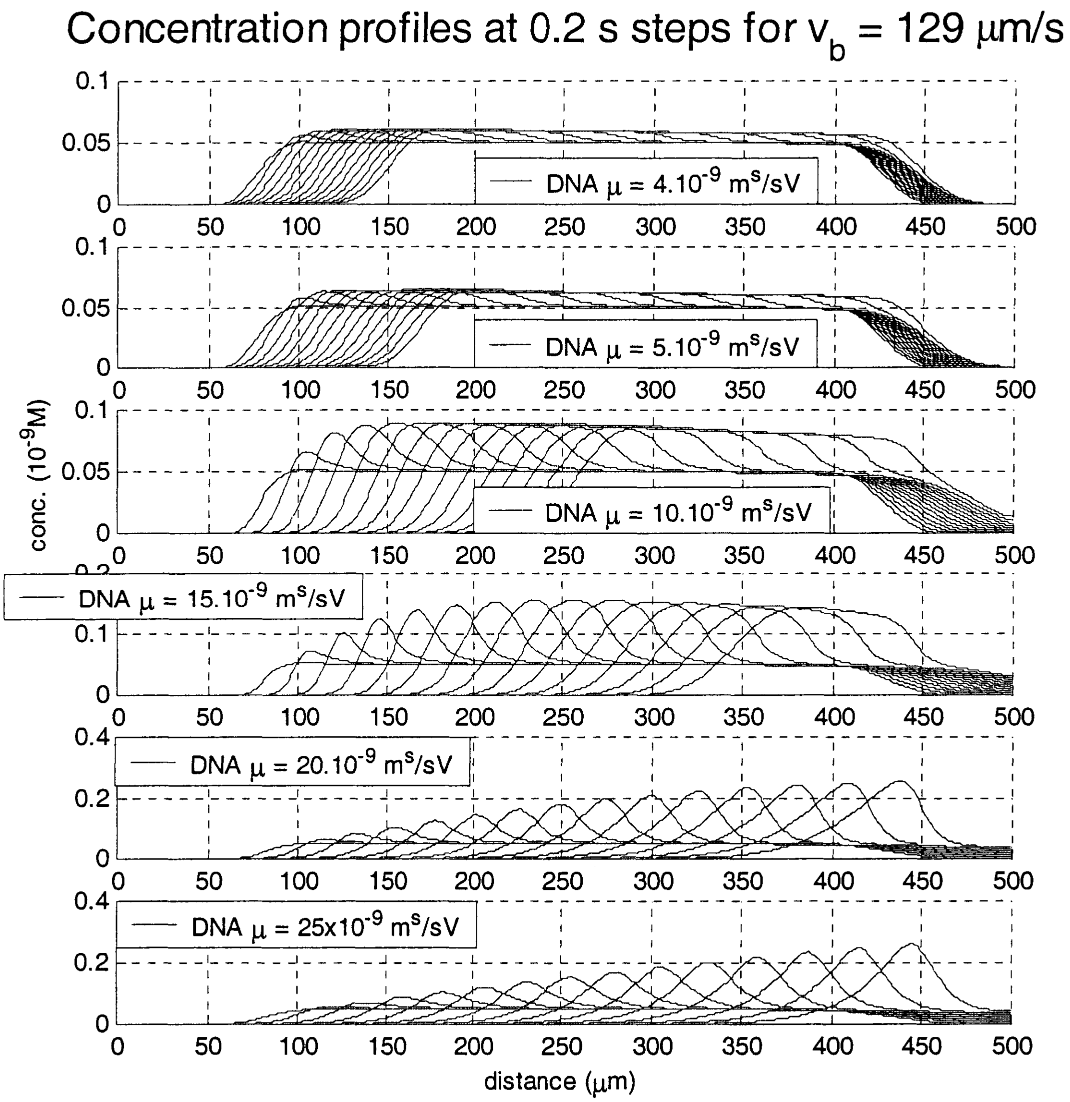

Figure 47. Stacking of Different Components for a Moving Boundary Speed of 129 μm/s

injector at 40 V/cm, 80 V/cm, 150V/cm, 200 V/cm the stacking ratio from the numerical scheme is found to be less than the experimental value by approximately 10%.

The stacking ratio is useful for describing the stacking of samples with mobility values less than buffer co-ion mobility. For faster sample ions, an important metric is the width of the sample peak. This is because the sample peak gets higher due to more sample added from a longer sample injector. In this case, the effect of diffusion is also of importance due to the high concentration gradient from sharp stacking peaks. As a result, the stacking ratio for the faster

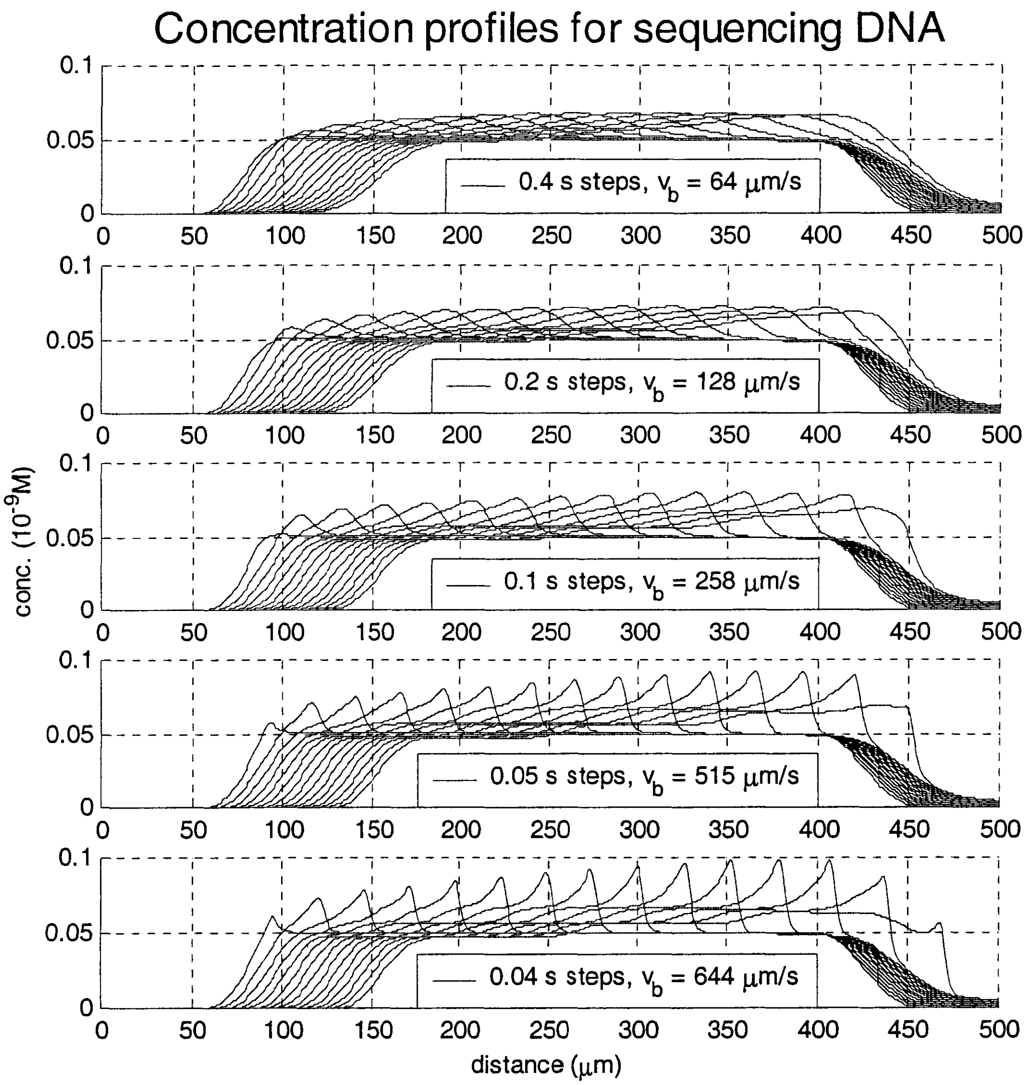

Figure 48. Stacking of Composite DNA for Different Moving Boundary Speeds

ion requires consideration of more factors. The theory for both forms of stacking was developed in Chapter 2.

Discussion

The following effects of parameters on sample stacking have been shown:

Buffer Co-Ion Mobility

For samples with mobility lower than the buffer sample, stacking increases with an increase buffer co-ion mobility because the electric field difference is higher across the boundary. For samples that are faster than the buffer, the higher electric field difference across the boundary causes the boundary to be narrower. The reduced space available to the sample causes it to undergo higher stacking.

Sample Mobility

As sample mobility increases, its stacking ratio increases. This has been explained earlier in Section 2.12. For samples with mobility greater than the mobility of the buffer co-ion but less than the stacking co-ion, which in this case is chloride, the stacking follows a form which is independent of the mobility, neglecting diffusion.

Higher Injection Voltage

For a sample is slower than the buffer, the stacking is unaffected by the high injection voltage. In the case of sample mobility higher than the buffer ion mobility, the stacking achieved depends upon the width of the boundary. The width of the boundary is determined by the balance between diffusive effects and the boundary speed. A higher boundary speed causes the boundary to get narrower. The boundary speed increases with the applied voltage. Hence, a higher injection voltage causes a narrower boundary and therefore higher stacking of sample which is faster than the buffer. The principle was described in Chapter 2.

The concentration profile of DNA samples of different mobility and their evolution are the result of the action of the same electric field on different samples. Figure 46 and Figure 47 show the stacking of samples with mobility $4\text{x}10^{-9}\text{m}^2/\text{sV}$, $5\text{x}10^{-9}\text{m}^2/\text{sV}$, $10\text{x}10^{-9}\text{m}^2/\text{sV}$, and $15\text{x}10^{-9}\text{m}^2/\text{sV}$. The stacking ratios for these are 1.15, 1.2, 1.7, and 3.2, respectively, and they compare very well with theory. Also shown are stacking of samples with mobility equal to or greater than the buffer co-ion (TAPS). For sample mobility values of $20\text{x}10^{-9}\ \text{m}^2/\text{sV}$ and $25\text{x}10^{-9}\ \text{m}^2/\text{sV}$, the stacking ratios at 250 μm of travel were 6.6 and 6.5, respectively. The samples continue to get stacked in this mode as the moving boundary moves through the sample zone. These ratios are reasonably close to the experimental stacking of 500b DNA obtained in the experiments.

5. Evaluation of Numerical Model

Based on the comparison of numerical results and experimental results the following observations may be made.

The agreement of speeds is good at lower injection voltages. The predictability of effects at higher voltages is not so reliable, probably due to thermal effects. Higher temperatures across the width of the channel result in loss of sharpness of the peak. The reduced predictive power at higher voltages is due to unmodeled thermal effects.

The shape of the sample stacking peak shows some deviations from the experimental data. The shape of the peak shows a longer tail in the simulation, whereas in the experiment it is relatively sharp. The tail at the rear is due to numerical diffusion. The sample is not constrained in the boundary but lags behind.

The shape as observed from the experimental data has a diffuse front and a sharp rear. This indicates the sample is faster than the buffer as shown in a review of sample stacking by Beckers and Bocek [90]. The departure of the predicted shape from the observed shape could result from the following reasons. (a) They could be numerical artifacts. Since the stacking of fast sample shows sharpness in one direction but not the other, it lends credence to the notion that there are other factors. Some other possible reasons are listed. (b) It could be due to two-dimensional effects during sample loading at the injector. (c) Finally, it could be the result of pH changes which cause changes in conductivity. Such an analysis would require modification of the governing equations for the problem. Generation and reaction terms should be incorporated to verify their effect.

Another factor that could affect this experiment is that the high voltage switch used to apply the voltage was designed for lower voltages, and the breakdown of the gas due to sparks has been reported. Uncertainty in the applied electric field values could also be the source for the reduced predictive power under these conditions.

6. Application of Model for Injector Length Design

Given a specification of sample mobility and desired separation quality using a separation chamber of a particular length, the selection of the injector length is quite important. Some terms are first defined. Plate number is the square of the ratio of the distance traveled by the sample plug to the spread of a spike of sample defined by its standard deviation as it moves after injection to the end of the channel [91]. Resolution is a measure of how well two neighboring peaks can be distinguished. The definition of resolution [8] is

$$R = \frac{d_{peak}}{W_{mean}} . \tag{4.1}$$

Assuming normal distributions, the full-width at half maximum is $hw = \sqrt{\frac{\ln 2}{2}} W = 0.59W$.

When $R = 0.5$, it implies that the width of two peaks is just as much as the width at half-maximum.

Method

The following experimental data was used from a 40 cm microfabricated electrophoretic device. Fragments of 800 base long single stranded DNA (ssDNA) separated in the channel reached the detector at the end in 43 minutes. The speed of 800b-ssDNA was therefore 40 cm/43 min. = 155 μm/s. It is also known that a 7.5 kV voltage is applied across the 40 cm length. Assuming a uniform electric field in the length of the channel, the electric field in the channel is calculated as 187.5 V/cm. The mobility of the 800b-ssDNA is then obtained as 155×10^{-6} m/s/187.5×10^{2} V/m = 8.3×10^{-9} m^2/sV.

Measurements taken from the electropherogram indicate that the width between consecutive peaks was 5.5 sampled data points. This is converted to a length by the use of the data sampling speed and the speed of the fragments. Width of the sample plug is the product of the speed of the sample, the number of data points, and the time between data points = 155 μm/s x (5.5)/3=284 μm.

Resolution estimates at this region show that R = 0.25 approximately. This means that the standard deviation of the peak is equal to the separation between adjacent peaks or $\sigma = \delta$, where σ is the standard deviation of the sample peak and δ is the distance between adjacent peaks. The injector offset is 500 μm, the channel width is 90 μm, and it is assumed that the increase in width due to diffusion is 90 μm. The width of the sample plug is therefore 680 μm. The variance due to diffusion is $\sigma^2 = 2Dt$=2 (0.5x10^{-11}) 2580 and the standard deviation is $\sigma_{diff} = 160$ μm. Similarly, the standard deviations due to the detector width and thermal effects are 50 μm each. The following values are used: $\sigma_{inj} = 197$ μm , $\sigma_{diff} = 160$ μm , $\sigma_{\text{detector}} = 50$ μm , $\sigma_{thermal} = 50$ μm . Adding the variances, $\sigma^2 = \sigma_{inj}^2 + \sigma_{inj}^2 + \sigma_{detector}^2 + \sigma_{thermal}^2$, the net standard variation obtained is $\sigma = 262$ μm . This is less than the value obtained by the electropherogram, thus indicating other unmodeled sources of error.

The questions that are now addressed include the following. What should be the width of the sample at the detector on a 40 cm device for a resolution of 0.5? What should be the corresponding width of the injector?

In order to obtain a resolution of 0.5, let the injector offset be l_{offset}. For R = 0.5, the width of the peak should be twice the distance between peaks, so the standard deviation of the Gaussian peak for this case should be 142 μm. Set $\frac{(l_{offset} + 180)^2}{12} + 160^2 + 50^2 + 50^2 = 142^2$. The solution to this equation does not yield a positive injector offset. For these conditions of device length, diffusion and selectivity, the separation of R = 0.5 for 800b does not seem possible when sample stacking is not considered in the modeling process. If sample stacking is considered, the sample from the injector collapses into a smaller length, and so the injector length can be estimated again. Sample stacking is possible with the use of the proper buffers, and a careful selection of their concentration can cause sample stacking without a corresponding decrease of concentration as the sample proceeds toward separation.

Based on the stacking model, the initial sample would be stacked into a plug, such that the stacking ratio of the 800b-ssDNA would be

$$\frac{c_{final}}{c_{initial}} = \frac{E_2}{E_1} \cdot \frac{\mu_2 - \mu_s}{\mu_1 - \mu_s} = \frac{1}{4} \frac{80 - 8.3}{20 - 8.3} \approx 1.5 .$$

For R = 0.5, $\sigma = 142$ μm. Due to stacking, the standard deviation can be increased by a factor allowed, i.e. $\sigma = 142 \times 1.5$ μm or $\sigma = 213$ μm. Performing calculations:

$$\frac{\left(l_{offset} + 180\right)^2}{12} + 160^2 + 50^2 + 50^2 = 213^2 .$$

This calculation predicts an injector offset of 240 μm for a resolution R = 0.5 with stacking as predicted by the model developed in this thesis. This suggests a significant potential improvement of performance of the micro-devices for DNA electrophoresis, which would not be considered possible with the use of older models. As a result, the model for DNA sample stacking provides a theoretical foundation for extending the capabilities of DNA electrophoresis.

Chapter 5. Conclusion

1. Summary of Results

In this thesis, a quantitative physics-based model for sample stacking has been developed. A numerical model, supported by a theoretical understanding, is a predictive model for sample stacking. This is the first time a such a fundamental understanding of the cause of stacking in DNA sequencing has been demonstrated.

The validation of the model is performed from comparisons with results from real experiments. Two types of DNA sample, a monodisperse 500b DNA sample and one for a mixture of various DNA fragments prepared from sequencing reactions, were used. The use of two different purification methods, ethanol precipitation and spin column purification, was investigated. Sample purification methods yielded results with significant variability so a clear conclusion cannot be made. Although limited parameter variations were performed in the experiments, the model makes strong predictions on the effect of these and other parameters.

This thesis shows the importance of simple electrochemical properties of the sample and buffer and their important impact on the separation quality of electrophoresis. The electrophoresis community has allocated immense resources to exploring ways to improve resolution of DNA sequencing by studying the effects different gels, their concentrations, and the molecular mechanism of DNA electrophoresis. However, as shown in this thesis, a strong understanding can be gained from a treatment of the mechanism of sample stacking based on their electrochemical and electrokinetic properties of the chemical constituents.

2. Process Improvements

The role of the buffer in DNA sample stacking was explored and understood to some degree. Based on the analysis in this thesis, the property of the buffer which should be modified for better stacking is now known. This work could potentially improve separation by the design or selection of a better buffer.

An injector length design method has been developed which takes advantage of the stacking of DNA of different sizes. Given a separation quality requirement and a device length, the injector length can be designed, assuming the buffer and sample concentrations are chosen correctly. This method presents a new way to design the injector length and shows ways to extend the capability of existing devices.

3. Contributions

In this thesis, a new mechanism for sample stacking in DNA electrophoresis was proposed. A numerical model of DNA sample stacking was implemented and the model was verified with existing experimental data. This thesis proposed ways to improve performance of separation of DNA using micro-devices. It includes ways to select buffers that enhance separation quality and presents a way to incorporate stacking to design injector lengths.

This thesis is a step towards more repeatable sample injection. Repeatability of a sample injection has been a problem in electrophoresis of DNA and has not been achieved [86]. The contribution of this thesis improves the understanding of DNA electrophoresis and can potentially enhance the repeatability of sample injection in DNA electrophoresis.

4. Suggestions for Further Work

Experiments of video microscopy, when performed in the future, would benefit from the following modifications.

(1) The measurement of sample and buffer conductivity can help in obtaining more accurate model parameters and predicting performance.

(2) The following parameters should be changed, keeping others constant: (a) buffers and (b) independently measured sample salt concentrations

(3) For studies with higher applied voltage, a higher resolution of imaging should be explored.

(4) Ways to combine imaging of the injector and detection at the end of the separation chamber should be explored to experimentally examine how stacking affects resolution of separation. While a model has been developed in this thesis, a stronger validation from more comprehensive and better quality of measurements would be useful.

(5) A larger field of view of imaging would be meaningful in order to observe stacked sample more down stream from the injector. This would help to capture effects of how the sample profile changes as it separates from the stacking ions. Another way to achieve this would be to move the electrophoresis device under the microscope.

(6) In a work which involves processing many images, including a time stamp in images, using accurate and higher resolution reference features would all help to make the analysis more efficient and reliable. Saving images in portable format would also help in further work.

(7) It is believed that the high voltage power supply used in the study was used for voltages higher than its designed capability. This caused discharges and thermal problems in the supply, reducing the reliability of the data. A better high voltage study might be educational.

(8) It would be useful to have data of experiments with monodisperse samples of DNA. Some suggested sizes are 50b, 100b, and 200b and steps of 100 up to 2000 and steps of 500 up to 8000.

(9) It may also be useful to measure the temperature in the channel center for a more accurate estimation of thermal differences and the consequent loss of resolution from this effect.

References

1. Sanger, F., S. Nicklen, and A.R. Coulson, *DNA sequencing with chain-terminating inhibitors.* Proceedings of the National Academy of Science USA, 1977. **74**(12): p. 5463-5467.
2. Schmalzing, D., et al., *DNA typing in thirty seconds with a microfabricated device.* Proceedings of the National Academy of Science USA, 1997. **94**(September 1997): p. 10273-10278.
3. Beckers, J.L. and P. Bocek, *Sample stacking in capillary zone electrophoresis: Principles, advantages and limitations.* Electrophoresis, 2000. **21**: p. 2747-2767.
4. Chien, R.-L., *Sample Introduction and Stacking*, in *High-performance capillary electrophoresis: theory, techniques and applications*, M.G. Khaledi, Editor. 1998, John Wiley and Sons: New York. p. 449-479.
5. Vazquez, M., *A study of loading parameters that affect DNA Electrophoresis in Microdevices*, in *Mechanical Engineering*. 2001, MIT.
6. Schmalzing, D., et al., *DNA sequencing on microfabricated electrophoretic devices.* Analytical Chemistry, 1998. **70**(11): p. 2303-2310.
7. Chien, R.-L. and D.S. Burgi, *Sample Stacking of an Extremely Large Injection Volume in High-Performance Capillary Electrophoresis.* Analytical Chemistry, 1992. **64**: p. 1046-1050.
8. Luckey, J.A., T.B. Norris, and L.M. Smith, *Analysis of resolution in DNA sequencing by capillary gel electrophoresis.* Journal of Physical Chemistry, 1993. **97**(12): p. 3067-3075.
9. Lax, P. and B. Wendroff, *Systems of Conservation Laws.* Communications in Pure and Applied Mathematics, 1960. **13**(217): p. 217-237.
10. Boris, J.P. and D.L. Book, *Flux-corrected Transport. I. SHASTA, A Fluid Transport Algorithm That Works.* Journal of Computational Physics, 1973. **11**: p. 38-69.
11. Yakushevich, L.V., *Nonlinear Physics of DNA.* Wiley series in nonlinear science, ed. A.H. Nayfeh. 1998, Chichester, UK: John Wiley & Sons Ltd.

12. Maniatis, T., E.F. Fritsch, and J. Sambrook, *Molecular Cloning: A Laboratory Manual.* 1982, Cold Spring Harbor, NY: Cold Spring Harbor Laboratory.
13. Manz, A., et al., *Planar Chips Technology for Miniaturization and Integration of Separation Techniques into Monitoring Systems - Capillary Electrophoresis on a Chip.* Journal of Chromatography, 1992. **593**: p. 253-258.
14. Rice, C.L. and R. Whitehead, *Electrokinetic Flow in a Narrow Cylindrical Capillary.* The Journal of Physical Chemistry, 1965. **69**(11): p. 4017-4023.
15. Hjerten, S., *High-Performance Electrophoresis - Elimination of Electroendosmosis and Solute Adsorption.* Journal of Chromatography, 1985. **347**(2): p. 191-198.
16. Carrilho, E., et al., *Rapid DNA sequencing of more than 1000 bases per run by capillary electrophoresis using replaceable linear polyacrylamide solutions.* Analytical Chemistry, 1996. **68**(19): p. 3305-3313.
17. Smith, L.M., et al., *Fluorescence detection in automated DNA sequencing analysis.* Nature, 1986. **321**: p. 674-679.
18. Ju, J.Y., A.N. Glazer, and R.A. Mathies, *Energy transfer primers: A new fluorescence labeling paradigm for DNA sequencing and analysis.* NAT MED, 1996. **2**(2): p. 246-249.
19. Biosystems, A., *ABI Prism BigDye Terminator v 3.0 Cycle Sequencing Kits.* 2001. p. 1-4.
20. Giddings, M.C., et al., Genome Research, 1998. **8**: p. 644-665.
21. Collins, F.S., M.S. Guyer, and A. Chakravarti, *Variations on a Theme: Cataloging Human DNA Sequence Variation.* Science, 1997. **278**(5343): p. 1580-1581.
22. FBI, *The FBI's Combined DNA Index System Program.* 2000, FBI Forensic Science Systems Unit.
23. Tiselius, A., *A new apparatus for electrophoretic analysis of colloidal mixtures.* Transactions of the Faraday Society, 1937. **33**: p. 524-531.
24. Jorgenson, J.W. and K.D. Lukacs, *Capillary Zone Electrophoresis.* Science, 1983. **222**(4621): p. 266-272.
25. Paegel, B.M., et al., *High throughput DNA sequencing with a microfabricated 96-lane capillary array electrophoresis bioprocessor.* Proceeding of the National Academy of Science USA, 2002. **99**(2): p. 574-579.
26. Connell, C., et al., Biotechniques, 1987. **5**: p. 342-348.

27. Brumbaugh, J.A., et al., Proceeding of the National Academy of Science USA, 1988. **85**: p. 5610-5614.
28. Kambara, H., et al., BioTechnology, 1988. **6**: p. 816-821.
29. Freeman, M., C. Baehler, and S. Spotts, Biotechniques, 1990. **8**: p. 147-148.
30. Wilson, R.K., et al., *Automation of Dideoxynucleotide DNA sequencing reactions using a robotic workstation.* BIOTECHNIQUES, 1988. **6**(8): p. 776.
31. Landegren, U., et al., *DNA Diagnostics - Molecular Techniques and Automation.* Science, 1988. **242**: p. 229-237.
32. Venter, J.C., *The sequence of the human genome.* Science, 2001. **291**(5501): p. 1304.
33. Vazquez, M., et al., *Electrophoretic injection within microdevices.* Analytical Chemistry, 2002. **74**: p. 1952-1961.
34. Gebauer, P., W. Thormann, and P. Bocek, *Sample self-stacking in zone electrophoresis Theoretical description of the zone electrophoretic separation of minor compounds in the presence of bulk amounts of a sample component with high mobility and like charge.* Journal of Chromatography, 1992. **608**: p. 47-57.
35. Gebauer, P., W. Thormann, and P. Bocek, *Sample self-stacking and sample stacking in zone electrophoresis with major sample components of like charge: General model and scheme of possible modes.* Electrophoresis, 1995. **16**: p. 2039-2050.
36. Viovy, J.-L., *Electrophoresis of DNA and other polyelectrolytes: Physical mechanisms.* Reviews of Modern Physics, 2000. **3**(July): p. 813-872.
37. Maxam and Gilbert, 1977.
38. Lerman, L.S. and H.L. Frisch, *Why Does the Electrophoretic Mobility of DNA in Gels Vary with the length og the Molecule?* Biopolymers, 1982. **21**: p. 995-997.
39. Lumpkin, O.J. and B.H. Zimm, *Mobility of DNA in Gel Electrophoresis.* Biopolymers, 1982. **21**: p. 2315-2316.
40. Bier, M., et al., *Electrophoresis: Mathematical Modeling and Computer Simulation.* Science, 1983. **219**(4590): p. 1281-1287.
41. Brouwer, G. and G.A. Postema, *Theory of the separtion in displacement electrophoresis.* Journal of the Electrochemical Society, 1970. **117**(7): p. 874-878.

42. Kohlrausch, v.F., *Ueber Concentrations-Verschiebungen durch Electrolyse im Inneren vvon Losungen und Losungsgemischen.* Annalen der Physik und Chemie, 1897. **62**: p. 209-239.

43. Mikkers, F.E.P., F.M. Everaerts, and T.P.E.M. Verheggen, Journal of Chromatography, 1979. **169**: p. 11-21.

44. Foret, F., E. Szoko, and B.L. Karger, *On-column transient and coupled column isotachophoretic preconcentration of protein samples in capillart zone electrophoresis.* Journal of Chromatography, 1992. **608**: p. 3-12.

45. Krivankova, L., et al., *Options in electrolyte systems for on-line combined capillary isotachophoresis and capillary zone electrophoresis.* Journal of Chromatography, 1993. **638**: p. 119-135.

46. Quirino, J.P. and S. Terabe, *Exceeding 5000-Fold Concentration of Dilute Analytes in Micellar Electrokinetic Chromatography.* Science, 1998. **282**(16 October): p. 465-468.

47. Fife, P.C., O.A. Palusinski, and Y. Su, *Electrophoretic Traveling Waves.* Transactions of the American Mathematical Society, 1988. **310**(2): p. 759-780.

48. Serre, D., *Systems of Conservation Laws.* Vol. 1. 1999, Cambridge, UK: Cambridge University Press.

49. Weber, H., *Die Partiellen Differential-Gleichungen der Mathematischen Physik.* 1910, Braunschweig. p. Chapter 14.

50. Longsworth, L.G., *The concentration distribution in two salt moving boundaries.* Journal of the American Chemical Society, 1944. **66**: p. 449-453.

51. Longsworth, L.G., *A differential moving boundary method for transference numbers.* Journal of the American Chemical Society, 1943. **65**: p. 1755-1765.

52. Saville, D.A. and O.A. Palusinski, *Theory of Electrophoretic Separations Part I: Formulation of a Mathematical Model.* AIChE Journal, 1986. **32**(2): p. 207-214.

53. Mosher, R.A., et al., *Dynamic simulator for capillary electrophoresis with in situ calculation of electroosmosis.* Journal of Chromatography A, 1995. **716**: p. 17-26.

54. Dose, E.V. and G.A. Guiochon, *High -Resolution Modeling of Capillary Zone Electrophoresis and Isotachophoresis.* Analytical Chemistry, 1991. **63**: p. 1063-1072.

55. Martens, J.H.P.A., et al., *Transient modelling of capillary electrophoresis Isotachophoresis.* Journal of Chromatography A, 1997. **772**: p. 49-62.

56. Su, Y., O.A. Palusinski, and P.C. Fife, *Isotachophoresis: Analysis and Computation of the Structure of the Ionic Species Interface.* Journal of Chromatography, 1987. **405**: p. 77-85.

57. Ermakov, S.V. and P.G. Righetti, *Computer simulation for capillary zone electrophoresis A quantitative approach.* Journal of Chromatography A, 1994. **667**: p. 257-270.

58. Andreev, V.P. and E.E. Lisin, *On The Mathematical Model of Capillary Electrophoresis.* Chromatographia, 1993. **37**(3/4): p. 202-210.

59. Chien, R.-L., *Mathematical Modeling of Field-Amplified Sample Injection in High-Performance Capillary Electrophoresis.* Analytical Chemistry, 1991. **63**: p. 2866-2869.

60. Schwer, C., et al., *Computer Simulation and Experimental Evaluation of On-Column Sample Preconcentration in Capillary Zone Electrophoresis by Discontinuous Buffer Systems.* Analytical Chemistry, 1993. **65**: p. 2108-2115.

61. Moore, G.T., *Theory of isotachophoresis Development of concentration boundaries.* Journal of Chromatography, 1975. **106**: p. 1-16.

62. Gel'fand, I.M., *Some problems in the theory of quasilinear equations.* American Mathematical Society Translations, 1963. **29**: p. 295-380.

63. Mosher, R.A., D.A. Saville, and W. Thormann, *The Dynamics of Electrophoresis.* Electrophoresis Library, ed. B.J. Radola. 1992, Weinheim ; New York ; Basel ; Cambridge: VCH.

64. Courant, R., K.O. Friedrichs, and H. Lewy, *Uber die partiellen Differenzengleichungen der mathematischen Physik.* Math Ann, 1928. **100**: p. 32.

65. Richtmyer, R.D. and K.W. Morton, *Difference Methods for Initial-Value Problems.* Interscience Tracts in Pure and Applied Mathematics, ed. L. Bers, R. Courant, and J.J. Stoker. 1957: John Wiley & SOns.

66. Palusinski, O.A., et al., *Theory of Electrophoretic Separations Part II: Construction of a Numerical Simulation Scheme and Its Applications.* AIChE Journal, 1986. **32**(2): p. 215-223.

67. Ermakov, S.V., M.S. Bello, and P.G. Righetti, *Numerical algorithms for capillary electrophoresis.* Journal of Chromatography A, 1994. **661**: p. 265-278.

68. Ermakov, S.V., O.S. Mazhorova, and Y.P. Popov, Electrophoresis, 1992. **13**: p. 838-848.

69. Ermakov, S.V., O.S. Mazhorova, and Y.P. Popov, Informatica, 1992. **3**: p. 173-197.

70. Ermakov, S.V., et al., Analytical Chemistry, 1994. **66**: p. 4034-4042.

71. Ermakov, S.V., et al., Analytical Chemistry, 1995. **67**: p. 2957-2965.

72. Everaerts, F.M. and J.L. Beckers, *Isotachophoresis - Theory, Instrumentation and Applications.* Journal of Chromatography Library. Vol. 6. 1976: Elsevier, Amsterdam.

73. Poppe, H., Journal of Chromatography, 1990. **506**: p. 45-60.

74. Sounart, T.L. and J.C. Baygents, *Simulation of electrophoretic separations by the flux-corrected transport method.* Journal of Chromatography A, 2000. **890**: p. 321-336.

75. Sounart, T.L. and J.C. Baygents, *Simulation of electrophoretic separations: Effect of numerical and molecular diffusion on pH calculations in poorly buffered systems.* Electrophoresis, 2000. **21**: p. 2287-2295.

76. Book, D.L., J.P. Boris, and K. Hain, *Flux-corrected Transport II. Generalizations of the method.* Journal of Computational Physics, 1975. **18**: p. 248-283.

77. Boris, J.P. and D.L. Book, *Flux-Corrected Transport. III Minimal_Error FCT Algorithms.* Journal of Computational Physics, 1976. **20**: p. 397-431.

78. Zalesak, S.T., *Fully Multidimensional Flux-Corrected Transport Algorithms for Fluids.* Journal of Computational Physics, 1979. **31**: p. 335-362.

79. Lohner, R., et al., *Finite element flux-corrected transport (FEM-FCT) for the Euler and Navier-Stokes Equations.* International Journal for Numerical Methods in Fluids, 1987. **7**: p. 1093-1109.

80. Georghiou, G.E., R. Morrow, and A.C. Metaxas, *An improved finite-element flux-corrected transport algorithm.* Journal of Computational Physics, 1999. **148**: p. 605-620.

81. Georghiou, G.E., R. Morrow, and A.C. Metaxas, *A two-dimensional, finite-element, flux-corrected transport algorithm for the solution of gas discharge problems.* Journal of Physics D: Applied Physics, 2000. **33**: p. 2453-2466.

82. Takuma, T., *Recent developments in electric field calculation.* IEEE transactions on magnetics, 1997. **33**(March 1997): p. 1155-1160.

83. Takuma, T. and T. Kawamoto, *A very stable method for ion flow field of HVDC transmission lines.* IEEE transactions on power delivery, 1987. **PWRD-2**: p. 189-198.

84. Abdel-Salam, M. and Z. Al-Hamouz, *A finite-element analysis of bipolar ionized field.* IEEE transactions on industry applications, 1995. **31**(May/June): p. 477-483.

85. Al-Hamouz, Z., M. Abdel-Salam, and A. Mufti, *Improved calculation of finite-element analysis of bipolar corona including ion diffusion.* IEEE transactions on industry applications, 1998. **34**(March/April): p. 301-309.

86. Heller, C., *Principles of DNA separation with capillary electrophoresis.* Electrophoresis, 2001. **22**: p. 629-643.

87. Longsworth, L.G., *Moving Boundary Electrophoresis: Theory*, in *Electrophoresis*, M. Bier, Editor. 1959, Academic Press: New York, NY. p. 92-135.

88. Srivastava, A., et al. *Numerical modelling as a design optimization tool for DNA electrophoresis.* in *Fourth International Conference on Computation in Electromagnetics*. 2002. Bournemouth, UK.

89. MacInnes, D.A. and L.G. Longsworth, *Transference numbers by the method of moving boundaries: Theory, practice, and results.* Chemical Reviews, 1932. **11**(2): p. 171.

90. Beckers, J.L. and P. Bocek, *Sample stacking in capillary electrophoresis: Principles, advantages and limitations.* Electrophoresis, 2000. **21**: p. 2747-2767.

91. Jorgenson, J.W. and K.D. Lukacs, *Capillary Zone Electrophoresis.* Analytical Chemistry, 1981. **53**: p. 1298-1302.

Appendix 1. Nomenclature

$\vec{v}$ velocity of the DNA fragment (m/s)
$\vec{E}$ electric field intensity (V/m)
c_i concentration of species i (mol/m^3) or (mM)
D_i diffusion coefficient if species i (m^2/s)
$\vec{J}$ current density (A/m^2)
$\vec{\Gamma}_i$ flux of species i $(mol/m^2\cdot s)$
μ_i electrophoretic migration mobility of species I $(m^2/V\cdot s)$
ε dielectric permittivity $(C/V\cdot m)$
ε_0 permittivity of free space 8.85×10^{-12} $C^2/N\cdot m$
ε_r dielectric constant
σ electrical conductivity (S/m)
λ molar conductivity $(A/m^2)(m^2/\Omega\cdot mol)$
μ dynamic viscosity $(Pa\cdot s)$
κ inverse Debye length (m^{-1})
ρ mass density (kg/m^3)
$\vec{J}$ current density (A/m^2)
ρ_c current density C/m^3
F Faraday's constant 9.640×10^4 C/mol
N_A Avogadro's number
Pe Peclet number
ς Zeta potential V
I current (A)
z valence (C/mol)
R gas constant $(8.314$ $C/mol)$
k Boltzmann's constant $(1.38\times10^{-23}$ $J/K)$

Appendix 2. Maxwell's Equation's and Charge Conservation

Review of Maxwell's equations of electrodynamics:

Gauss's law $$\nabla\cdot(\varepsilon\vec{E})=\rho \tag{A.1}$$

Magnetic flux continuity $$\nabla\cdot\vec{B}=0 \tag{A.2}$$

Faraday's law $$\nabla\times\vec{E}=-\frac{\partial\vec{B}}{\partial t} \tag{A.3}$$

Ampère's law $$\nabla\times\vec{H}=\vec{J}+\frac{\partial\vec{D}}{\partial t} \tag{A.4}$$

Constitutive equations: $$\vec{D}=\varepsilon\vec{E} \text{ and } \vec{B}=\mu\vec{H} \tag{A.5}$$

Charge conservation:

We can show that charge conservation is embedded in Maxwell's laws. Taking divergence of Ampère's law:

$$\nabla\cdot(\nabla\times\vec{H})=\nabla\cdot(\vec{J}+\frac{\partial\vec{D}}{\partial t}) \tag{A.6}$$

$$0=\nabla\cdot\vec{J}+\frac{\partial(\nabla\cdot\vec{D})}{\partial t} \tag{A.7}$$

$$0=\nabla\cdot\vec{J}+\frac{\partial\rho}{\partial t} \tag{A.8}$$

Appendix 3. Matlab Program for Electrophoresis

```
% bel.m
% Alok Srivastava April 13, 2002

start_time=clock; start_time=start_time(4:6)
num_x = 500;     %
n_disp= num_t/15;     %
boundary1= 50;   %
boundary2= 400;  %

df=3; %3
df2=2;

dt=5e-5;
dx=1e-6;
d1= df*0.5e-9;
d2= df*2e-9;
d3= df*0.75e-9;

width=50;

m1= 20e-9; m2=79e-9; m3=29e-9;
m4=10e-9;                 d4=4e-10;

m4_1=  4e-9;      d4_1=(4/20)*1e-10;
m4_2=  5e-9;      d4_2=(5/20)*1e-10;
% m4_3=  6e-9;    d4_3=(6/20)*1e-10;
m4_4=  10e-9;     d4_4=(10/20)*1e-10;
m4_5=  15e-9;     d4_5=(15/20)*1e-10;
%m4_6=  19.5e-9; d4_6=df*(19/20)*1e-10;
m4_7=  20e-9;   d4_7=df2*2e-10;
%m4_8=  20.5e-9; d4_8=df*2e-10;
%m4_9=  21e-9;   d4_9=df*2e-10;
m4_10= 24e-9;   d4_10=df2*4e-10;

n_data = fix( num_t/n_disp );
csam(n_data, num_x)=0;

c1_sam=csam;
c2_sam=csam;
c3_sam=csam;

csam_1=csam;
csam_2=csam;
csam_4=csam;
csam_5=csam;
csam_7=csam;
csam_10=csam;


count_data=0;

E(1:num_x)=0;
sigma(1:num_x)=0;
v1(1:num_x)=0;v2(1:num_x)=0;v3(1:num_x)=0;

cA=10; cB=22.7; sample_conc=5e-2;
        % cB=25 before
x=[1:num_x].*dx*1e6;

xr1=[0:(1/width):1];
xra=(cos(xr1*pi));
xra=xra+1;
xra=xra./2; % decreasing
xrb=1-xra;       % increasing

% initial conditions
c1(1:num_x)=cA;
c1(boundary1:boundary1+width) = xra*cA;    % for
decreasing
c1(boundary1+width+1:boundary2-1)=0;
c1(boundary2:boundary2+width) = xrb*cA;    % then
increasing

c2(1:num_x)=cB;
c2(1:boundary1-1)=0;
c2(boundary1:boundary1+width) = xrb*cB;    % for
increasing
c2(boundary2:boundary2+width) = xra*cB;    % for
decreasing
```

```
c2(boundary2+width+1:num_x)=0;


c3=c1+c2;
c4=(c2./cB).*0.05;
c4_1=c4;  c4_2=c4;
%c4_3=c4;
c4_4=c4; c4_5=c4;
%c4_6=c4;
c4_7=c4; % c4_8=c4;
%c4_9=c4;
c4_10=c4;


% initializing variables
cz=c1*0;
c1s=cz; c2s=cz; c3s=cz; %c4s=cz;
c4_1s=cz; c4_2s=cz;
%c4_3s=cz;
c4_4s=cz; c4_5s=cz;
% c4_6s=cz;
c4_7s=cz; % c4_8s=cz;
%c4_9s=cz;
c4_10s=cz;


v1=cz; v2=cz; v3=cz; %v4=cz;
v4_1=cz; v4_2=cz;
%v4_3=cz;
v4_4=cz; v4_5=cz;
% v4_6=cz;
v4_7=cz; % v4_8=cz;
%v4_9=cz;
v4_10=cz;


sigma = 1e5.*( c1.*m1 + c2.*m2 + c3.*m3 ) ;

E = J./sigma;


%figure(1); clf;
%plot(x,c3,'b-.'); hold on; plot(x,c1,'r--'); grid;
plot(x,c2,'g--'); ;


%figure(2); clf;
%plot(x,E,'b--'); hold on; grid;


%figure(3); clf;
%plot(x,c4,'r-.'); grid; hold on;


% for every time step


for n = 1:num_t
   % apply boundary condition
   c1(1)=cA;    c2(1)=0;   c3(1)=cA;   %c4(1)=0;
   c1s(1)=cA;    c2s(1)=0;   c3s(1)=cA;
%c4s(1)=0;
   c4_1s(1)=0;   c4_2s(1)=0;
   %c4_3s(1)=0;
   c4_4s(1)=0;   c4_5s(1)=0;
   %c4_6s(1)=0;
   c4_7s(1)=0;  %c4_8s(1)=0;
   %c4_9s(1)=0;
   c4_10s(1)=0;


   sigma = 1e5.*( c1.*m1 + c2.*m2 + c3.*m3 ) ;
   E = J./sigma;
   v1=m1.*E; v2=m2.*E; v3=m3.*E; v4=m4.*E;
   v4_1=m4_1.*E;   v4_2=m4_2.*E;
   %v4_3=m4_3.*E;
   v4_4=m4_4.*E; v4_5=m4_5.*E;   % v4_6=m4_6.*E;
   v4_7=m4_7.*E;   % v4_8=m4_8.*E;
   %v4_9=m4_9.*E;
   v4_10=m4_10.*E;


   for i=2:num_x-1
      % FTCS
      c1s(i) = c1(i) + d1*dt*( c1(i+1)-
2*c1(i)+c1(i-1) )/(dx*dx)  ...
           -dt*(v1(i+1)*c1(i+1) - v1(i-1)*c1(i-
1))/(2*dx);


      c2s(i) = c2(i) + d2*dt*( c2(i+1)-
2*c2(i)+c2(i-1) )/(dx*dx)  ...
         -dt*(v2(i+1)*c2(i+1) - v2(i-1)*c2(i-
1))/(2*dx);


      if mod(i,2)==0
      c2s(i)=c3(i)-c1(i);
      end;


      %c4s(i) = c4(i) + d4*dt*( c4(i+1)-
2*c4(i)+c4(i-1) )/(dx*dx)  ...
      %   -dt*(v4(i+1)*c4(i+1) - v4(i-1)*c4(i-
1))/(2*dx);
```

```
      c4_1s(i) = c4_1(i) + d4_1*dt*( c4_1(i+1)-
2*c4_1(i)+c4_1(i-1) )/(dx*dx)  ...

         -dt*(v4_1(i+1)*c4_1(i+1) - v4_1(i-
1)*c4_1(i-1))/(2*dx);


      c4_2s(i) = c4_2(i) + d4_2*dt*( c4_2(i+1)-
2*c4_2(i)+c4_2(i-1) )/(dx*dx)  ...

         -dt*(v4_2(i+1)*c4_2(i+1) - v4_2(i-
1)*c4_2(i-1))/(2*dx);


      %c4_3s(i) = c4_3(i) + d4_3*dt*( c4_3(i+1)-
2*c4_3(i)+c4_3(i-1) )/(dx*dx)  ...

       %  -dt*(v4_3(i+1)*c4_3(i+1) - v4_3(i-
1)*c4_3(i-1))/(2*dx);


      c4_4s(i) = c4_4(i) + d4_4*dt*( c4_4(i+1)-
2*c4_4(i)+c4_4(i-1) )/(dx*dx)  ...

         -dt*(v4_4(i+1)*c4_4(i+1) - v4_4(i-
1)*c4_4(i-1))/(2*dx);


      c4_5s(i) = c4_5(i) + d4_5*dt*( c4_5(i+1)-
2*c4_5(i)+c4_5(i-1) )/(dx*dx)  ...

         -dt*(v4_5(i+1)*c4_5(i+1) - v4_5(i-
1)*c4_5(i-1))/(2*dx);


      %c4_6s(i) = c4_6(i) + d4_6*dt*( c4_6(i+1)-
2*c4_6(i)+c4_6(i-1) )/(dx*dx)  ...

      %   -dt*(v4_6(i+1)*c4_6(i+1) - v4_6(i-
1)*c4_6(i-1))/(2*dx);


      c4_7s(i) = c4_7(i) + d4_7*dt*( c4_7(i+1)-
2*c4_7(i)+c4_7(i-1) )/(dx*dx)  ...

         -dt*(v4_7(i+1)*c4_7(i+1) - v4_7(i-
1)*c4_7(i-1))/(2*dx);


      %c4_8s(i) = c4_8(i) + d4_8*dt*( c4_8(i+1)-
2*c4_8(i)+c4_8(i-1) )/(dx*dx)  ...

      %   -dt*(v4_8(i+1)*c4_8(i+1) - v4_8(i-
1)*c4_8(i-1))/(2*dx);


      %c4_9s(i) = c4_9(i) + d4_9*dt*( c4_9(i+1)-
2*c4_9(i)+c4_9(i-1) )/(dx*dx)  ...

       %  -dt*(v4_9(i+1)*c4_9(i+1) - v4_9(i-
1)*c4_9(i-1))/(2*dx);


      c4_10s(i) = c4_10(i) + d4_10*dt*( c4_10(i+1)-
2*c4_10(i)+c4_10(i-1) )/(dx*dx)  ...

         -dt*(v4_10(i+1)*c4_10(i+1) - v4_10(i-
1)*c4_10(i-1))/(2*dx);


      end;
```

```
      for i=2:num_x-1


      j=num_x-i+1;


      c3s(j) = c3(j) + d3*dt*( c3(j+1)-
2*c3(j)+c3(j-1) )/(dx*dx)  ...

          +dt*(v3(j+1)*c3(j+1) - v3(j-1)*c3(j-
1))/(2*dx);


     end


   c1s(num_x-1) = c1s(num_x-2)  ;

   c2s(num_x-1) = c2s(num_x-2)  ;

   c3s(num_x-1) = c3s(num_x-2)  ;

   %c4s(num_x-1) = c4s(num_x-2)  ;

   c4_1s(num_x-1) = c4_1s(num_x-2)  ;

   c4_2s(num_x-1) = c4_2s(num_x-2)  ;

   %c4_3s(num_x-1) = c4_3s(num_x-2)  ;

   c4_4s(num_x-1) = c4_4s(num_x-2)  ;

   c4_5s(num_x-1) = c4_5s(num_x-2)  ;

   %c4_6s(num_x-1) = c4_6s(num_x-2)  ;

   c4_7s(num_x-1) = c4_7s(num_x-2)  ;

   %c4_8s(num_x-1) = c4_8s(num_x-2)  ;

   %c4_9s(num_x-1) = c4_9s(num_x-2)  ;

   c4_10s(num_x-1) = c4_10s(num_x-2)  ;


   c1s(num_x) = c1s(num_x-1)  ;

   c2s(num_x) = c2s(num_x-1)  ;

   c3s(num_x) = c3s(num_x-1)  ;

   %c4s(num_x) = c4s(num_x-1)  ;

   c4_1s(num_x) = c4_1s(num_x-1)  ;

   c4_2s(num_x) = c4_2s(num_x-1)  ;

   %c4_3s(num_x) = c4_3s(num_x-1)  ;

   c4_4s(num_x) = c4_4s(num_x-1)  ;

   c4_5s(num_x) = c4_5s(num_x-1)  ;

   %c4_6s(num_x) = c4_6s(num_x-1)  ;

   c4_7s(num_x) = c4_7s(num_x-1)  ;

   %c4_8s(num_x) = c4_8s(num_x-1)  ;

   %c4_9s(num_x) = c4_9s(num_x-1)  ;

   c4_10s(num_x) = c4_10s(num_x-1)  ;


   c1=c1s; c2=c2s; c3=c3s; %c4=c4s;

   c4_1=c4_1s; c4_2=c4_2s;

   %c4_3=c4_3s;
```

```
   c4_4=c4_4s; c4_5=c4_5s; % c4_6=c4_6s;

   c4_7=c4_7s; % c4_8=c4_8s;

   %c4_9=c4_9s;

   c4_10=c4_10s;


  if (mod(n,n_disp)==0)  % 100

      count_data=count_data+1;

      %figure(1)

      %plot(x,c3,'b--');

      %plot(x,c1,'r--');

      %plot(x,c2,'g--');


      %figure(2);

      %plot(x,E,'b--');


      %figure(3);

      %plot(x,c4,'r--');


      c1_sam(count_data,:)=c1;

      c2_sam(count_data,:)=c2;

      c3_sam(count_data,:)=c3;


                  %csam(count_data,:)=c4;

                  csam_1(count_data,:)=c4_1;
csam_2(count_data,:)=c4_2;

      %csam_3(count_data,:)=c4_3;

      csam_4(count_data,:)=c4_4;
csam_5(count_data,:)=c4_5;

      %csam_6(count_data,:)=c4_6;

                  csam_7(count_data,:)=c4_7;
%csam_8(count_data,:)=c4_8;

                  %csam_9(count_data,:)=c4_9;

                  csam_10(count_data,:)=c4_10;


             end


        end


        figure(1);

        title('Electrolyte Concentration'  );

        ylabel('concentration (mol/m^3)'  );

        xlabel('distance (\mum)');

        legend('c3','c1','c2');


        figure(2);

        title('Electric Field'  );

        ylabel('electric field intensity (V/m)'  );

        xlabel('distance (\mum)');

        % axis([ 0 5 0 5000 ]);


        figure(3);

        title('Sample Concentration'  );

        ylabel('Concentration (mol/m^3)'  );

        xlabel('distance (\mum)');


        end_time=clock; end_time=end_time(4:6)


        save(savefile,'csam*', 'c1_sam', 'c2_sam',
        'c3_sam', 'start_time','end_time');
```

Appendix 4. Details of Experiments and Data Files

Description of experimental data used in the analysis

CD1 5/31/2000
500bp M13mp18 dsDNA
2% LPA (051700A) with urea
250μm offset glass chip 12 cm long
10X magnification
x2 binning, 8 bit data
250V, 500V, 1000V, 1250V, 1500V, 1750V
DNA 10^{-8}M

CD2 5/22/2000
500bp M13mp18 dsDNA
2% LPA with urea
250μm offset glass chip 12 cm long
10X magnification
x2 binning, 12 bit data
150V, 300V, 750V
DNA 10^{-10}M

CD3 7/13/2000
M13mp18 ssDNA sequencing reaction
2% LPA (051700A) with urea
250μm offset glass chip
10X magnification
x2 binning, 8 bit data
500V, 750V, 1000V, 1500V
DNA 2.5 x 10^{-10}M

CD4 2/28/2001
M13mp18 ssDNA sequencing Big dye terminator
2% LPA (051700A) with urea
250μm offset with 2.5mm arms
150μm offset with 4 and 2mm arms
10X magnification
x2 binning, 8 bit data
2K, 3K, 4K, 5K, 6K, 7K, 8K, 9K
DNA 3.3 x 10^{-10}M
Ethanol precipitated

CD5 3/20/2001
M13mp18 ssDNA sequencing Big dye terminator
2% LPA (051700A) with urea
150μm offset with 4 and 2mm arms
10X magnification
x2 binning, 8 bit data
3K, 4K, 5K, 6K, 7K, 8K, 9K
DNA 3.3 x 10^{-10}M
Spin column

CD6 4/6/2001
M13mp18 ssDNA sequencing Big dye terminator
2% LPA (051700A) with urea
500μm offset with 4 and 2mm arms
10X magnification
x4, x8 binning, 8 bit data
1K, 2K, 3K, 4K, 5K, 6K, 7K, 8K, 9K
DNA 3.3 x 10^{-10}M
Spin column and ethanol precipitation

CD7 4/5/2001
M13mp18 ssDNA sequencing Big dye terminator
2% LPA (051700A) with urea
250μm offset with 4 and 2mm arms
10X magnification
x2, x8 binning, 8 bit data

2K, 3K, 4K, 5K, 6K, 7K, 8K, 9K

DNA 3.3 x 10^{-10}M

Spin column and ethanol precipitation

CD 8 4/1/2001

M13mp18 ssDNA sequencing Big dye terminator

2% LPA (051700A) with urea

250μm offset with 4 and 2mm arms

10X magnification

x2, x4 binning, 8 bit data

3K, 4K, 5K,6K, 7K, 8K, 9K, 10K

DNA 3.3 x 10^{-10}M

Spin column and ethanol precipitation

CD 9 10/20/2000

Description not available

CD 10 4/4/2000

100bp lambda phage dsDNA

2% LPA (051700A) with urea

250μm offset glass chip 12 cm long

10X, 20X, 60X magnification

x2, x4 binning,

0.35kV

CD 11 8/3/2000

M13mp18 ssDNA sequencing Big dye terminator

2% LPA (051700A) with urea

100μm offset 2.5mm arms

250μm offset 2.5mm arms

500μm offset 2.5mm arms

10X magnification

x2 binning, 8 bit data

1000V, 1250V, 1500V, 1750V

DNA 2.5 x 10^{-10}M

CD 12 10/2/2000

M13mp18 ssDNA sequencing Big dye terminator

2% LPA (051700A) with urea

1000μm offset 2.5mm arms

10X magnification

x2 binning, 8 bit data

1000V, 1250V, 1500V, 1750V

DNA 3.3x10^{-10}M

CD 13 7/20/2000

M13mp18 ssDNA sequencing Big dye terminator

2% LPA (051700A) with urea

250μm offset glass chip 12 cm long

10X magnification

x2 binning, 8 bit data

1000V, 1250V, 1500V, 1750V

DNA 2.5x10^{-10}M

CD 14 5/23/2000

500 bp M13mp18 dsDNA

2% LPA with urea

250μm offset glass chip 12cm long

10X magnification

x2 binning, 8 bit data

600V, 1000V, 1500V, 2000V

DNA 10^{-8}M

CD 15 10/6/2000

M13mp18 ssDNA sequencing Big dye terminator

2% LPA (051700A) with urea

1000μm offset 2.5mm arms

150μm offset 2.5mm arms

10X magnification

x2 binning, 8 bit data

1000V, 1250V, 1500V, 1750V

DNA 3.3x10^{-10}M

Appendix 5. Buffer Composition

TBE Buffer
1×**TBE** Tris borate-EDTA solution
Buffer will contain 89 mM Tris; 89 mM borate ; 2 mM EDTA and have a pH approx. 8.3
Buffer will contain 10.8 g/l Tris-borate; 5.5 g/l boric acid; 0.744 g/l EDTA
10× TBE Buffer will contain 108 g/l Tris-borate; 55 g/l boric acid; 7.44 g/l EDTA

10X TBE Buffer

Component	mg/liter
Boric Acid	55,000 (55.03)
EDTA. Na_2	7,440 (7.44)
Tris	108,000 (107.82)

Tris(hydroxymethyl) aminomethane
Formula: C4H11NO3 12*4+1*11+14+16*3=121 Molecular Weight: 121.14
Chemical Formula: $H_2N.C.(CH_2OH)_3$
TRIS; 2-Amino-2-(hydroxymethyl)-1,3-propanediol; THAM; Tromethamine (USP); TRIS (Base); Trisamine
pKa-Value: 8.3 at 20°C
Melting point: 167 - 172° C
Absorbance: <=0.015 at 300 nm (100 mg/ml in water)
Solubility: 550 mg/mL
pH: 10.4 (0.1 molar solution)

Boric Acid
Molecular Weight: 61.83 (3*1+10.8+16*3=61.83)
Chemical Formula: H_3BO_3
Solubility: 1g/18mL in cold water.
Density: 1.43
pH: 5.1 Aqueous solution: (0.1M)

EDTA Disodium Salt
Synonyms: (Ethylenedinitrilo) tetraacetic acid disodium salt; Disodium EDTA; disodium dihydrogen ethylenediaminetetraacetate; disodium edetate; N,N'-1,2-ethanediylbis (N-(carboxymethyl)- glycine), disodium salt, dihydrate
Molecular Weight: 372.24
Chemical Formula: $C_{10}H_{14}O_8N_2Na_2.2H_2O$
Formula weight 12*10+1*14+16*8+14*2+23*2+2*(2+16) = 372
Chemical Formula: C10H14O8N2Na2.2H2O
Solubility: 10 g in 100 g of water.

Dilute 1 in 10 with deionized water
The pH of 1X buffer should be 8.3

TTE buffer
1X 50mM Tris 50mM TAPS 2mM EDTA

Tris(hydroxymethyl) aminomethane
Molecular Weight: 121.14
Chemical Formula: $H_2N.C.(CH_2OH)_3$
pKa-Value: 8.3 at 20°C
pH: 10.4 (0.1 molar solution)

TAPS
$HOCH_2.C(CH_2OH)_2NH.CH_2.CH_2.CH_2\text{-}SO_2\text{-}OH$
N-tris(Hydroxymethyl)methyl-3-aminopropanesulfonic acid;
Molecular Formula: $C_7H_{17}NO_6S$
Structiral formula: $HOCH_2.C(CH_2OH)_2\ NH\ CH_2.CH_2.CH_2.SO_2.OH$
Molecular Weight =243.28
pKa = 8.4 at 25°C; useful pH range 7.7-9.1

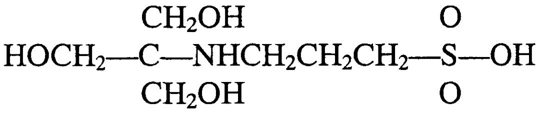

$$HOCH_2-\overset{CH_2OH}{\underset{CH_2OH}{C}}-NHCH_2CH_2CH_2-\overset{O}{\underset{O}{S}}-OH$$

EDTA Disodium Salt
Ethylenediaminetetraacetic acid
Molecular Weight: 372.24
Chemical Formula: $C_{10}H_{14}O_8N_2Na_2.2H_2O$
Formula weight 12*10+1*14+16*8+14*2+23*2+2*(2+16) = 372
Chemical Formula: $C_{10}H_{14}O_8N_2Na_2.2H_2O$
Solubility: 10 g in 100 g of water.

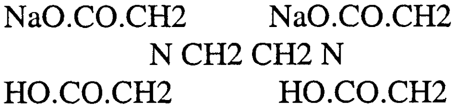

$$\begin{matrix} \text{NaO.CO.CH2} & & \text{NaO.CO.CH2} \\ & \text{N CH2 CH2 N} & \\ \text{HO.CO.CH2} & & \text{HO.CO.CH2} \end{matrix}$$

Appendix 6. Buffer Dissociation Constants

Electro-chemistry; reaction kinetics

water

$$H_2O \rightarrow H^+ + OH^-, \quad K_w = \frac{\left[H^+\right]\left[OH^-\right]}{[H_2O]} = 10^{-14}, \quad pH = -\log_{10}\left[H^+\right]$$

Acid – general

$$HA \rightarrow H^+ + A^-, \quad K_{acid} = \frac{\left[H^+\right]\left[A^-\right]}{[HA]}$$

degree of ionization m

$$m = \frac{\left[A^-\right]}{\left[A^-\right]+[HA]} = \frac{\left[A^-\right]}{\left[A^-\right]+\frac{\left[H^+\right]\left[A^-\right]}{K_{acid}}} = \frac{K_{acid}}{K_{acid}+H}$$

Base – general

$$BOH \rightarrow B^+ + OH^-, \quad K_{base} = \frac{\left[B^+\right]\left[OH^-\right]}{[BOH]}$$

$$m = \frac{\left[B^+\right]}{\left[B^+\right]+[BOH]} = \frac{\left[B^+\right]}{\left[B^+\right]+\frac{\left[B^+\right]\left[OH^-\right]}{K_{base}}} = \frac{1}{1+\frac{K_w[H_2O]}{K_{base}\left[H^+\right]}}$$

$$m = \frac{1}{1+\frac{K_w}{K_{base}\left[H^+\right]}} = \frac{H}{H+\frac{K_w}{K_{base}}} = \frac{H}{H+K}$$

Appendix 7. Video Microscopy of Sample Injection

Experimental Protocol

A. Preparation

1. Turn on laser (allow to warm up)
2. Check laser power with photometer
3. Make sure water bath is full and at 50C
4. Place 1xTTE buffer and sample in bucket of ice
5. Fill syringe on press with running gel

B. Plate preparation

1. Remove water from vials
2. Fill channel with running gel
3. Check for bubbles
4. Rinse each vial with $H2O$ 3x using a new pipette tip each time
5. Fill SAMPLE vial with $H2O$
6. Fill BUFFER and WASTE vials with 1x TTE buffer
7. Clean plate, especially where laser will be going through
channel
(approximately 11.5 cm from cross injector)
8. Secure plate on stage so that laser goes through channel
approximately 11.5 cm from
cross injector
9. Clean electrodes with water and place in appropriate vials

C. Pre-electrophoresis

1. Log new entry

2. Rename file for data acquisition
3. Pullback is OFF
4. Power switch is in RUN position
5. Turn on power supply (set at 2.3 kV)
6. Pre-electrophorese channel for 5 mins
7. Record initial and final current
8. Switch power switch to LOAD position
9. Pre-electrophorese injector for 3 mins
10. Record current at 0, 10, 20, 30, 60, 90, 120, 150 and 180 seconds
11. SHUT OFF POWER SUPPLY

D. Sample

1. Rinse SAMPLE vial 3x with H2O
2. Clean SAMPLE electrode
3. Add 12ml of sample
4. Add 12 ul of buffer to waste vial
5. Place electrode in SAMPLE vial

E. Electrophoresis

1. Pullback is OFF
2. Power switch on LOAD
3. Turn on power supply (set at 2.3 kV)
4. Record current of cross injector at 0, 10, 20, 30, 60, 90, 120, 150 and 180 seconds
5. At 180 seconds, switch to RUN and high voltage and start data acquisition
6. At 5 seconds, switch voltage back down to 2.3 kV.
7. After 10 seconds, Pullback is ON
8. SHUT OFF POWER SUPPLY

9. Fill sample vial with 1x TTE buffer
10. Shut off lights
11. Turn on lamp and place over stage laser hole
12. Center laser in channel
13. Focus channel
14. Open PMT's
15. Turn power supply on

F. Shut down

1. SHUT OFF POWER SUPPLY
2. Stop data acquisition
3. Remove plate from stage
4. Fill vials with H2O
5. Cover with parafilm
6. Turn off laser (make sure fan is still on)
7. Put buffer and gel into refrigerator, and sample in freezer

Additional Information on Experiments

Some details about experiments are given below, from communication with M. Vazquez.

"I used 10-12 different voltages for injection which involve the cathode and anode electrode (top and bottom wells). It was reported that voltages ranged from 50 V/cm; upto 700 V/cm. A double-T injector with total channel length of ~5mm was used for all the experiments. The injector offset was 250 μm, 350 μm or 500 μm. All channels were 40 um deep and 90 um wide."

"Conductivity changes with chemical composition of the sample, among other things. I used two methods of DNA purification (spin column and ethanol precipitation) in order to get two different salt concentrations and hence two different conductivities: 148 S/m and 58 S/m."

"10^{-10} M DNA solution was always the standard."

"The sieving gel was Polyacrylamide PAA, prepared in the lab of (9MDa) at 2% concentration. Std 1XTTE for runs and 1XTBE for gel prep."

"Monodisperse samples (i.e. PCR product of same MW) and polydisperse samples in the form of sequencing reactions from Mark (Novotny) were used."

"The voltage applied to the cross injector - did you ever swap the ends? " (author)

"... Not significant difference, just directional change."

"The arms varied between 2.5mm for each or 2mm and 3mm for sample/waste."

Appendix 8. DNA Mobility as a Function of Size

The following analysis by Lumpkin and Zimm [39] explained the inverse-length dependence DNA electrophoretic mobility in gels.

Assume: (1) worm-like polymer motion, (2) frictional coefficient proportional to polymer length, (3) a random polymer conformation defined by Gaussian statistics, and (4) counter-ion screening is accounted for by replacing the polymer-ion's own charge by an effective charge. Consider a polymer ion to occupy and move, like a worm in a burrow, along a random tube in the gel. The total tangential electric force exerted on the polymer ion by a constant electric field $\vec{E}$ in the x direction is

$$\frac{Q}{L}\sum \vec{E}\cdot\Delta s = \frac{QE}{L}\sum \hat{i}\cdot\Delta s = \frac{QEh_x}{L}, \tag{A.9}$$

where Δs is a length increment tangent to the polymer ion at every point and the sum is over the contour of the molecule, L being the contour length, $\hat{i}$ the unit vector in the x-direction, h_x the component of the polymer's end-to-end vector parallel to the electric field, E, and Q the polymer ion's total effective charge. If the polymer's translational frictional coefficient is ξ, then the equation of translational motion along the tube is

$$\xi\dot{s} = QEh_x / L, \tag{A.10}$$

where $\dot{s}$ is the polymer's mean velocity along the tube. The velocity of the polymer's center of mass parallel to the field is

$$\dot{X}_{cm} = \dot{s}h_x / L, \tag{A.11}$$

where h_x is the same as in Equations (A.9) and (A.10). This relation follows from the definition of the center of mass and the definition of wormlike motion. That is

$$M\vec{R}_{cm} = \sum m_i\vec{r}_i \tag{A.12}$$

and taking time derivatives

$$M\dot{\vec{R}}_{cm} = \sum m_i\dot{\vec{r}}_i \tag{A.13}$$

where M is the polymer's mass, m_i the mass of the ith segment, and $\dot{\vec{r}}_i$ is its velocity. Now write

$$m_i = M \Delta s_i / L, \tag{A.14}$$

where Δs_i is the contour length of the segment. Further, with assumption of wormlike motion,

$$\dot{r}_i = \dot{s}_i \hat{t}_i = \dot{s} \hat{t}_i, \tag{A.15}$$

where $\hat{t}_i$ is the unit vector tangent to the ith segment and $\dot{s} = \dot{s}_i$ the common magnitude of the tangential velocity of all the segments. Using Equations (A.13) and (A.14) in Equation (A.12), the following is obtained:

$$\dot{\vec{R}}_{cm} = \frac{\dot{s}}{L} \sum \hat{t}_i \cdot \Delta s_i = \frac{\dot{s}}{L} h, \tag{A.16}$$

where h is the polymer's random end-to-end vector. Equation (A.11) is the component of Equation (A.15) parallel to the E-field.

Using Equations (A.10) and (A.11) and taking averages, we obtain

$$\left\langle \dot{X}_{cm} \right\rangle = \frac{\left\langle h_x^2 \right\rangle QE}{L^2 \xi}. \tag{A.17}$$

As Q and ξ are both assumed proportional to L, (Q / ξ) is independent of L. Since for gaussian statistics $\left\langle h_x^2 \right\rangle$ is proportional to L, $\left\langle \dot{X}_{cm} \right\rangle / E$, the mobility is protional to L^{-1}.

This theory is true with the following limitations:

(1) The electric field is small, and field induced changes in polymer conformations may be neglected.

(2) For DNA shorter than or comparable to persistence length the dependence of mobility to length is weak.

(3) Pore size is small compared with persistence length. The persistence length of DNA is approximately 500Å

Appendix 9. Width of Moving Boundary

Assume there are three electrolyte species: two co-ions and a counter ion. Start with the following governing equations:

$$\frac{\partial c_1}{\partial t}+\frac{\partial}{\partial x}(z_1\mu_1 c_1 E-D_1\frac{\partial c_1}{\partial x})=0$$

$$\frac{\partial c_2}{\partial t}+\frac{\partial}{\partial x}(z_2\mu_2 c_2 E-D_2\frac{\partial c_2}{\partial x})=0$$

$$\frac{\partial c_3}{\partial t}+\frac{\partial}{\partial x}(z_3\mu_3 c_3 E-D_3\frac{\partial c_3}{\partial x})=0.$$

The current density may be expressed as $J=-F\left(\sum_{j=1}^{j=3} c_j\mu_j z_j\frac{\partial V}{\partial x}+D_j\frac{\partial c_j}{\partial x}\right)$. Seek a solution of the form $c=f(x-v_b t)$.

$$\partial c/\partial t=-v_b f'(x-v_b t)=-v_b\partial c/\partial x$$

Upon integration of the conservation laws and the characteristic equation:

$$\frac{\partial c_j}{\partial t}=\frac{\partial}{\partial x}(z_j\mu_j c_j\frac{\partial V}{\partial x}+D_j\frac{\partial c_j}{\partial x})$$

$$-v_b\frac{\partial c_j}{\partial x}=\frac{\partial}{\partial x}(z_j\mu_j c_j\frac{\partial V}{\partial x}+D_j\frac{\partial c_j}{\partial x})$$

$$v_b\frac{\partial c_j}{\partial x}+\frac{\partial}{\partial x}(z_j\mu_j c_j\frac{\partial V}{\partial x}+D_j\frac{\partial c_j}{\partial x})=0$$

Integrating:

$$v_b c_j+(z_j\mu_j c_j\frac{\partial V}{\partial x}+D_j\frac{\partial c_j}{\partial x})=A_j$$

$$v_b c_1+(z_1\mu_1 c_1\frac{\partial V}{\partial x}+D_1\frac{\partial c_1}{\partial x})=A_1$$

$$v_b c_2+(z_2\mu_2 c_2\frac{\partial V}{\partial x}+D_2\frac{\partial c_2}{\partial x})=A_2$$

$$v_b c_3+(z_3\mu_3 c_3\frac{\partial V}{\partial x}+D_3\frac{\partial c_3}{\partial x})=A_3$$

The current density, including the diffusion terms, is

$$J = z_1F\Gamma_1 + z_2F\Gamma_2 + z_3F\Gamma_3 .$$

$$J = z_1F(z_1\mu_1c_1\frac{\partial V}{\partial x} + D_1\frac{\partial c_1}{\partial x}) + z_2F(z_2\mu_2c_2\frac{\partial V}{\partial x} + D_2\frac{\partial c_2}{\partial x}) + z_3F(z_3\mu_3c_3\frac{\partial V}{\partial x} + D_3\frac{\partial c_3}{\partial x})$$

Also $J = z_1F(A_1 - c_1v_b) + z_2F(A_2 - c_2v_b) + z_3F(A_3 - c_3v_b)$.

$$J / F = z_1(A_1 - c_1v_b) + z_2(A_2 - c_2v_b) + z_3(A_3 - c_3v_b)$$

$$J / F = (z_1A_1 + z_2A_2 + z_3A_3) - v_b(z_1c_1 + z_2c_2 + z_3c_3)$$

Charge neutrality implies $z_1c_1 + z_2c_2 + z_3c_3 = 0$.

$$J / F = (z_1A_1 + z_2A_2 + z_3A_3) - v_B(z_1c_1 + z_2c_2 + z_3c_3)$$

$$J / F = (z_1A_1 + z_2A_2 + z_3A_3)$$

When $z_1 = 1$, $z_2 = 1$, and $z_3 = -1$,

$$J / F = A_1 + A_2 - A_3 .$$

As $x \longrightarrow +\infty$, $c_1 = 0$. Therefore, $A_1 = 0$. As $x \longrightarrow -\infty$, $c_2 = 0$. Therefore, $A_2 = 0$. From above, $A_3 = J / F$. From the Nernst-Einstein equation,

$$v_bc_1 + (z_1\mu_1c_1\frac{\partial V}{\partial x} + D_1\frac{\partial c_1}{\partial x}) = 0$$

$$v_bc_2 + (z_2\mu_2c_2\frac{\partial V}{\partial x} + D_2\frac{\partial c_2}{\partial x}) = 0$$

$$v_bc_3 + (z_3\mu_3c_3\frac{\partial V}{\partial x} + D_3\frac{\partial c_3}{\partial x}) = J / F$$

$$v_b + (z_1\mu_1\frac{\partial V}{\partial x} + \frac{D_1}{c_1}\frac{\partial c_1}{\partial x}) = 0$$

$$v_b + (z_2\mu_2\frac{\partial V}{\partial x} + \frac{D_2}{c_2}\frac{\partial c_2}{\partial x}) = 0$$

$$v_bc_3 + (z_3\mu_3c_3\frac{\partial V}{\partial x} + D_3\frac{\partial c_3}{\partial x}) = J / F$$

Since $D = \mu RT / F$ or $D = \mu k$ (where $k = RT / F$),

$$v_b + (z_1\mu_1\frac{\partial V}{\partial x} + \frac{\mu_1 k}{c_1}\frac{\partial c_1}{\partial x}) = 0$$

$$v_b + (z_2\mu_2 \frac{\partial V}{\partial x} + \frac{\mu_2 k}{c_2}\frac{\partial c_2}{\partial x}) = 0$$

$$v_b + (z_1\mu_1 \frac{\partial V}{\partial x} + \mu_1 k \frac{\partial \ln c_1}{\partial x}) = 0$$

$$v_b + (z_2\mu_2 \frac{\partial V}{\partial x} + \mu_2 k \frac{\partial \ln c_2}{\partial x}) = 0$$

$$\frac{v_b}{z_1\mu_1} + \frac{\partial V}{\partial x} + \frac{\mu_1 k}{z_1\mu_1}\frac{\partial \ln c_1}{\partial x} = 0$$

$$\frac{v_b}{z_2\mu_2} + \frac{\partial V}{\partial x} + \frac{\mu_2 k}{z_2\mu_2}\frac{\partial \ln c_2}{\partial x} = 0$$

Eliminating $\frac{\partial V}{\partial x}$,

$$\frac{v_b}{k}\left(\frac{1}{z_1\mu_1} - \frac{1}{z_2\mu_2}\right) + \frac{1}{z_1}\frac{\partial \ln c_1}{\partial x} - \frac{1}{z_2}\frac{\partial \ln c_2}{\partial x} = 0 .$$

Case: $z_1 = 1$ and $z_2 = 1$

$$\frac{v_b}{k}(1/\mu_1 - 1/\mu_2) + \frac{\partial \ln c_1}{\partial x} - \frac{\partial \ln c_2}{\partial x} = 0$$

$$\frac{v_b}{k}(1/\mu_1 - 1/\mu_2) + \frac{\partial}{\partial x}\ln(c_1/c_2) = 0$$

$$\frac{Fv_b}{RT}\left(\frac{\mu_2 - \mu_1}{\mu_2\mu_1}\right) + \frac{\partial}{\partial x}\ln(c_1/c_2) = 0$$

Also,

$$v_b\left(\frac{1}{k\mu_1} - \frac{1}{k\mu_2}\right) + \frac{\partial}{\partial x}\ln(c_1/c_2) = 0$$

$$v_b\left(\frac{1}{D_1} - \frac{1}{D_2}\right) + \frac{\partial}{\partial x}\ln(c_1/c_2) = 0$$

$$v_b\left(\frac{D_2 - D_1}{D_1 D_2}\right) + \frac{\partial}{\partial x}\ln(c_1/c_2) = 0$$

The width of boundary is defined as the distance between points where the ratio (c_1 / c_2) varies from (e^2) to $(1/e^2)$ in $\frac{4RT}{Fv_b}\frac{\mu_2\mu_1}{\mu_2-\mu_1}$ or $\frac{4}{v_b}\frac{D_2D_1}{D_2-D_1}$. This shows that the width of the boundary is due to the balance between the applied electric field (or boundary speed) and diffusion.

Appendix 10. Mobility and Time Constant for Transient Response

We do not consider the time of acceleration of the charged species. Under the action of an electric field, a charged particle experiences a force along the electric field, $\vec{F}_E = q\vec{E}$. For a globular particle that moves in a viscous medium, the drag force is $\vec{F}_D = -6\pi\eta a\vec{v}$. The net force on the particle is $\vec{F}_{net} = \vec{F}_E + \vec{F}_D$ or $\vec{F}_{net} = q\vec{E} - 6\pi\eta a\vec{v}$. Consider a one dimensional case (with no loss of generality) $m\ddot{x} = q\vec{E} - 6\pi\eta a\dot{x}$, $m\ddot{x} + 6\pi\eta a\dot{x} = q\vec{E}$, or $\ddot{x} + \frac{6\pi\eta a}{m}\dot{x} = \frac{q}{m}\vec{E}$. These equations show first order dynamical behavior. As a result, it has a time constant of $\tau = \frac{m}{6\pi\eta a}$.

Characteristic values include:

Atomic mass unit = $\frac{1}{6.02\times10^{26}}$ kg

Atomic number of hydrogen = 1.008, chlorine = 35.453

Atomic radius of chlorine = 90.10^{-12} m

Viscosity of water = $\mu=10^{-3}$ kg/m.s.

From $\tau = \frac{m}{6\pi\eta a}$, $\tau = \frac{35.45}{6\pi 10^{-3} 90.10^{-12}} \frac{1}{6.02\times10^{26}}$ = $\tau = 0.0347\times10^{-12}$ = 35 femto seconds.

The acceleration time is very short. The time scale of interest in this study is a fraction of a second (about 1/10 to 1/100 of a second). So we can neglect the period of acceleration and consider the acceleration to be nearly instantaneous. If steady state is achieved quickly, we neglect the acceleration term. We are left with $\dot{x} = \frac{q}{6\pi\eta a}\vec{E}$ or $\dot{x} = \mu\vec{E}$. So we can justifiably express the constitutive relationship $\vec{v} = \mu\vec{E}$ where the mobility is $\mu = \frac{q}{6\pi\eta a}$. The mobility is proportional to the ratio of charge to size for a given molecule in a medium of a given viscosity.

This relationship is true for a spherical particle. This approximation may also be true for particles with shapes that are similar though not exactly identical.

Appendix 11. Additional Numerical Results

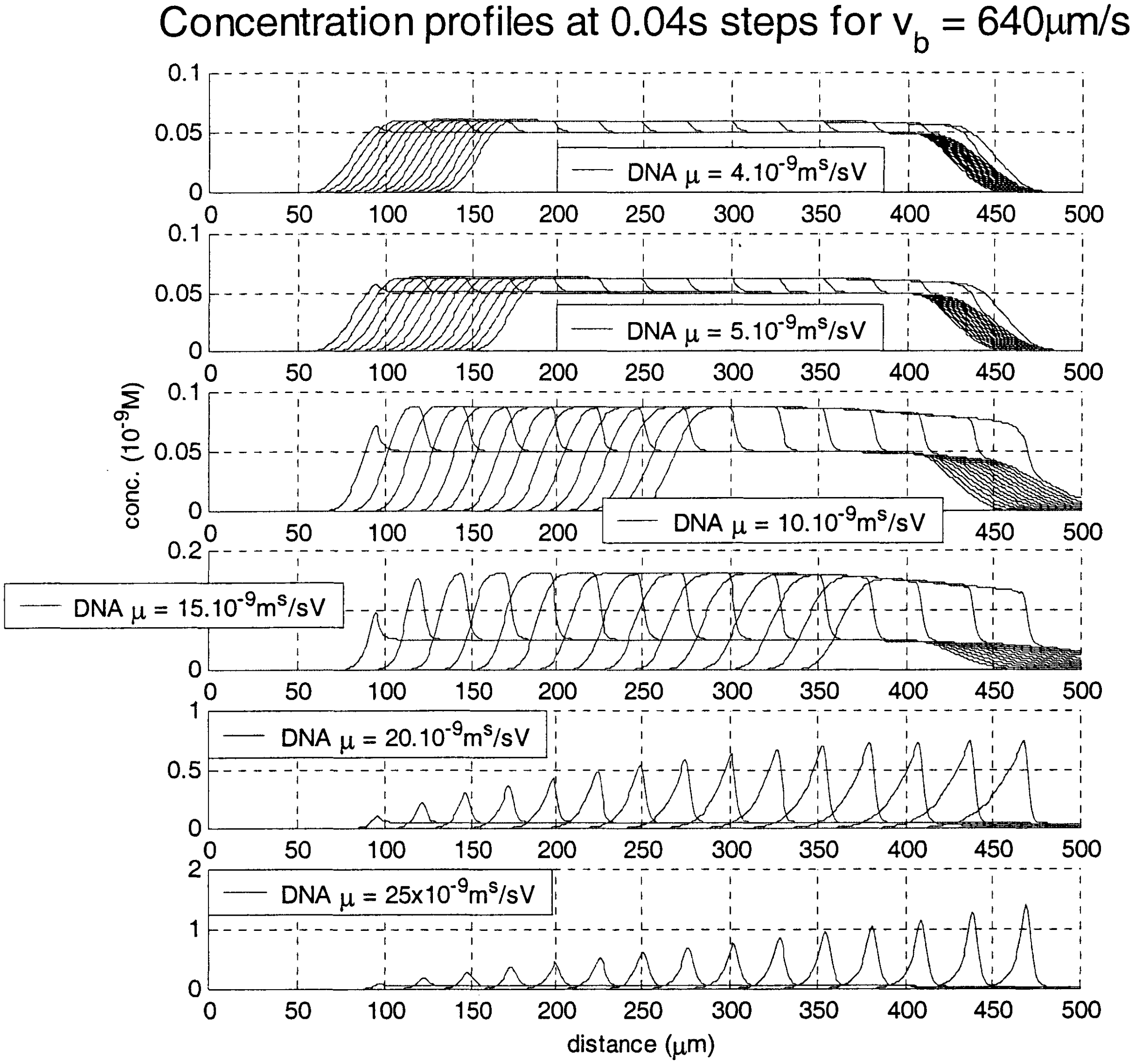

Figure 49. Stacking of Different Components for Moving for Boundary Speed of 640 μm/s

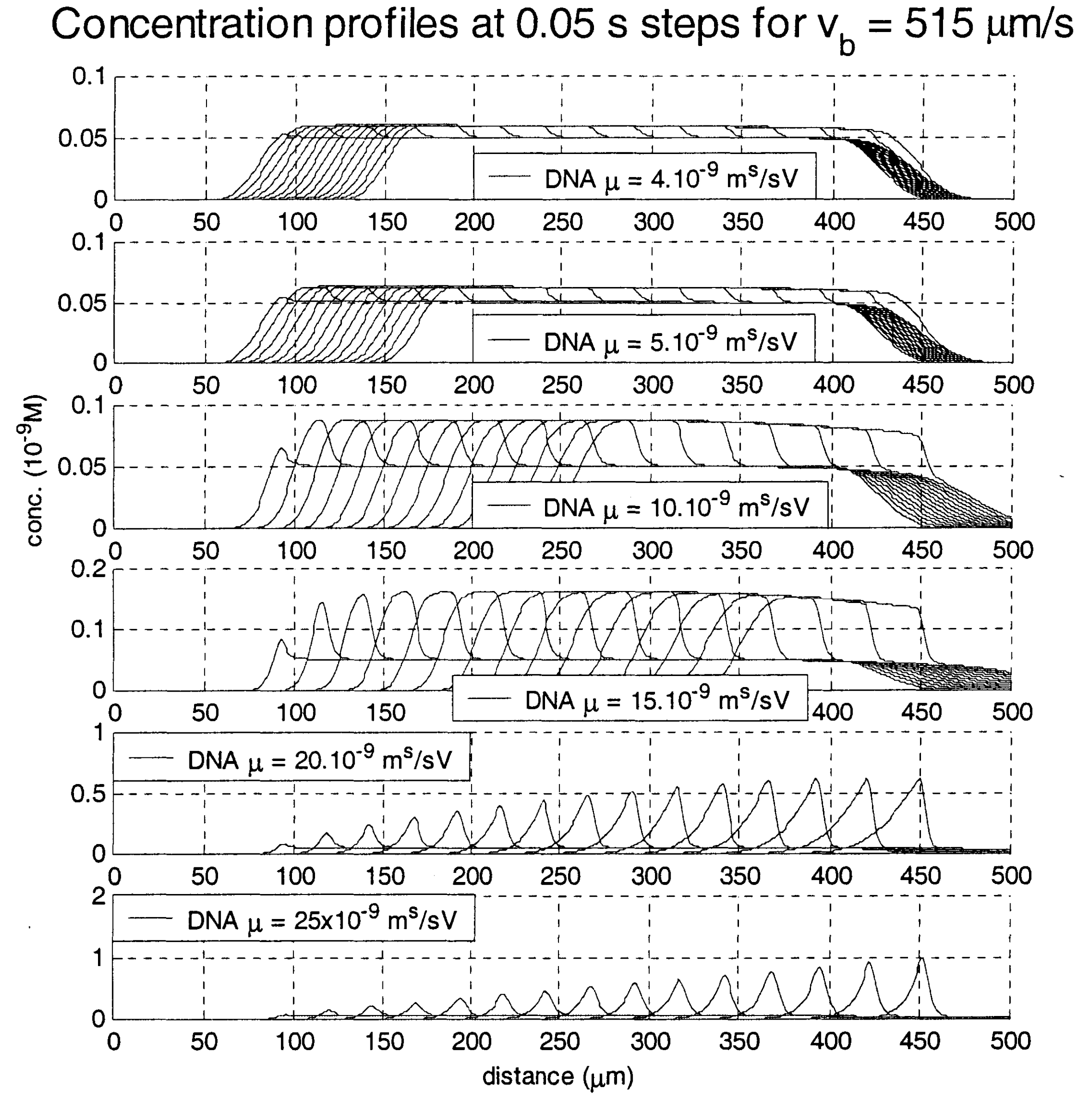

Figure 50. Stacking of Different Components for Moving Boundary Speed of 515 μm/s

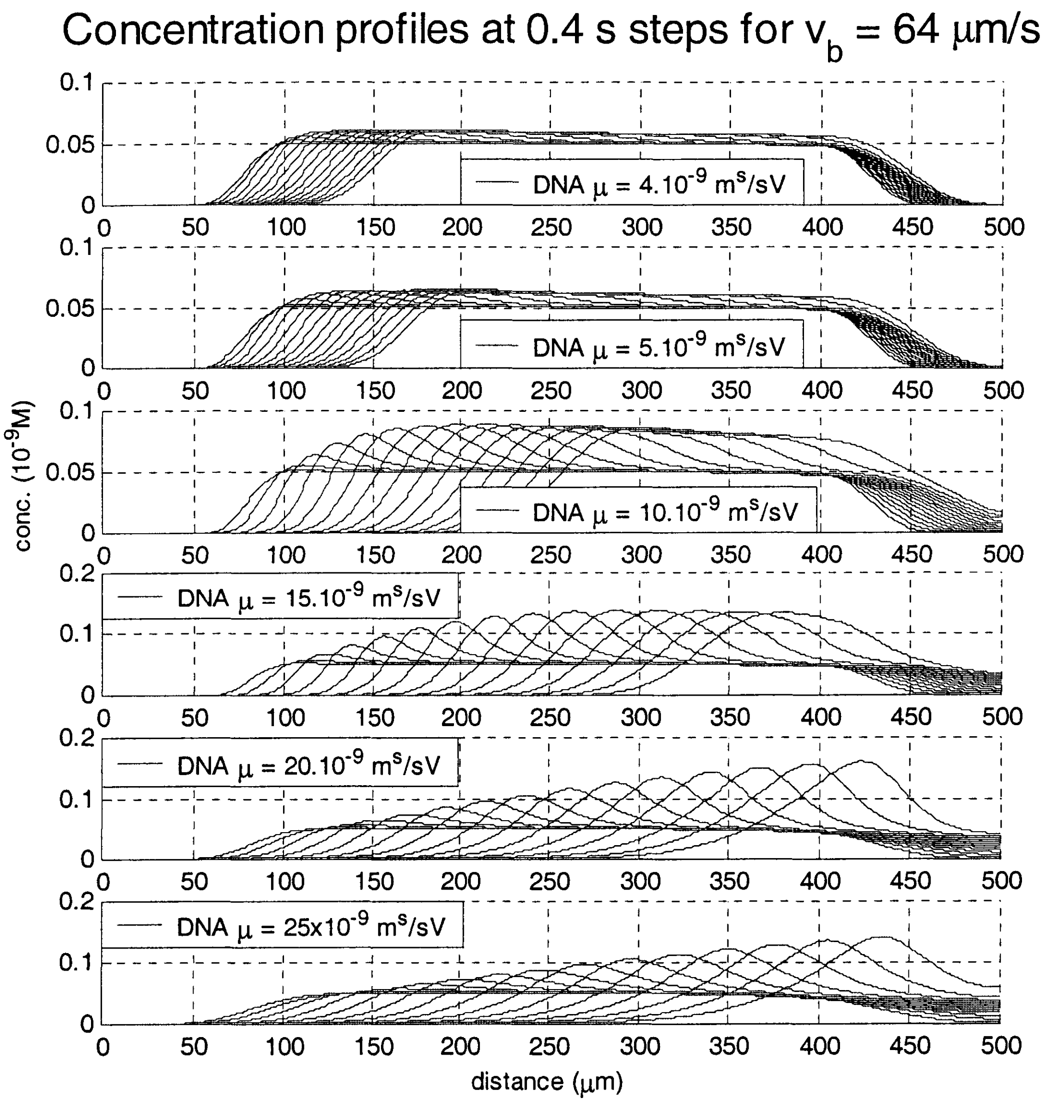

Figure 51. Stacking of Different Components for Moving Boundary Speed of 64 μm/s